Final Technical Report

Project Title: Advanced Machines for Marine Hydrokinetic Energy

Award Number: DE-EE0003641

Federal Agency to which Report is submitted: DOE EERE – Wind & Water Power Program

Date of Report: July 30, 2014

Project Period: January 14, 2014 – June 30, 2014

Principle Investigator: Ted Lesster, tlesster@rct-systems.com, (410) 694-0447

Report Submitted by: Edward Wagner, ewagner@rct-systems.com, (410) 694-8046

Recipient: RCT Systems, Inc., DUNS 795953095
1745A West Nursery Road
Linthicum, MD 21090-2906
Office: (410) 694-8050
Fax: (410) 859-1702

DOE Project Team: DOE HQ Program Manager – Jose Zayas
DOE Field Contract Officer – Pamela Brodie
DOE Field Grants Management Specialist – Jane Sanders
DOE Field Project Officer – Gary Nowakowski
DOE/CNJV Project Monitor – Erik Mauer
DOE Contracting Officer – Laura Merrick
DOE Technology Manager – Ryan Sun Chee Fore
DOE Technology Manager – Alison LaBonte
DOE NEPA Specialist – Laura Margason

Signature of Submitting Official:

Edward T. Wagner, VP Engineering, Program Manager
RCT Systems, Inc.

Acknowledgment

This material is based upon work supported by the Department of Energy, Office of Energy Efficiency & Renewable Energy, under Award Number DE-EE0003641.

Table of Contents

List of Acronyms

Acronym or Symbol	**Definition**
1010 Steel	A plain carbon steel with a nominal 0.10% carbon content
2-D	Two Dimensional
2S 4Q	Two Sides, Four Quadrants
3D	Three Dimensional
3-D	Three Dimensional
α, Alpha	Mean Tooth Width to Height Ratio
β, Beta	Tooth Width to Valley Width Ratio
γ, gamma	Angular displacement
Δ, Delta	Change
Δg	Change in Gap
θ, Theta	The measure of an angular position, measured in radians.
θa	Angular Deflection in degrees or radians
θb	Angular Deflection in degrees or radians
θ_n	Angle, n^{th} element
λ, lambda	Flux Linkage
ν, nu	Poisson's Ratio
φ, phi	Magnetic Flux, measured in Webers.
a	Outer Radius
A28lenrad	28 Pole Angular Tooth Length and Radius Variations
A28meancirc	Circumference of Axial Flux Machine with 28 Poles
A28meandia	Mean Diameter of Axial Flux Machine with 28 Poles
A28meanrad	Mean Radius of Axial Flux Machine with 28 Poles
ABC	Air Box Clearance
Abi	Area of Back Iron
AFRM	Axial Flux Reluctance Machine, synonymous with AGSRM or AFSRM
AFSRM	Axial Flux Switched Reluctance Machine, synonymous with AFRM or AGSRM
AGSRM	Axial Gap Switched Reluctance Machine, synonymous with AFRM or AFSRM
ANSYS	ANSYS Incorporated, Manufacturer of ANSYS Mechanical Analysis Software. Also refers to the software package itself.

Arat	Area Ratio
Astep	Step Angle
AT	Ampere Turns
At	Area of Tooth
Atv	Area of Tooth and Valley
Av	Area of Valley
b	Inner Radius
B field	Magnetic Flux Density, measured in Tesla.
C1	Plate Function C1
C2	Plate Function C2
C3	Plate Function C3
C4	Plate Function C4
C7	Plate Function C7
C8	Plate Function C8
C9	Plate Function C9
CM	Core Material
D	Plate Constant
deg	degrees, a measure of angles
di/dt	The derivative with respect to time of current, measured in Amperes per second.
dL(θ,i)/dt	The derivative with respect to time of Inductance, measured in Henries per second.
DOE	Department of Energy
dθ/dt	The derivative with respect to time of Angular Position, measured in radians per second.
dλ/dt	The derivative with respect to time of flux linkage
dφ/dθ	The derivative with respect to Theta of Magnetic Flux, measured in Webers per Radian
E	When used in a number, indicates an exponent base 10. That is, 10.1E5 equals 10.1×10^5
E	Young's Modulus
EDM	Electro-Discharge Machine
FEA	Finite Element Analysis
F_n	Force,n^{th} element
g	gap
gap	Axial tooth air gap

g_n	Gap,nth element
H field	Magnetic Field Strength, measured in Amperes per meter.
Hc	Coil Height
HIP	Hot Isostatically Pressed
htm	Tooth Height at Mean Radius
ID	Inner Diameter
in	inch
in	inch
IR	Inner Radius
J	Induced Eddy Current
K_1	Stiffness of element #1 (spring constant)
K_2	Stiffness of element #2 (spring constant)
Ka	Axial Stiffness in pounds per inch per unit length, or Newtons per meter per unit length.
Ka'	Axial Stiffness in pounds per inch or Newtons per meter.
Kb	Axial Stiffness in pounds per unit length, or Newtons per meter per unit length.
Kb'	Axial Stiffness in pounds per inch, or Newtons per meter.
K_{eq}	Equivalent Series Stiffness (spring constant)
ksi	Thousands of pounds per square inch, a measure of pressure.
kVA	Kilo Volt Amperes, a measure of apparent power.
K_{Θ}	Rotational Stiffness
L	Left
L	Inductance, measured in units of Henries
L(θ,i)	Inductance, as a function of angular position and current, measured in Henries.
L3	Plate Function L3
L3	Plate Function L3
L6	Plate Function L6
L9	Plate Function L9
Lb	Pound Avoirdupois, a measure of weight.
Lt	Tooth Length
m	meter
M19 Steel	A non-oriented electrical silicon steel with low core loss properties.
Mat	Material

Matlab/Simulink	Circuit and system simulation software produced by Mathworks, Inc., Natick, MA.
mm	millimeter
N/m	Newtons per meter, a measure of stiffness.
NI	The product of the number of turns (N) and the current (I), measured in Ampere Turns
npoles	Number of poles
NT	Number of Teeth
OD	Outer Diameter
OR	Outer Radius
Pi	Power, as a function of current, measured in Watts.
psi	pounds per square inch
pSim	Circuit simulation software produced by Powersim Inc., Rockville, MD.
PTC	PTC Incorporated, Manufacturer of PTC Creo Computer Aided Design Software.
R	Right
R28circ	Circumference of Radial Flux Machine with 28 Poles
R28dia	Diameter of Radial Flux Machine with 28 Poles
R28lenax	Axial Length of Radial Flux Machine with 28 Poles
R28pole	Circumferential Pole Length in the Radial Flux Machine with 28 Poles
R28slot	Circumferential Slot Length in the Radial Flux Machine with 28 Poles
R28tooth	Circumferential Tooth Length in the Radial Flux Machine with 28 Poles
rad	radians, a measure of angles
rbi	radius, back iron
RCT	RCT Systems, Incorporated
RDR	Requirements Design Review
rev	revolutions
RFSRM	Radial Flux Switched Reluctance Machine, synonymous with RGSRM
RGSRM	Radial Gap Switched Reluctance Machine, synonymous with RFSRM
Ri	Inner Radius
Rm	Tooth mean radius
R_m	Radius, mean
r_n	Radius, n^{th} element
Ro	Outer Radius
ro	Load Radius

Rs	Series Resistance, measured in units of ohms
rs	radius stator
s	second, unit of time
sbi	stator back iron
sec	second, unit of time
SR	Switched Reluctance
SRM	Switched Reluctance Machine
ss	stator slot
T	Torque
t	Thickness
T_n	Torque, n^{th} element
US	United States
v	Voltage, measured in Volts.
V	Volts
vi	The product of Voltage and Current.
VR	Variable Reluctance
W	Load or weight, in pounds or Newtons
w	Unit Line Load, in pounds per inch or Newtons per meter
Wb	Webers, units of flux linkage.
Wc	Coil Width
Wcc	Coil Clearance Width
Wt	Tooth Width
wtm	Mean Tooth Width
ya	Axial Deflection in inches or meters
yb	Axial Deflection in inches or meters

List of Figures

List of Tables

Executive Summary

This program studied novel concepts for an Axial Flux Reluctance Machine to capture energy from marine hydrokinetic sources and compared their attributes to a Radial Flux Reluctance Machine which was designed under a prior Department of Energy program for the same application. Figure 1 illustrates key mechanical features. Detailed electromagnetic and mechanical analyses were performed to determine the validity of the concept and to provide a direct comparison with the existing conventional Radial Flux Switched Reluctance Machine designed during the Advanced Wave Energy Conversion Project, DE-EE0003641.

The alternate design changed the machine topology so that the flux that is switched flows axially rather than radially and the poles themselves are long radially, as opposed to the radial flux machine that has pole pieces that are long axially. It appeared possible to build an axial flux machine that should be considerably more compact than the radial machine. In an "apples to apples" comparison, the same rules with regard to generating magnetic force and the fundamental limitations of flux density hold, so that at the heart of the machine the same torque equations hold. The differences are in the mechanical configuration that limits or enhances the change of permeance with rotor position, in the amount of permeable iron required to channel the flux via the pole pieces to the air-gaps, and in the sizing and complexity of the electrical winding. Accordingly it was anticipated that the magnetic component weight would be similar but that better use of space would result in a shorter machine with accompanying reduction in housing and support structure. For the comparison the pole count was kept the same at 28 though it was also expected that the radial tapering of the slots between pole pieces would permit a higher pole count machine, enabling the generation of greater power at a given speed in some future design.

The baseline Radial Flux Machine design was established during the previous DOE program. Its characteristics were tabulated for use in comparing to the Axial Flux Machine. Three basic conceptual designs for the Axial Flux Machine were considered: (1) a machine with a single coil at the inner diameter of the machine, (2) a machine with a single coil at the outside diameter of the machine, and (3) a machine with a coil around each tooth. Slight variations of these basic configurations were considered during the study. Analysis was performed on these configurations to determine the best candidate design to advance to preliminary design, based on size, weight, performance, cost and manufacturability.

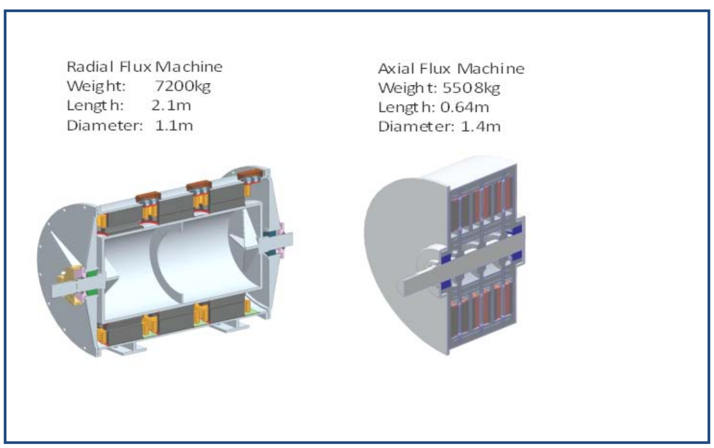

Figure 1 – Radial and Axial Flux Machine Features

The configuration selected as the most promising was the multi-pole machine with a coil around each tooth. This configuration provided the least complexity with respect to the mechanical configuration and manufacturing, which would yield the highest reliability and lowest cost machine of the three options. A preliminary design was performed on this selected configuration. For this first ever axial design of the multi rotor configuration the 'apples to apples' comparison was based on using the same length of rotor pole as the axial length of rotor pole in the radial machine and making the mean radius of the rotor in the axial machine the same as the air gap radius in the radial machine. The tooth to slot ratio at the mean radius of the axial machine was the same as the tooth to slot ratio of the radial machine.

The comparison between the original radial flux machine and the new axial flux machine indicates that for the same torque, the axial flux machine diameter will be 27% greater, but it will have 30% of the length, and 76% of the weight. Based on these results, it is concluded that an axial flux reluctance machine presents a viable option for large generators to be used for the capture of wave energy. In the analysis of Task 4, below, it is pointed out that our selection of dimensional similarity for the 'apples to apples' comparison did not produce an optimum axial flux design. There is torque capability to spare, implying we could reduce the magnetic structure, but the winding area, constrained by the pole separation at the inner pole radius has a higher resistance than desirable, implying we need more room for copper. The recommendation is to proceed via one cycle of optimization and review to correct this unbalance and then proceed to a detailed design phase to produce manufacturing drawings, followed by the construction of a prototype to test the performance of the machine against predicted results.

Introduction

Prior to the time of initiation of the original Power Take Off design project the price of Permanent Magnet material, in particular the Neodymium Boron Iron based material, had skyrocketed and prime contractor personnel had decided that based on their earlier work they would seek a switched reluctance machine approach.

RCT was able to offer a novel approach based on minimizing the effects of negative magnetic stiffness by putting all the poles of one phase in a complete cylinder and making a multiphase machine by stacking phases on the single shaft with each phase rotated with respect to the next (120deg electrical rotation for a three phase machine).

This approach minimized also the length of end turn and pole to pole wiring for each phase so reducing losses. Use of an inverter to provide the required excitation current for each pulse cycle of generation of the machine offered better efficiency compared with the more traditional three phase single stator AC excited machines. In the wave environment furthermore it would be possible to modify the excitation to follow the frequency of the wave energy and generate into a fixed voltage much more easily than from a permanent magnet machine. It was also easy to preserve efficiency by switching off in the valleys of the wave where the energy required to excite the reluctance machine in order to harvest the energy would be greater than that present in the wave at that time.

The original Power Take Off reluctance machine design was directed initially by the prime contractor technical team to look at a truly linear manifestation in which a "rotor" became a translator rising and falling with the waves inside a linear "stator". The machine by definition had to be of height ((Length of Stator) + 2 x (Length of stroke of wave)). In this case a 5m stroke was required and the total machine would have been 40+ feet high. A linear to rotary conversion based toothed belt approach permitted construction of an oscillating machine in which the translator was wrapped around inside the stator and thus was electrically and mechanically endless.

Thus has evolved the Radial Flux Switched Reluctance Machine for wave energy conversion. It is also perfectly suitable for continuous rotation generating and motoring in, for example a tide power application.

Subsequent to the prime contractor running out of funds and the termination of the PTO project before it was completed, initial calculations indicated that an axial flux machine could be more compact than the radial machine already designed. The rotor drum in the radial machine was a large hollow space, that could be filled with torque producing components in the axial machine and so bring the overall diameter down. This would reduce the machine size and reduce structural weight even if the basic electromagnetic structure was about the same weight.

The current extension of the technology within the same contract funding total explores the possible benefits of the axial flux approach versus the original radial flux machine. Any reduction in weight and size implies reduced capital cost and so is favorable in the renewable energy environment where, although the energy itself comes for free, the capital cost of collecting and distributing it as electricity is very high.

Background

The predominant use of multi phase reluctance machine technology is in small high speed machines. In these, AC excitation is used with a single rotor and a stator wound to carry all three phases interleaved around the circumference of the stator. In any reluctance machine the unwanted magnetic forces that attract the rotor radially to the stator far exceed the wanted forces that apply circumferentially to rotate the rotor. The unwanted forces in a three phase wound machine causes unbalanced radial forces on the rotor which cause vibration and noise. Likewise this configuration of machine, when used in a switched reluctance machine (SRM) mode accentuates the effect of switching and commutation ripple causing unwanted high frequency noise. It is this type of machine that has caused reluctance machines to be considered noisy.

Both the original radial machine design for the PTO project and this study of an axial flux version of the machine rely on three separate single phase machines stacked axially and rotated through 120 electrical degrees. This offers lower winding resistance per phase which benefits efficiency and balances out the unwanted radial magnetic force effects due to the switching or basic three phase excitation which is now a uniform 360 mechanical degree excitation of a single phase per machine segment. This study will make extensive use of FEA electromagnetic simulation and analysis. While the radial machine could be analyzed using 2 dimensional FEA the axial flux machine requires 3-dimensional analysis. RCT has developed an excellent 3-D modeling technique in Infolytica and now has an ability to analyze such machines and alternate configurations efficiently. The primary team working on this project has experience in both FEA power electronics and machine design of reluctance machines and permanent magnet machines.

Project Objective:

The primary objective of the proposed project is to perform design and analysis of novel concepts for an Axial Flux Reluctance Machine (AFRM) to capture energy from marine hydrokinetic sources. The project will perform detailed electromagnetic and mechanical analysis to determine the validity of the concept and to provide a direct comparison with the existing conventional rotary based Switched Reluctance Machine designed during the original Advanced Wave Energy Conversion Project, DE-EE0003641.

Project Goals:

The goal for an alternate design is to change the machine topology so that the flux that is switched flows axially rather than radially and the poles themselves are long radially versus the radial flux machine that has pole pieces that are long axially. Based on our understanding of the wanted and unwanted magnetic forces from the radial design it appears possible to build an axial flux machine that should be considerably more compact than the radial machine. In “apples to apples” comparison the same rules with regard to generating magnetic force and the fundamental limitations of flux density hold so that at the heart of the machine the same torque equations hold. The differences will be in the mechanical configuration that limits or enhances the change of permeance with rotor position, in the amount of permeable iron required to channel the flux via the pole pieces to the air-gaps, and in the sizing and complexity of the electrical winding. Accordingly it is likely the magnetic component weight will be similar but that better use of space will result in a shorter machine with accompanying reduction in housing and support structure. It is also expected that the radial tapering of the slots between pole pieces will permit a higher pole count machine.

Results and Discussion

This section includes the work done according to the tasks for the project. The information is task specific and refers to tasks as listed in the Statement of Project Objectives.

Task 1: Machine design and concept trade-offs

Specific objectives (Task 1)

The existing switched reluctance machine design was reviewed and critical design review information and a manufacturing package was delivered.

Target requirements and machine parameters to be used for the Axial Flux Reluctance Machine design were finalized.

Conceptual designs were evaluated and compared to determine the optimum configuration of the Axial Flux Reluctance Machine for further development in the following tasks.

Parameters determined included the number and physical dimensions of poles, the length of air gaps, the radius and length of the machine, and the speed of the machine.

Size, weight, cost, efficiency and performance were considered.

Major activities (Task 1)

The existing switched reluctance machine design depicted in Figure 2 has been reviewed and critical design review information and a manufacturing package was delivered. Target requirements and machine parameters to be used for the Axial Flux Reluctance Machine design were finalized.

We started the axial design by selecting an axial machine configuration that, like the radial machine, had 28 poles. The length of each pole piece is the same as the length of each pole piece in the radial machine. Also, the mean radius of the axial machine pole pieces was set to be the same as the radius at the air-gap in the radial machine. At the mean radius, the pole structure cross section dimensions looked the same as the radial machine pole structure dimensions.

Radial Machine Baseline [Original PTO Design]

RDR Radial flux machine basic dimensions as a starting point

$$\text{npoles} := 28$$

$$\text{R28dia} := 0.928\,\text{m} \qquad \text{R28circ} := \text{R28dia}\cdot\pi = 2.915\,\text{m} \qquad \text{R28pole} := \frac{\text{R28circ}}{\text{npoles}} = 10.412\cdot\text{cm}$$

$$\text{R28tooth} := \text{R28pole}\cdot\frac{4.5}{10} = 4.685\cdot\text{cm} \qquad \text{R28slot} := \text{R28pole}\cdot\frac{5.5}{10} = 5.727\cdot\text{cm}$$

$$\text{R28lenax} := 0.291\ \text{m}$$

Machine size 1.33m diameter x 1.5m long

Volume 3.10m^3

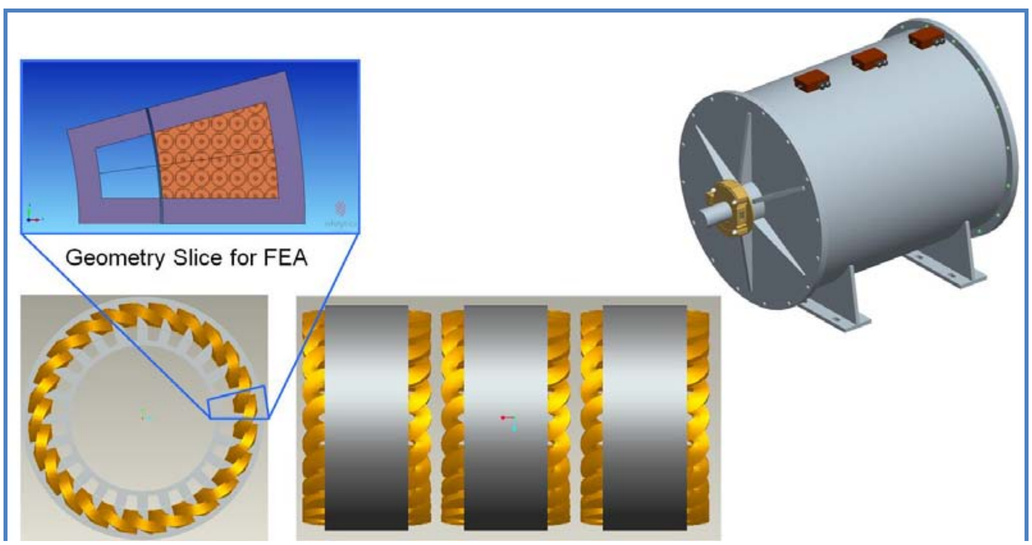

Figure 2 - RDR Rotor and Stator Cores (Left) and 3-Phase SRM (Upper Right)

Initial Axial Pole Structure Scaled from Radial Machine Baseline

Axial Machine magnetic dimensions - 28 pole version outside coil

$A28meandia := R28dia = 0.928m$

$A28meanrad := A28meandia \cdot 0.5 = 0.464m$

$A28meancirc := A28meandia \cdot \pi = 2.915m$

$A28lenrad := R28lenax = 0.291m$

Three conceptual axial flux machine configurations were considered and all were evaluated magnetically and to a first order for impact on electrical parameters. Each of the three configurations have certain common options related to the shaping of the magnetic pole structures themselves rather than the overall dimensioning of the machine.

Low winding resistance is a major factor in improving reluctance machine efficiency and a key feature available to the axial flux machine was a potential winding simplification. Accordingly, initial analysis focused on configurations favorable from this electrical perspective.

Step 1) Instead of multiple pole windings as in the radial machine, a single circumferential coil could excite all poles of one phase by driving the flux via back-iron along the pole structures. This was the first configuration selected to start our comparative analysis.

Step 2) If the single coil approach near the circumference of the machine (Outside Radius (OR) coil) could be replaced by a single coil at the shaft side of the stator (Inside Radius (IR) coil) then the per turn length of the coil would be much less for a lower resistance and better machine efficiency. Mechanically more complex, this second configuration was selected for comparison.

Step 3) Evaluate a pole structure with tapered (following radii) stator and rotor teeth, and straight (with changing slot to pole width as pole radius increased, i.e. tapered slots)

Single Phase Structure as Basis for FEA

The RCT configuration for multi-phase switched reluctance machines (SRM) is to stack single phases on a common rotor. The driver for this is the benefit from pulsing the flux in a single phase air-gap symmetrically all around so that uniform mechanical stress that is produced by the pulse and negative stiffness effects are minimized.

Figure 3 illustrates two single coil per phase, axial gap, Switched Reluctance (SR) electrical machines modeled and analyzed using FEA methods. The y-axis is defined as the axis of revolution for reference. In Figure 3, upper left, an array of ferromagnetic “blocks” around the outer mid line of the machine are mechanically tied together to form the rotating element of the machine. For magnetic analysis, the non-ferromagnetic, non-electrically conductive rotor structure need not be included.

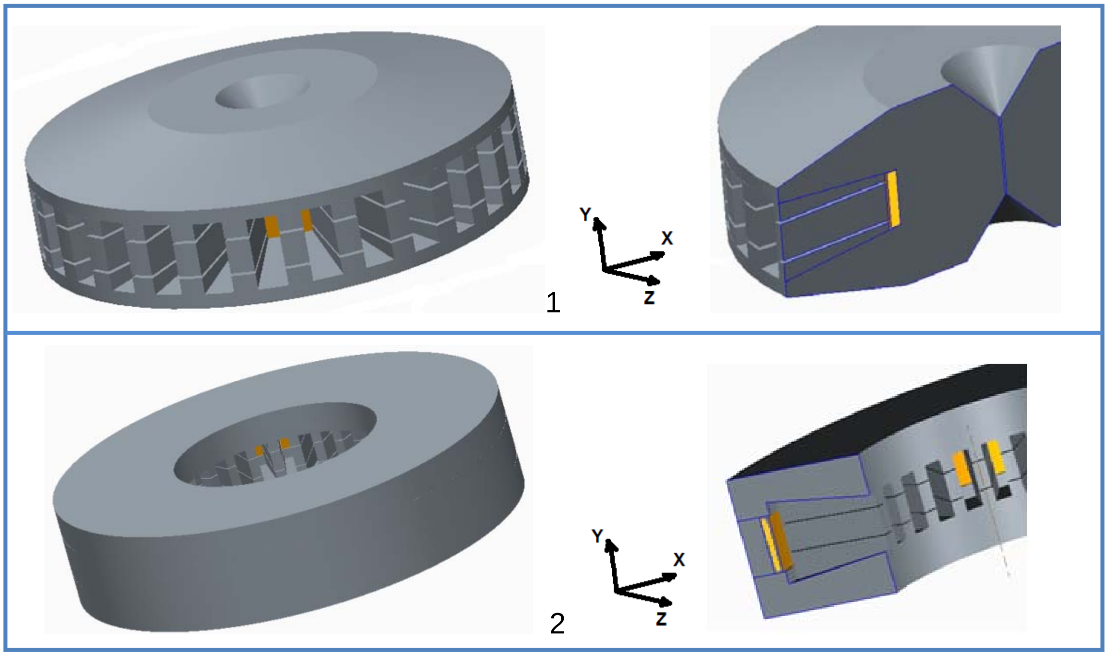

Figure 3 - SR Machine Coil at IR (Top) and Coil at OR (Bottom)

Axial Machine Configurations - Inner Diameter Coil and Outer Diameter Coil
There is a single cylindrical coil inside the tooth structure and wound around central ferromagnetic return path at the Inside Radius (IR) in the IR Coil configuration; see Figure 3 upper right. An alternate configuration, Figure 3 lower right, has the rotor at the inside and the coil and return path at the Outside Radius (OR).

Figure 4 illustrates how only half of the geometry need be considered by imposing a flux normal requirement on the x-z plane at the midline cut. Though the IR Coil configuration is shown, the symmetrical analysis method also applies to the OR Coil.

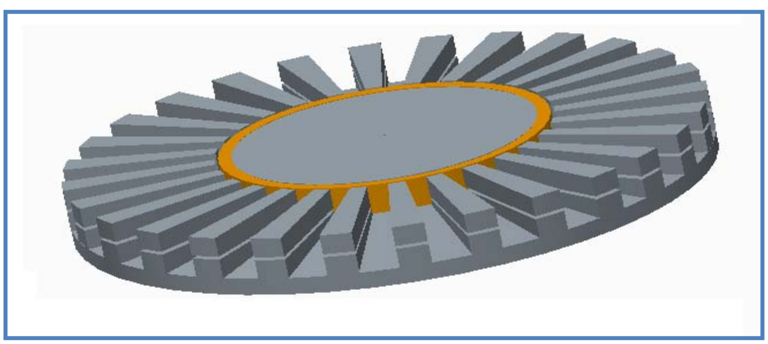

Figure 4 - Half Geometry of Coil at IR

Furthermore, even periodic boundary conditions enable a single tooth to be modeled accurately. The tooth geometry selected has a half a valley on either side as illustrated in Figure 5.

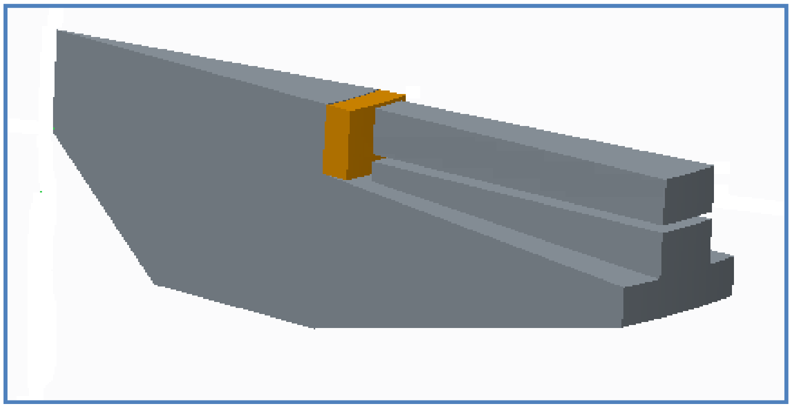

Figure 5 - Single Tooth, Half Geometry of Coil at IR

There is weight reduction chamfering options included in the parametric model, but these are set to zero for initial studies, resulting in the rectangular shapes with parallel sides. Therefore, the flux density is not constant at various radii from the axis of revolution in the iron.

The coil geometry was arbitrarily constructed from two bodies, enabling the current input and output terminals to be on coil faces that are not coincident with surfaces that have boundary conditions. The coil was defined using the multi terminal feature and the stranded coil option. Furthermore, the gap region was subdivided into four regions to facilitate re-meshing when the rotor position is moved. This requires re-meshing of only two sub volumes for each move, instead of the entire problem. Rotor and stator air boxes enclose all the parts for modeling purposes.

Significant results (Task 1)

While the ultimate objective of this task is to evaluate competing designs of axial flux machines against the system target requirements and then evaluate the winner against the existing radial machine design, a specific intermediate objective addressed in this first quarter time frame in this task is to develop a cost effective (in engineering time and computer resources) method for analyzing each concept configuration magnetically and develop a magnetic, mechanical and electrical data to serve as input to manufacturing and cost estimates.

The driver for this modeling activity is that the axial gap machine has an annular disk gap, requiring electromagnetic analysis in three dimensions (3-D). Radial machines, with cylindrical gaps and can be analyzed electromagnetically in two dimensions (2-D).

Historically, lumped parameter permeance path analysis and 2-D Finite Element Analysis (FEA) approximations have been used to analyze the types of problems encountered here, due to size, complexity and significant computer resources needed for 3-D models. The axial gap Switched Reluctance (SR) machine requires 3-D analysis due to the flux paths. Also, given the flux variations in the tooth structure, nonlinear BH characteristics must be considered for an accurate result in any SRM analysis.

A significant accomplishment is that we have developed a small but accurate 3-D FEA model that can be created using problem symmetry to reduce the size to **1/(2N)** of the original problem, where **N** equals the number of teeth. Use of boundary conditions in state of the art 3-D FEA tools, such as Infolytica MagNet Version 7.1.1, makes this problem now quite tractable. The geometries presented and analyzed in the body of this report were created in Infolytica MagNet FEA software.

Key outcomes (Task 1)

Ability for relatively rapid analysis of complex axial machine shapes.

<u>Task 2: Modeling and Analysis</u>

Specific objectives (Task 2)

The novel Axial Flux Reluctance Machine has been developed for the target application. Detailed electromagnetic finite element analyses (FEA) were performed using Infolytica. Characteristics studied included the evaluation of the negative stiffness effect caused by displacement of the rotor and stator elements from their ideal positions. These forces typically drive the mechanical design in a conventional reluctance machine, since the rotor and stator have to be designed for a mechanical stiffness sufficient to counteract the negative magnetic stiffness effect of the unwanted radial force which is many times higher than the desired (torque producing) circumferential force. This radial force increases as the air gap narrows from mechanical imperfections or from slight bending of the rotor shaft under the radial forces. The force always increases in the direction of the 'bend' and aggravates the 'bend' because the reduced air gap reduces the reluctance and so increases flux and the force, hence giving rise to the negative stiffness effect.

However, the proposed design uses a novel arrangement of rotor, stator and air gaps to dramatically reduce the unwanted forces on the rotor. The analysis determined the effectiveness of this new configuration, and the resultant mechanical forces that the structure must withstand. These forces drive the material selection, mass and volume of the machine. A model of the machine was created in PTC Creo Parametric (Pro/Engineer), and the physical structure analyzed using ANSYS.

The key is to definitively relate mechanical machine configuration to the wanted electromagnetic forces that serve as the discriminator for evaluating the effectiveness of a machine, and define unwanted forces that must be compensated for in mechanical stiffness calculations.

Major activities (Task 2)

Parameterization for Rapid Analysis in the Future
For subsequent rapid capability to model different structures it is very beneficial to parameterize the structures. A motion component that includes the rotor tooth, two air gaps closest to the rotor tooth and the rotor air box was used to enable transient analysis with minimal re-meshing for faster analysis times. Even periodic boundary conditions on the radial planes and a normal boundary condition on the mid plane were used. Non-linear ferromagnetic material properties were also used. Ferromagnetic material conductivity was set to zero; eliminating eddy currents. With proper lamination, eddy currents will be manageable. Traditional analyses are based on the weight of the iron, the electrical frequency and flux density (Steinmetz model) to account for core losses.

For initial model validation, a preliminary coarse mesh and static solution using linear materials were generated at the tooth aligned and unaligned positions to verify model mesh integrity. The results are shown in Figure 6 and Figure 7 for arbitrary geometry.

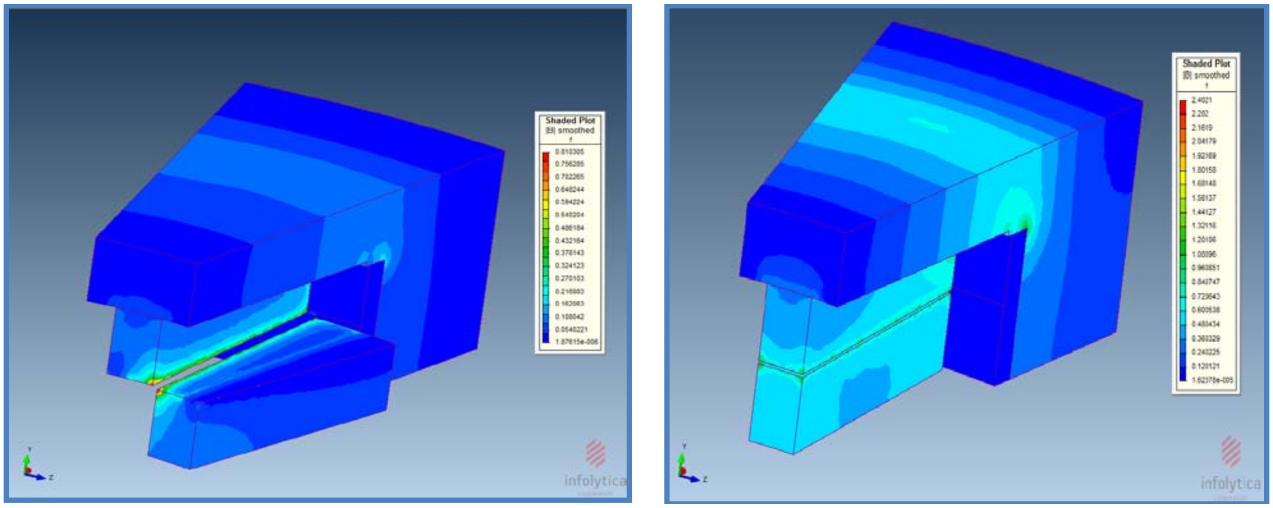

Figure 6 – Typical Static Solution, Linear Material, Unaligned (L) and Aligned (R)

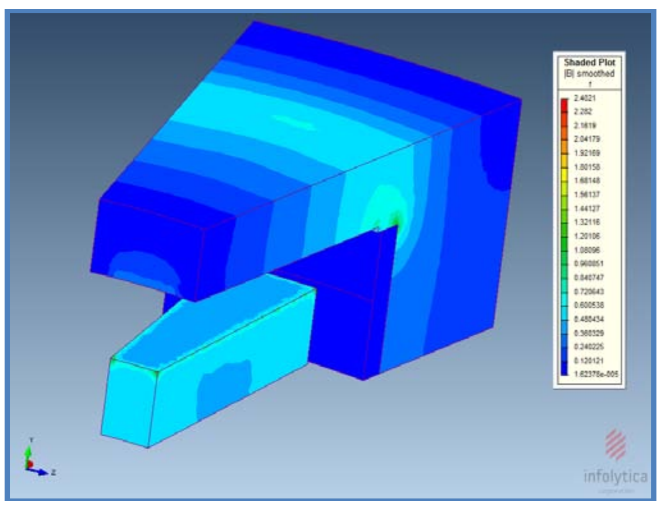

Figure 7 – Typical Static Solution, Linear Material, Aligned, Stator Tooth Hidden

Subsequently, a nonlinear material (1010 Steel) was implemented and resulted in improved solution accuracy with an insignificant increase in solution time. Material conductivity was again set to zero to eliminate core losses. Realistic geometry values were implemented per Table 1.

Table 1 - Parametric Studies Input Data

gap	0.0025
Rm	0.675
Lt	0.34
Alpha	1
Beta	0.45
Wcc	0.00636
Wc	0.0254*3
Hc	0.13/3
Arat	1.45
NT	56
Atv	(2*%pi)/%NT
At	%Beta*%Atv

Av	%Atv-%At
wtm	%Beta*(2*%PI*%Rm/%NT)
htm	%Alpha*%wtm
Abi	(%Beta*(2*%PI*%Rm*%Lt))/%Arat
ABC	0.02
Astep	0*0.5*%Atv
Ro	%Rm+0.5*%Lt
Ri	%Rm-0.5*%Lt
Mat	CR10: Cold rolled 1010 steel
Speed	2*2*%PI
Turns	6
NI	1333*6

Next the mesh was refined, globally by setting a maximum limit to the size and a local limit was applied to the two gap regions closest to the gap midline. Figure 8 illustrates the Flux Density results.

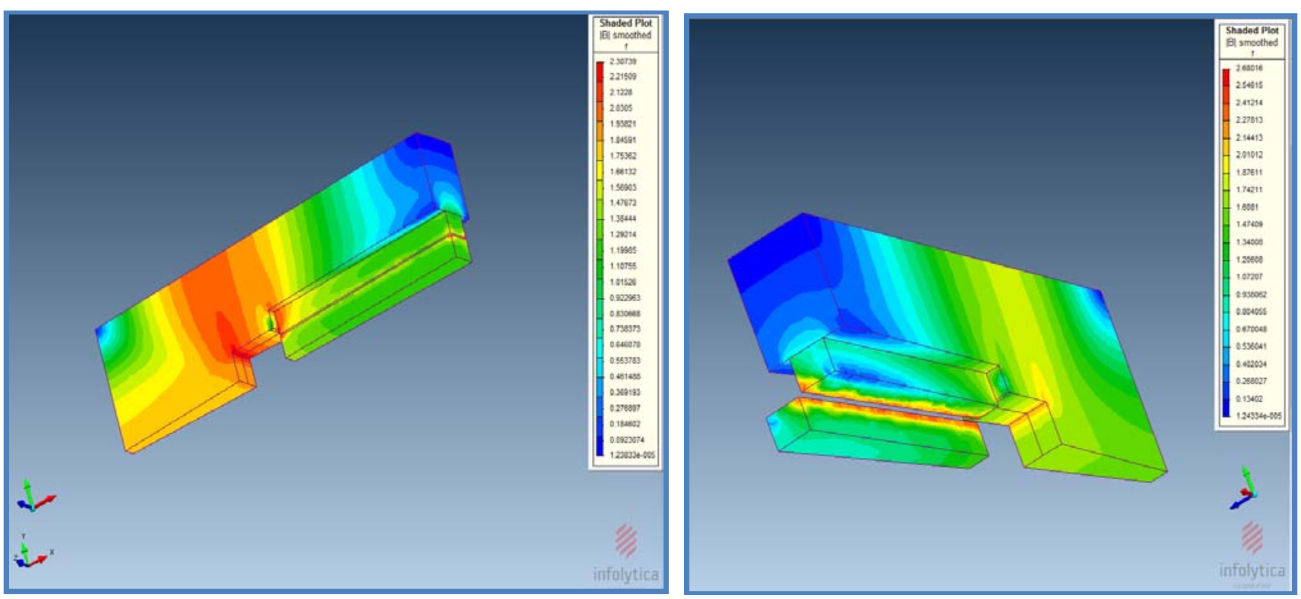

Figure 8 - Coil Inside, 56-Teeth, 6-Turns, 1333 Amps, Aligned (L), Unaligned (R)

Transient solver with motion was implemented next. The maximum gap mesh size value was varied to achieve acceptable solution accuracy without undue increase in problem size or solution time. Figure 9 shows the torque accuracy improvement versus rotor position.

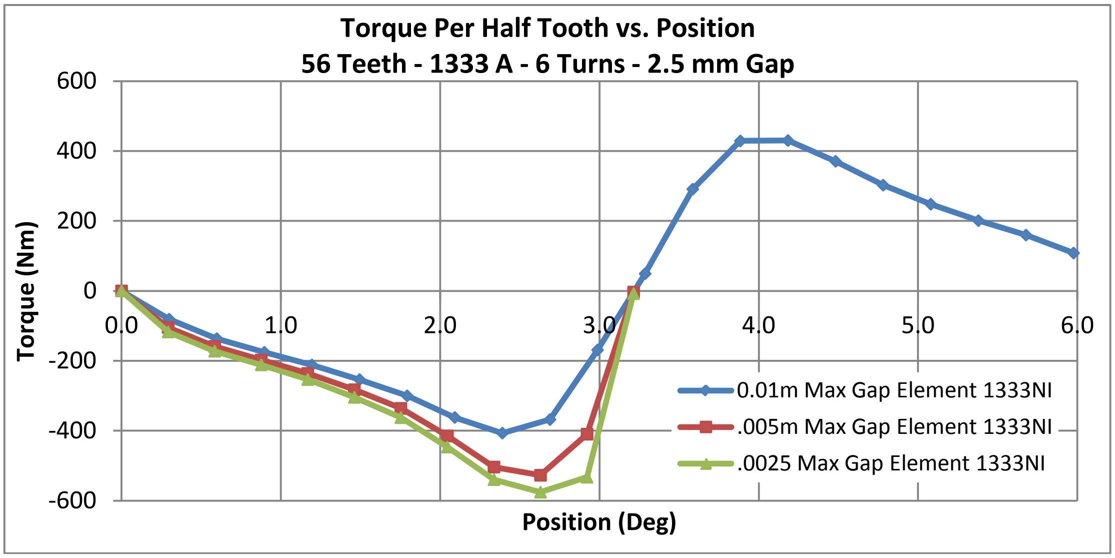

Figure 9 - Effect of Gap Element Size on Torque Results

With an acceptable torque accuracy obtained, a parameter sensitivity study was preformed. The nominal gap was varied first to obtain a method to evaluate axial stiffness. Three currents were evaluated at each gap. Force, torque and flux linkage were obtained and plotted for two pairs of gaps, 2.5 mm in Figure 10 and 5.0 mm in Figure 11.

Note that the results must be multiplied by 2 times the number of teeth (NT) to yield a total machine torque result; likewise for the flux linkage. The y axis force must be multiplied by the NT to yield a correct result and will cancel with the other half or mirror of the tooth geometry. Therefore, no axial force exists when the rotor is axially centered. However, these forces are present in the stator structure and must be considered in the structural and bearing designs.

In addition, the axial forces also produce a negative linear and angular stiffness present between the rotor and stators. The rotor and stator mechanical structure and bearings must have net positive stiffness 5 to 10 times larger than the negative stiffness to insure the structure is stable and the gap dimensions can be maintained. The negative stiffness also has an effect on modal analyses, as it lowers the resonance of the axial mode. The parameter variation results show the axial stiffness is negative and decreases as the nominal gap increases approximately as the ratio of the gap.

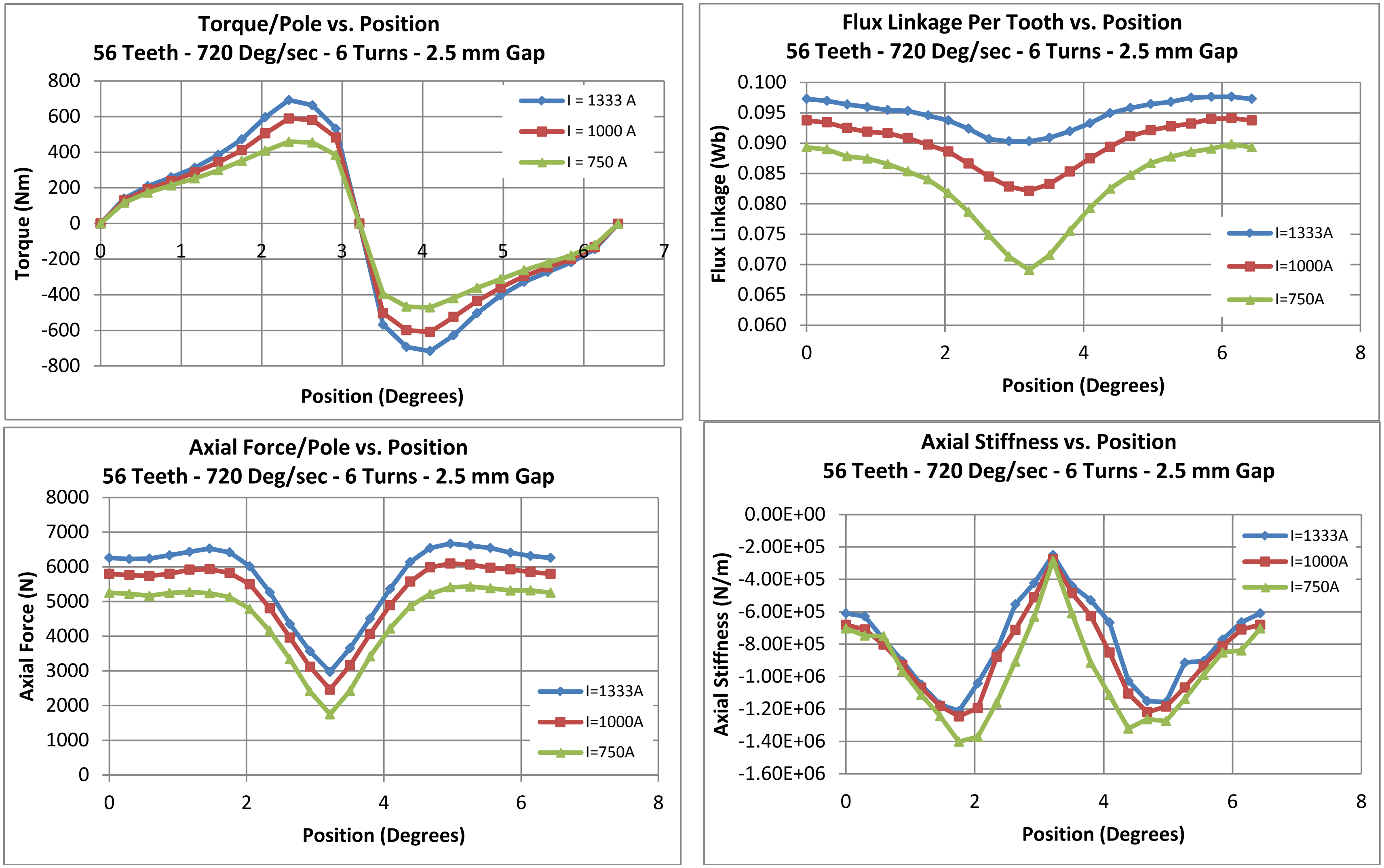

Figure 10 - Gap Results 2.5 mm: Torque, Flux Linkage, Stiffness, and Force

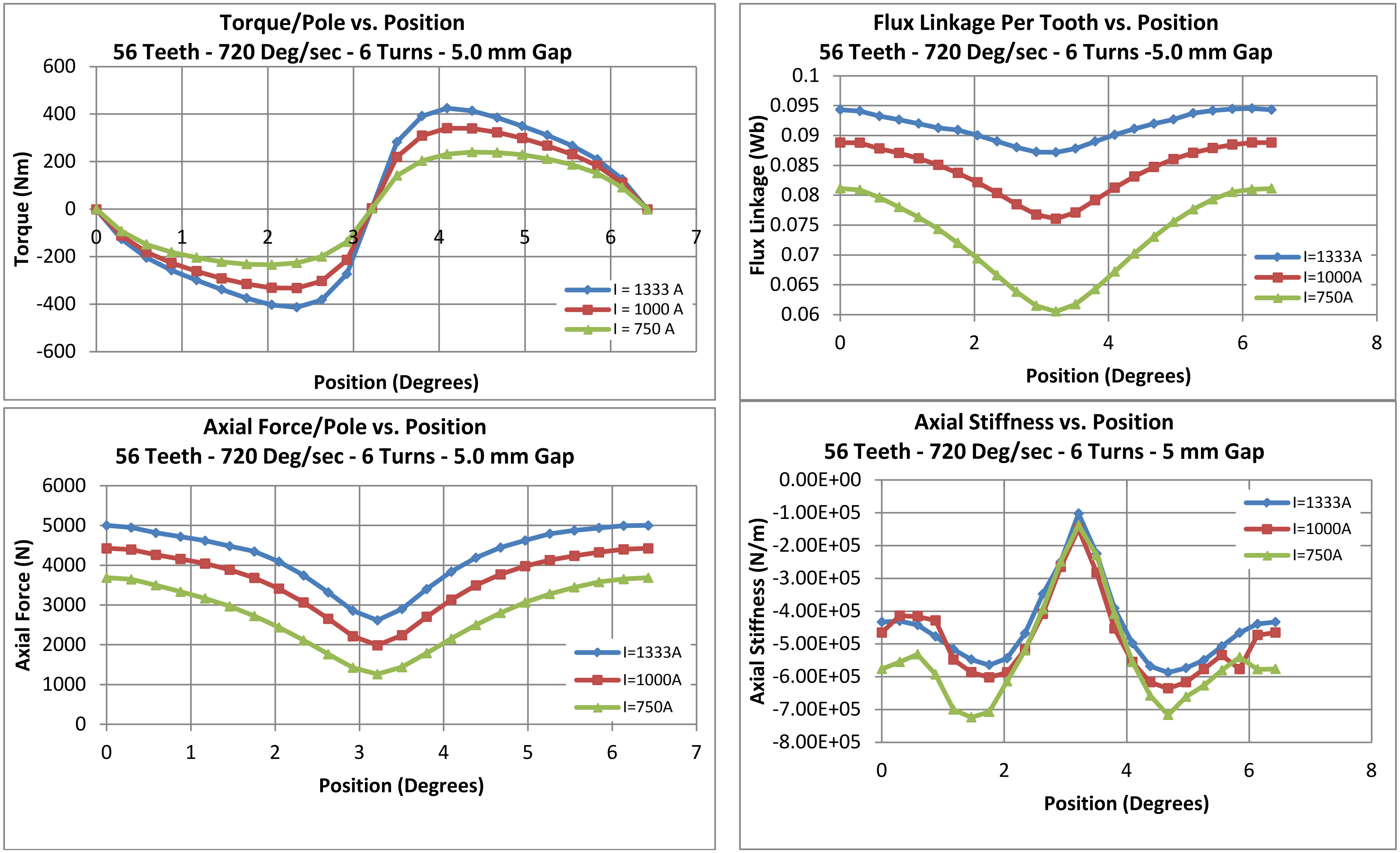

Figure 11 - Gap Results 5.0 mm: Torque, Flux Linkage, Stiffness, and Force

More parametric evaluations besides the gap and current parametric studies were conducted and included sensitivity to changes in the Mean Tooth Width to Height ratio (α - Alpha), Tooth Width to Valley Width ratio (β - Beta), Core Material (CM) and Number of Teeth (NT). There was no noticeable change in the torque vs. position shape with the Alpha variation as illustrated in Figure 12, but there is a minor increase in the torque amplitude.

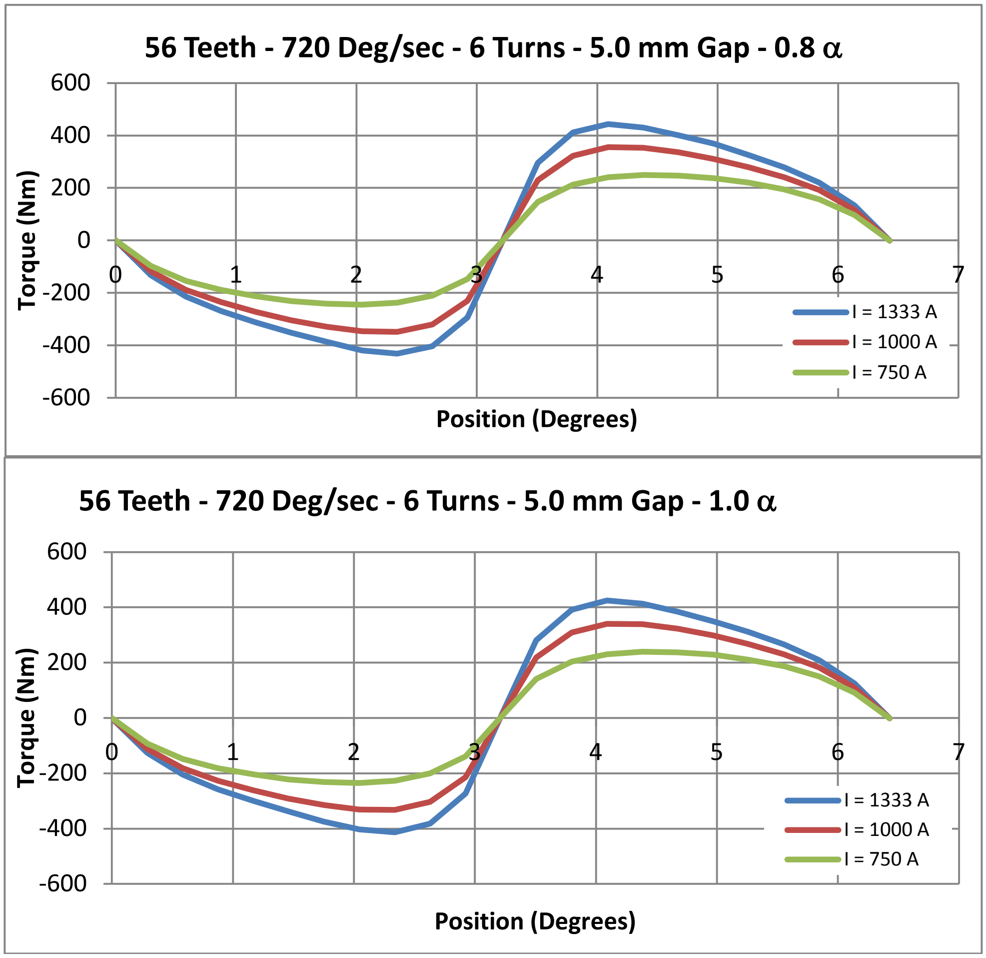

Figure 12 – Variations in Alpha and Current, Torque vs. Position

Figure 13 shows the performance sensitivity of the design to variations in Alpha graphically. There is some sensitivity in the torque; there appears to be a small peak at α = 0.8. There also appears to be a maxima between α = 0.8 and 0.9 in the variation of flux linkage between the aligned and unaligned positions. The peak axial force is essentially constant over the range investigated which means the axially stiffness is not dependent on Alpha. Analyses with higher density meshing can confirm these trends, but there is not enough design sensitivity to Alpha to warrant further investigation.

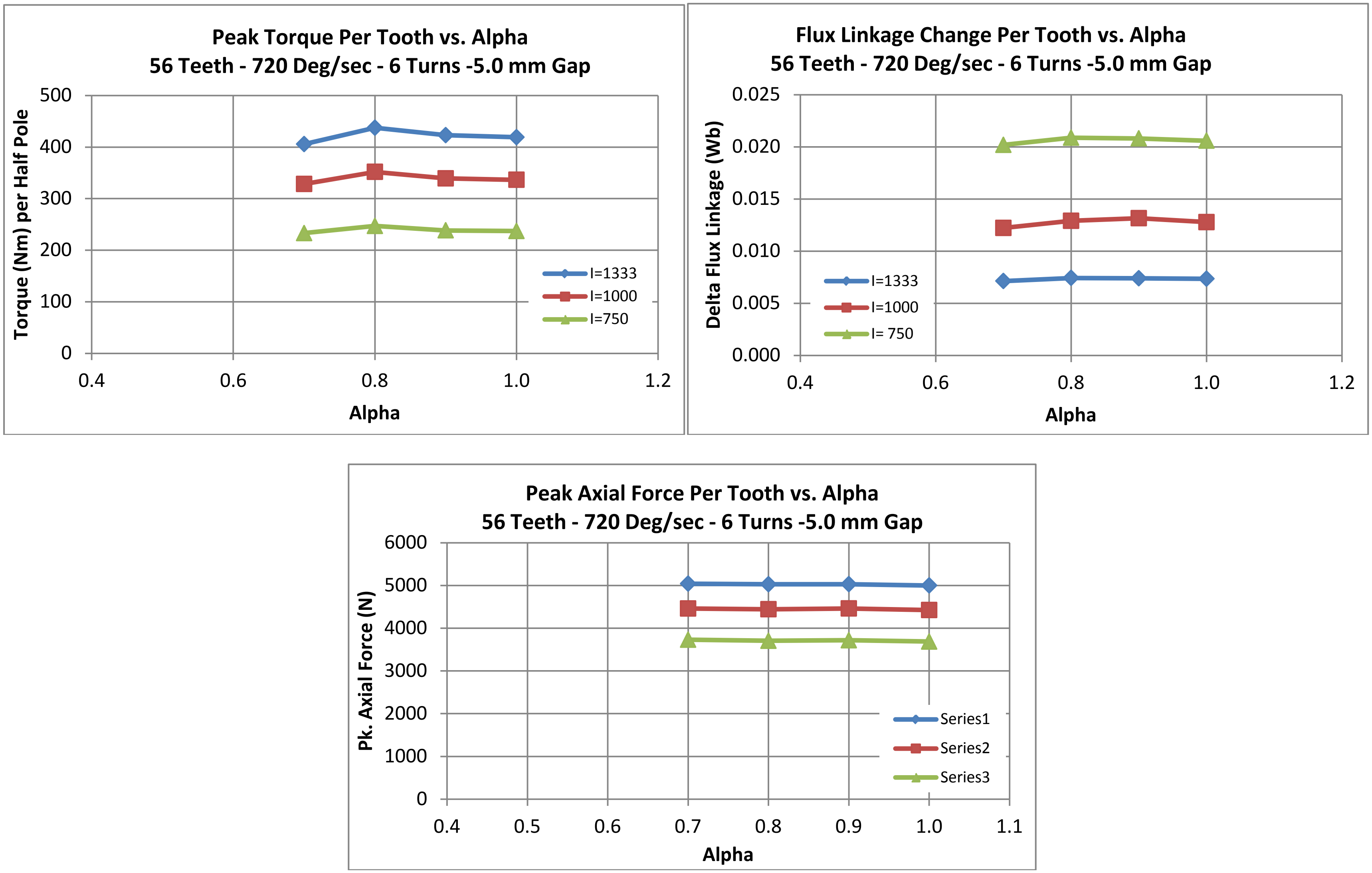

Figure 13 - Alpha Variation Results: Torque, Flux Linkage, and Axial Force

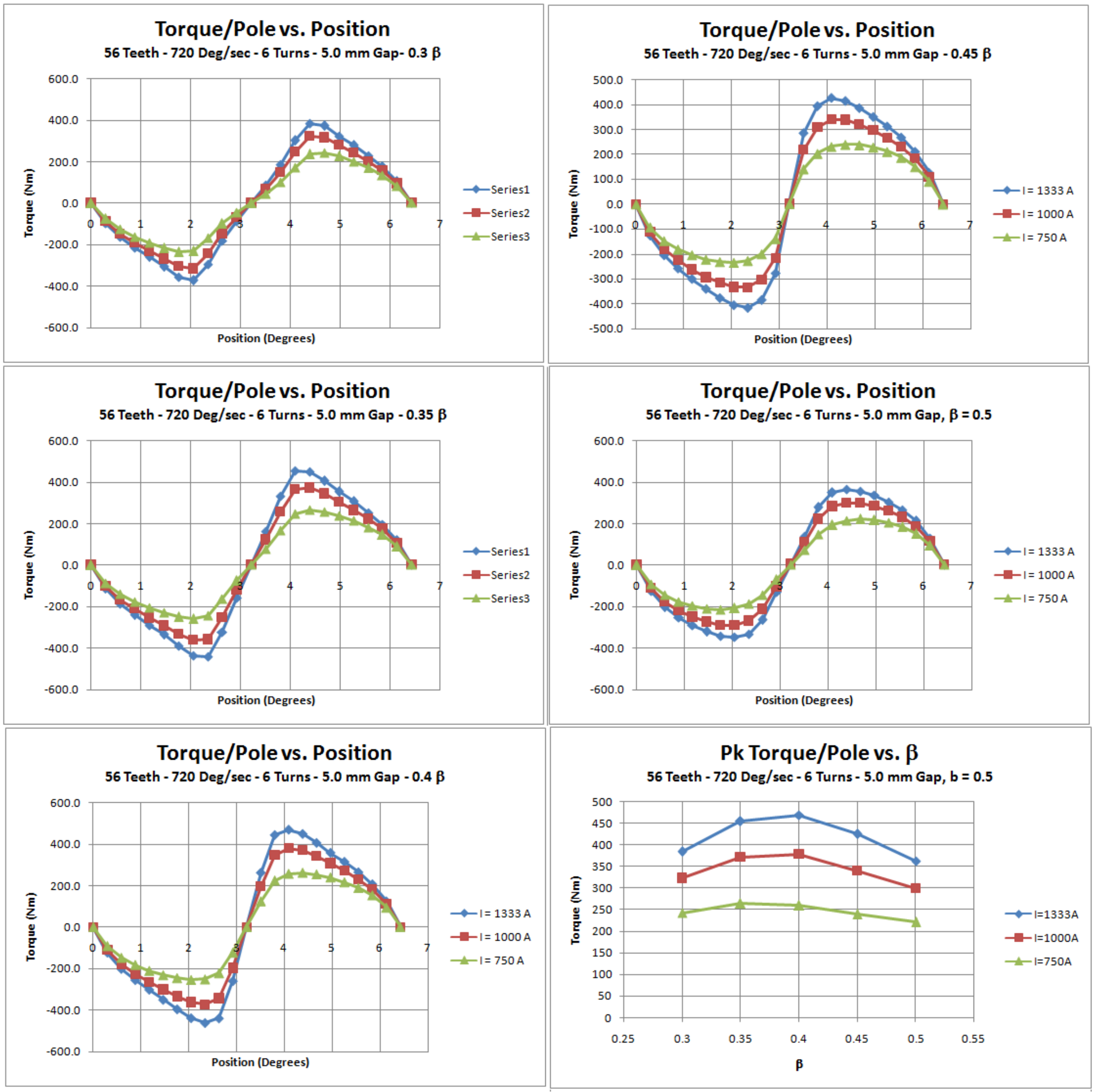

Figure 14 - Beta Variation Results, Torque vs. Position

Figure 14 illustrates there is a noticeable effect of Beta on the shape (i.e., Harmonics) of the torque vs. position curve and an increase in peak force. The peak torque varies with between $\beta = 0.4$ and 0.35 depending on the NI, most likely due to saturation effects. There is also a noticeable change in flux linkage as illustrated in Figure 15. The summary plot in Figure 15, Bottom Right shows the maximum variation in flux linkage with position is at $\beta = 0.4$.

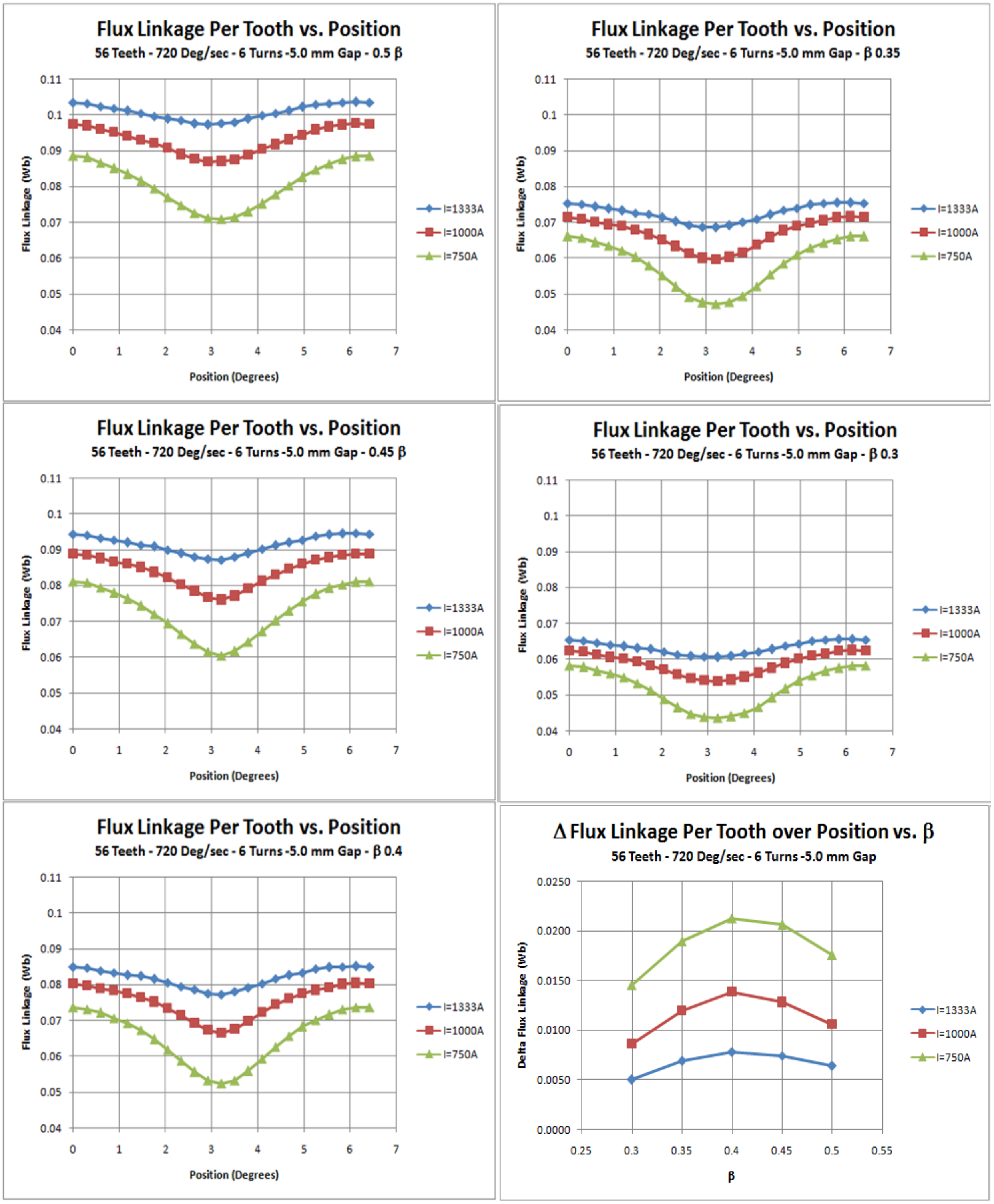

Figure 15 - Beta Variation Results, Delta (Δ) Flux Linkage vs. Position

Maximizing the Flux variation over position is desirable to maximize the SR Machine's power output, as can be seen by the second term in Equation 1[1], of the SR Generator Phase - Equivalent Circuit, Figure 16, which relates to the magnetic energy stored in the air gap.

$$p_i = vi = R_s i^2 + i^2 \frac{dL(\theta,i)}{dt} + L(\theta,i) i \frac{di}{dt}$$ **Equation 1**

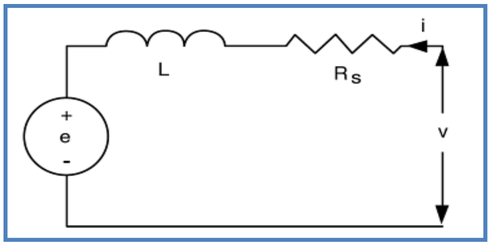

Figure 16 – Switched Reluctance (SR), Generator Phase, Equivalent Circuit

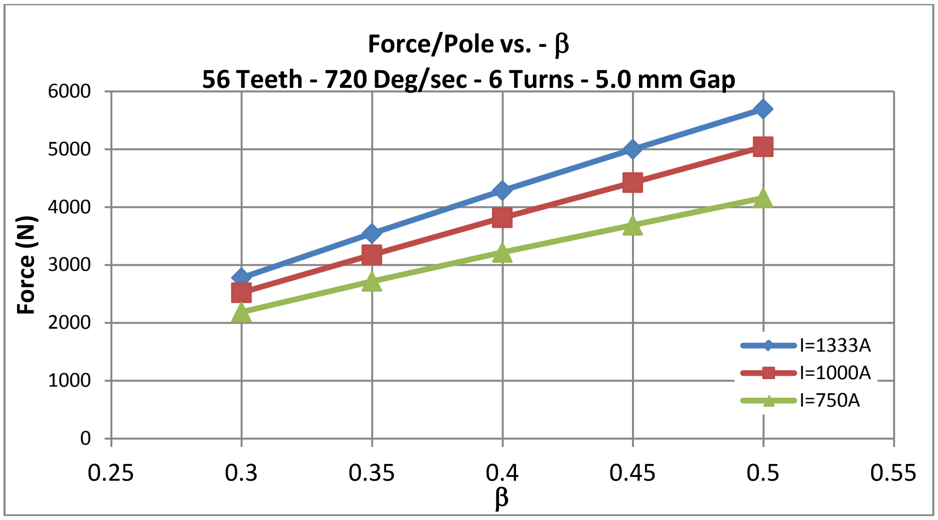

Figure 17 - Beta Variation Results, Peak Axial Force/Pole

Figure 17 shows the peak axial force corresponding to the aligned tooth condition decreases linearly with decreasing Beta. The negative magnetic stiffness also has a corresponding decrease with Beta.

Parallel vs. Angular Sided (Tapered) Tooth Structure

The shape of the rotor and stator tooth is a design issue to be evaluated. The tooth can be designed to have sides that are rectangular (as shown in Figure 5 and in Figure 18 Left) or with a fixed angular span between the sides whose planes pass through the center axis (Figure 18 Right). The rectangular stator tooth edge engages the rectangular rotor tooth edge at the inner radius first, and progresses radial outward over the range of rotation. Alternatively, the latter angular wedge shaped configuration is the most analogous to the radial gap SR machine. As the rotor tooth moves from the unaligned to an aligned orientation, the entire edge of the rotor and stator teeth align at the same rotational position.

[1] "Switched Reluctance Motor Drives: Modeling, Simulation, Analysis, Design & Applications", R. Krishnan, 2001, CRC Press, Industrial Electronics Series

The difference in the engagement progression may or maybe not be an issue for the electrical system, but it is relevant that the shape of the machine voltage waveform (the consequent harmonic content) and force versus position is different for the two configurations.

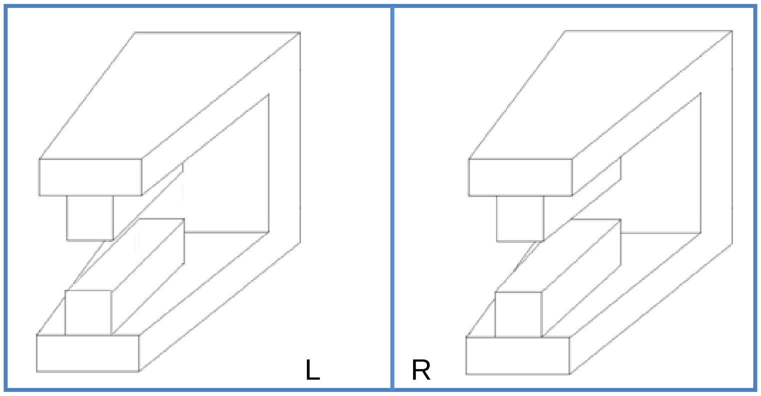

Figure 18 - Stator Tooth Structure - Parallel (L) and Angular Sides (R)

To facilitate construction, parallel sided teeth were identified as a preferred method to use with lamination construction. FEA shows there is a significant increase (25%) in machine performance even though the edges of the parallel sided teeth of Figure 19 do not engage all at once over the tooth length as is the case with teeth that are angular sided.

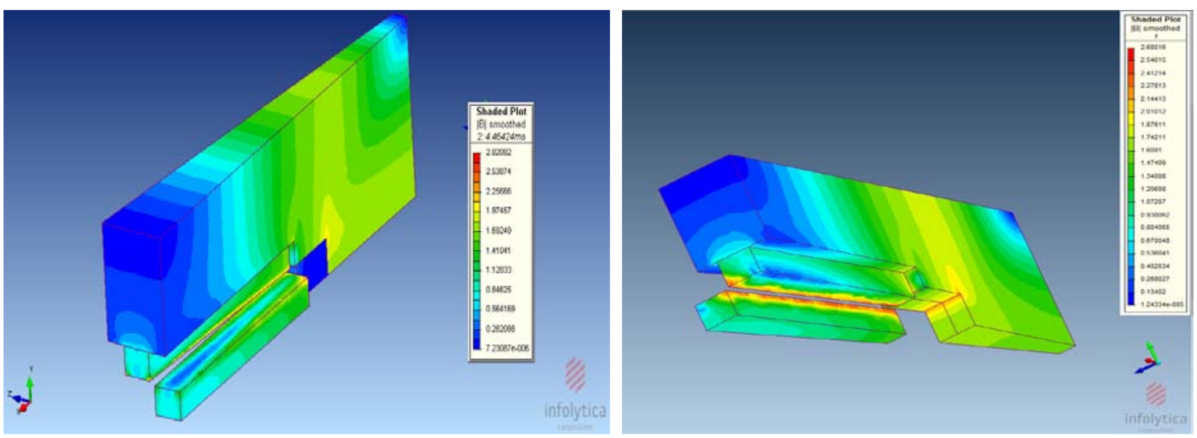

Figure 19 – Parallel Side (L) vs. Angular Side (R), Flux Plots

The following three figures illustrate the tooth alignment issue and the impact to three key parameters, torque (Figure 20), flux linkage (Figure 21) and axial force (Figure 22). Three (3) values of current flow are provided to illustrate performance for each of the key parameters.

The parallel teeth concentrate flux (ϕ) when aligned and have larger leakage reluctance when unaligned yielding higher forces and flux variations. Parallel teeth also change the harmonics in the flux vs. position waveform. The harmonic modifications will also be present in the time varying voltage (v) waveform because $v(t) = (d\phi/d\theta)\cdot(d\theta/dt)$.

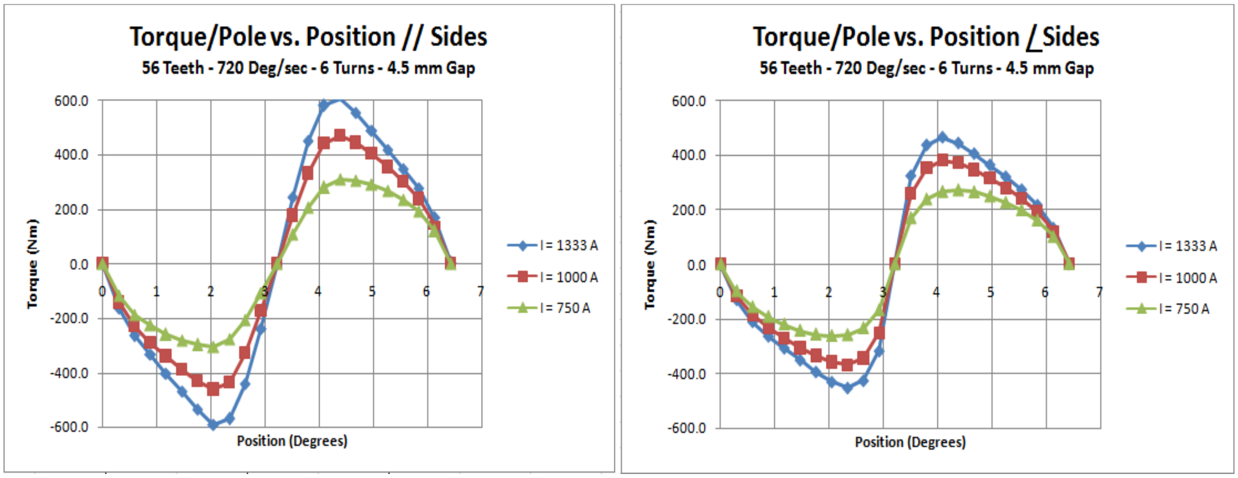

Figure 20 - Parallel Side vs. Angular Side, Torque per Pole vs. Position

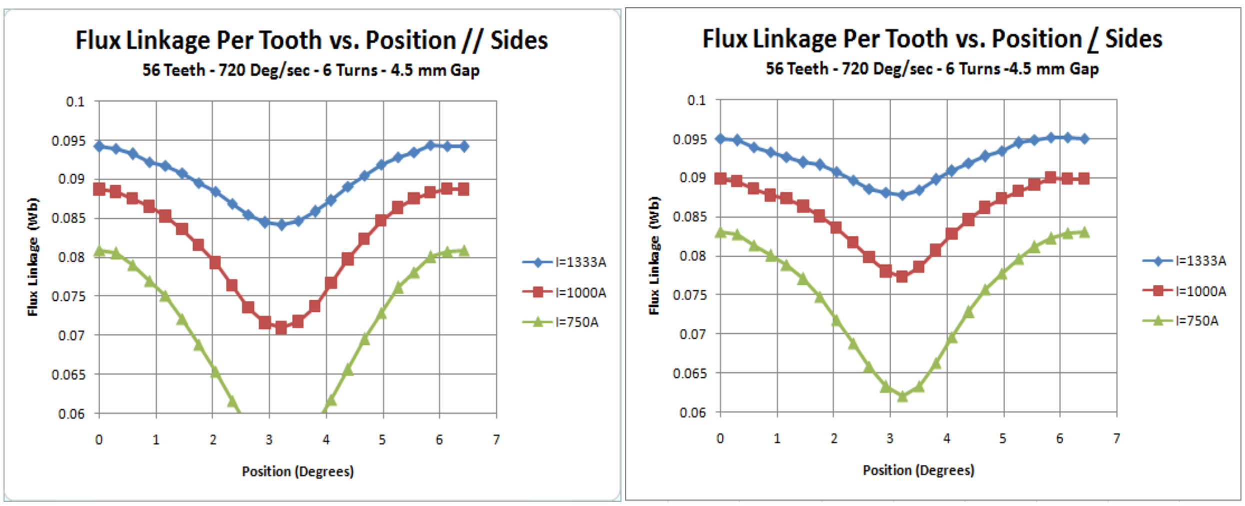

Figure 21 – Parallel Side vs. Angular Side, Flux Linkage per Pole vs. Position

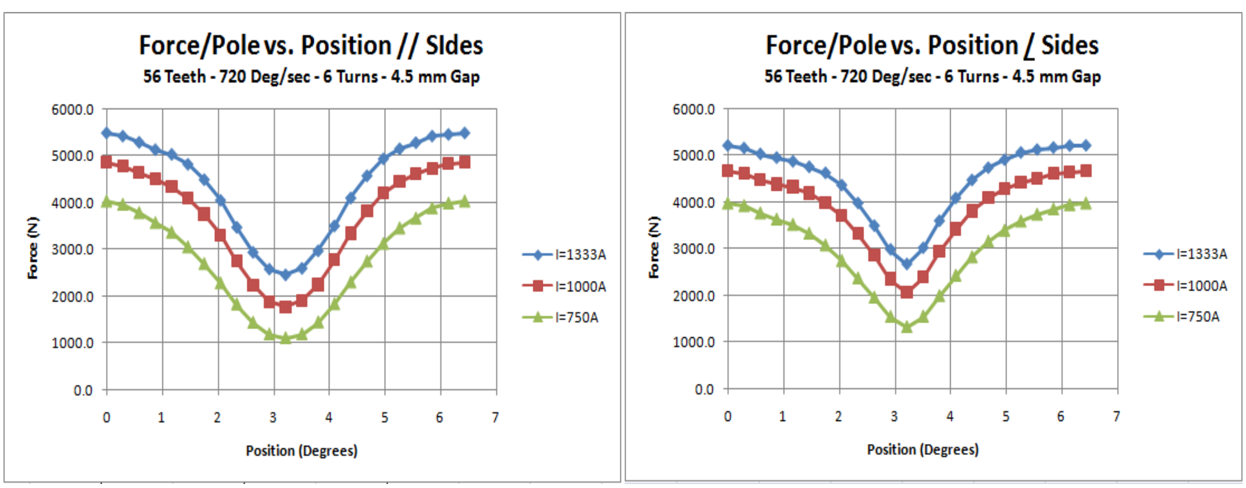

Figure 22 – Parallel Side vs. Angular Side, Axial Force per Pole vs. Position

Parameter Variation of Teeth with Parallel Sides

For the parallel sided tooth the β parameter no longer has the same meaning so tooth width (Wt) has been used as a variable for the parametric evaluation. Figure 23 shows the Torque/Pole variation with Wt. The graph in Figure 23 lower left shows there is a leveling off in the peak force as the tooth width falls below 0.24 and little change in the torque waveform harmonics.

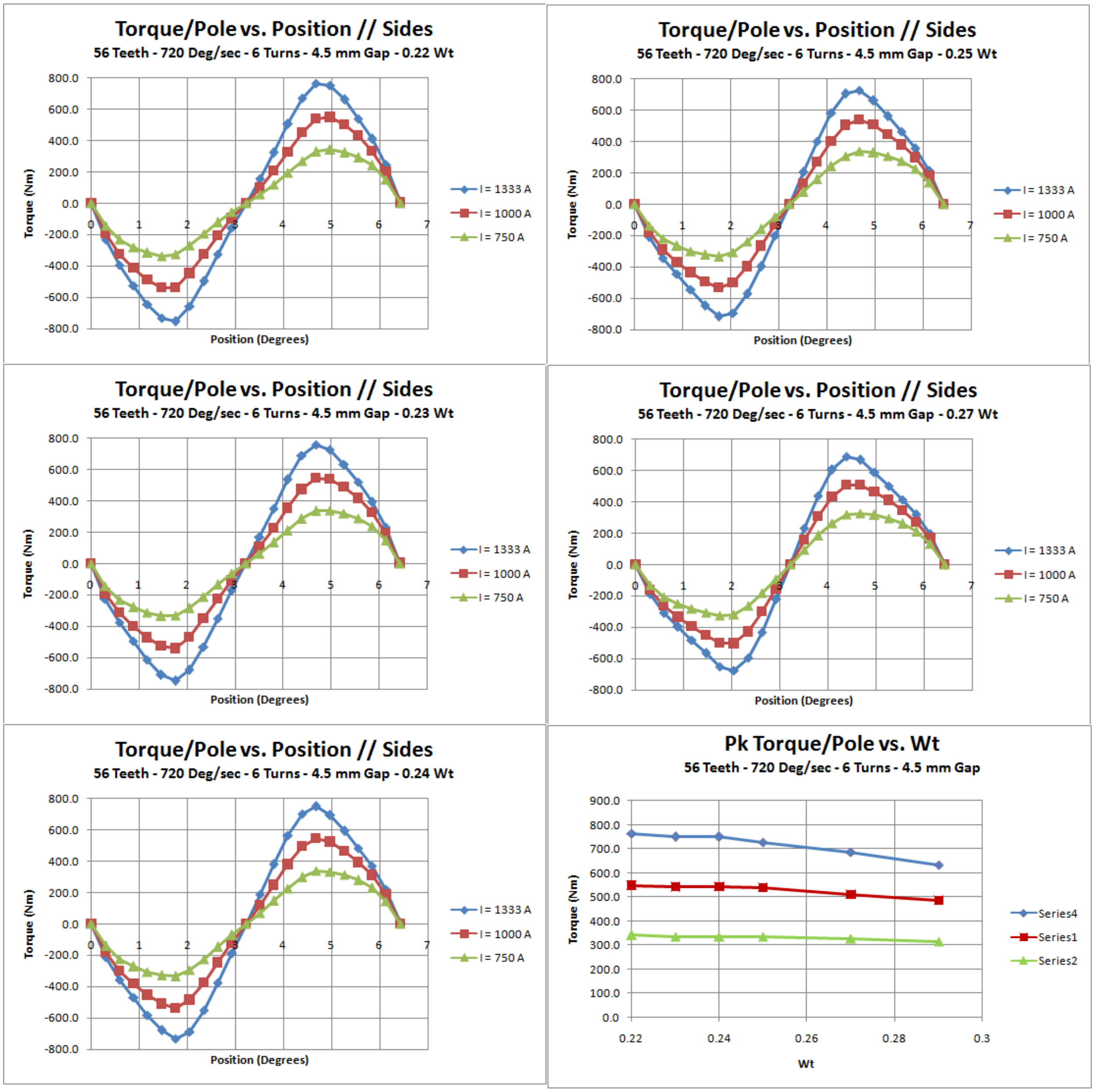

Figure 23 - Parallel Side Wt Variation, Torque per Pole vs. Position

Figure 24 shows a similar behavior in the Delta Flux Linkage Variation vs. Position, most likely due to saturation, at the highest current level.

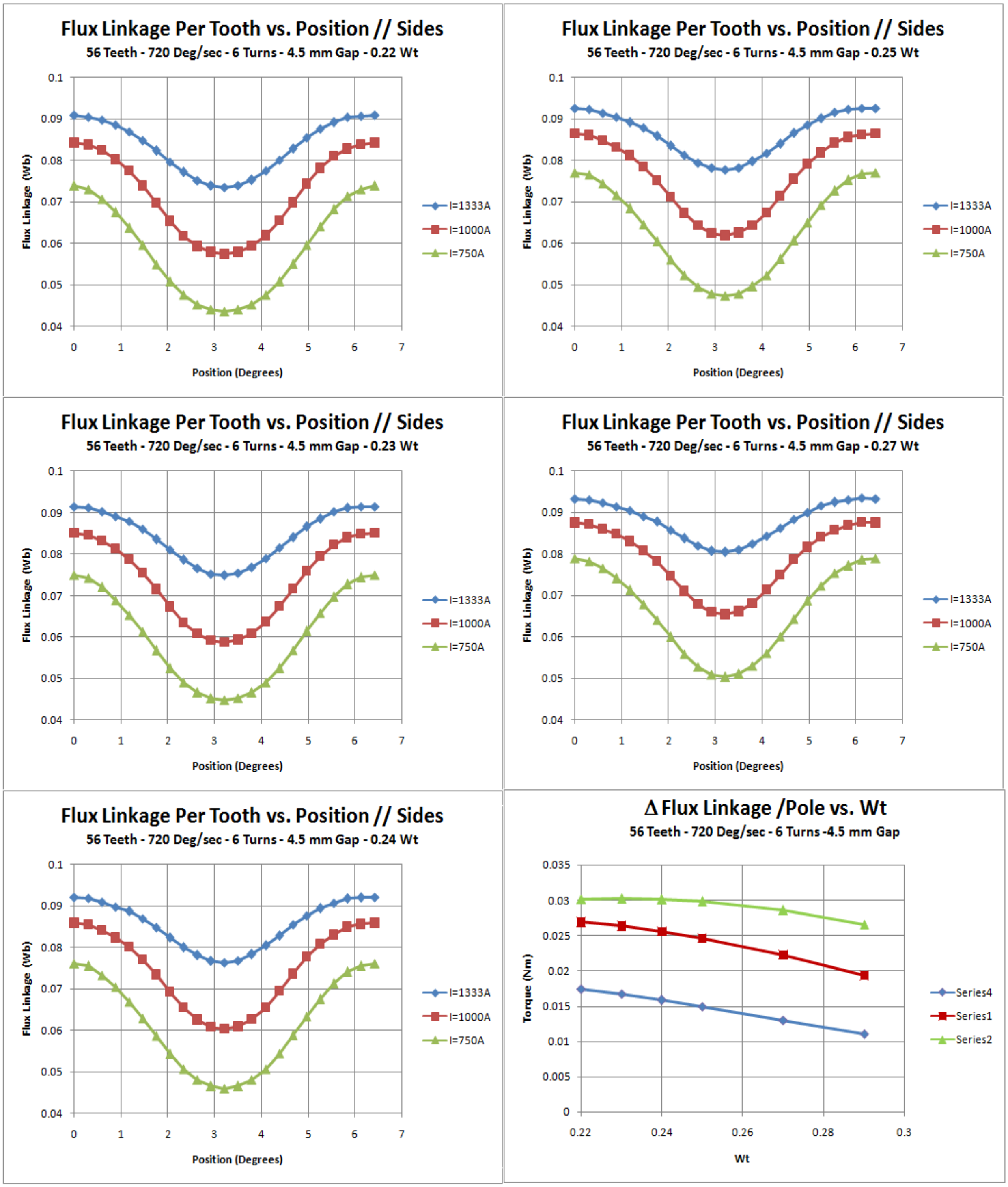

Figure 24 - Parallel Side Wt Variation, Flux Linkage per Pole vs. Position

Figure 25 shows the axial force decreases with decreasing Wt for the lowest current value and a leveling off for higher current values; again most likely due to material saturation.

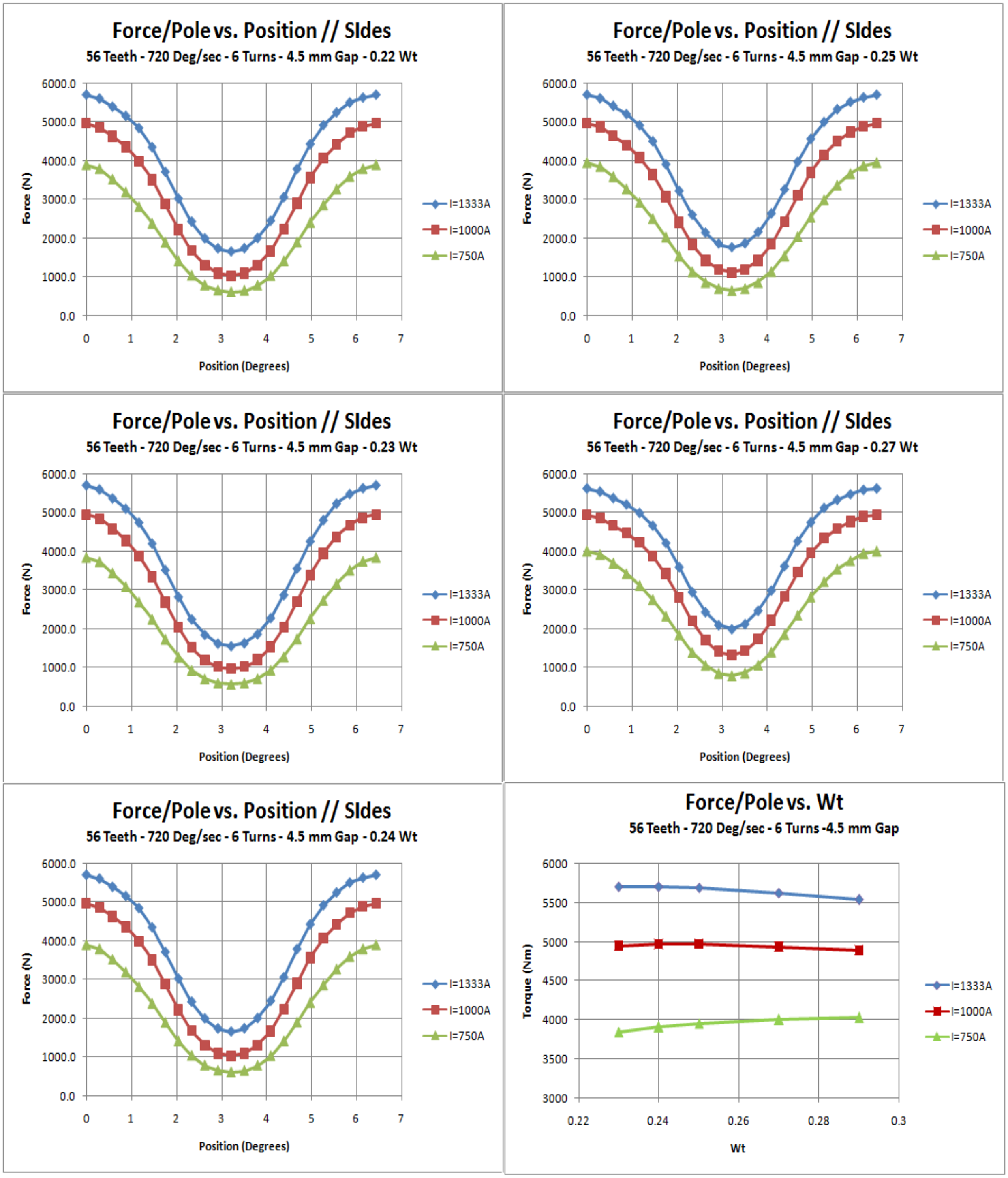

Figure 25 - Parallel Side Wt Variation, Axial Force per Pole vs. Position

A Core Material comparison between 1010 Steel and M19 Steel was performed with little sensitivity to the performance found, as illustrated in Figure 26.

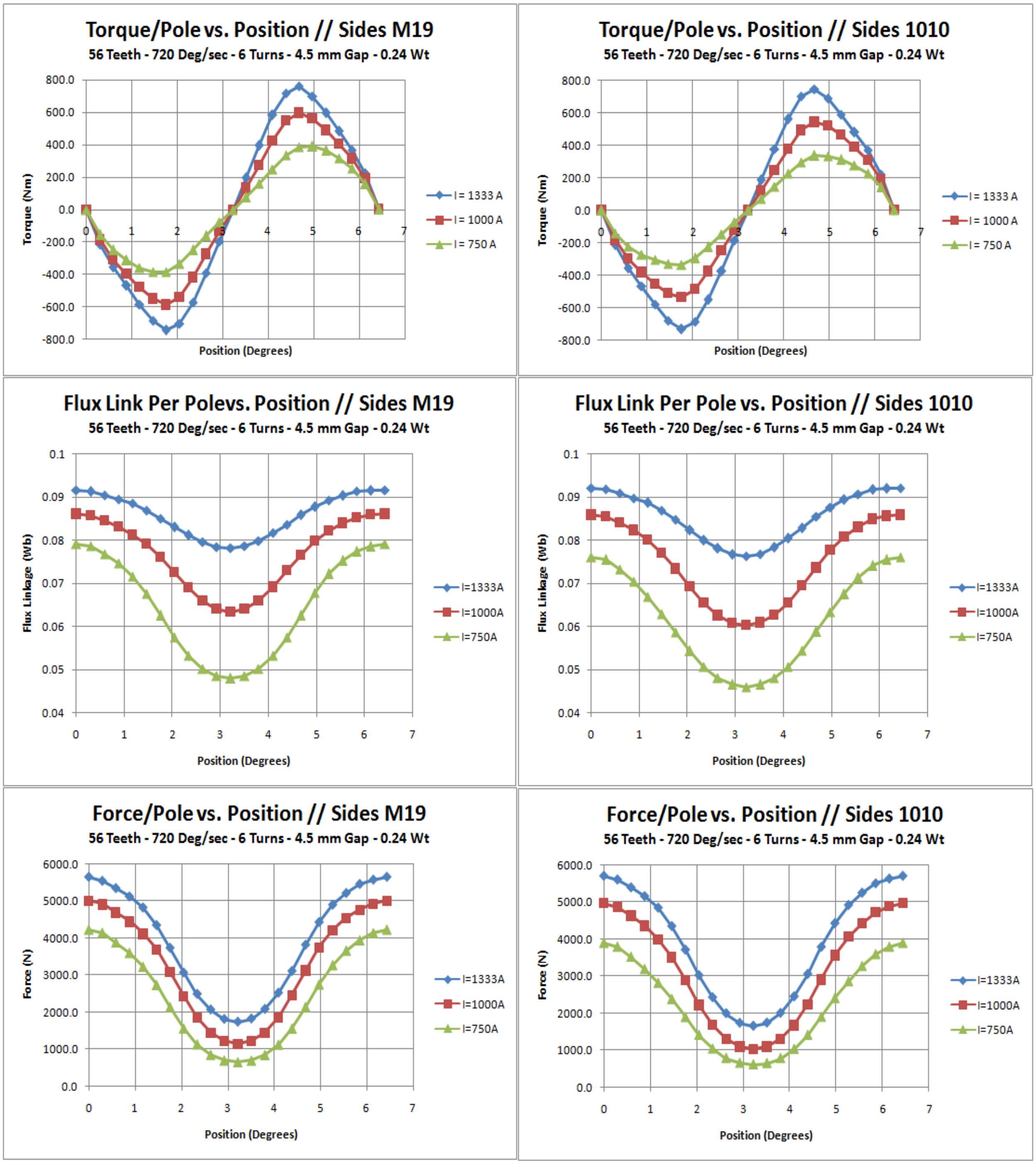

Figure 26 - Parallel Side 1010 & M19 Steel, Axial Force per Pole vs. Position

Transition of design approach to multi-coil winding and more conventional flux paths

The design and simulation of the two single coil winding versions showed that despite the benefits to winding only a single coil versus many individual pole coils the large thickness of iron in the axial direction as back iron to get the flux along to the teeth as well as the back iron channeling the flux around the coil increase the dimensions and weight to where desired benefits against the radial machine were not realized. Accordingly, as mentioned in the first quarterly report, the next focus was on an axial flux design that does not require radial channeling of the flux along the radially directed teeth of the axial flux machine. Most of the simulation and trade-offs above are relevant to the dimensions of the rotor / stator pole / slot structure.

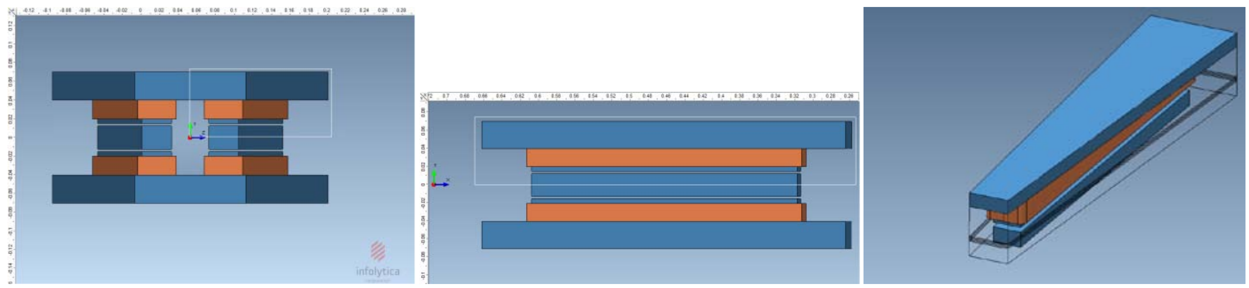

Figure 27 – Multi Coil Axial Gap SRM FEA Model

The flux density plot of Figure 28 illustrates how the magnetic flux now travels axially through teeth and then splits, traveling circumferentially through two parallel paths in the disk of iron (top wedge in the FEA model shown in Figure 27) that supports the stator tooth. No flux path is needed at the ID or OD as was the case with the single coil configuration. The coil on each tooth structure has a lower mass of material than the single coil configuration. The lower weight comes at the cost of an associated increase in complexity of multi coil connections. This configuration is most similar to an axial embodiment the baseline radial gap SRM.

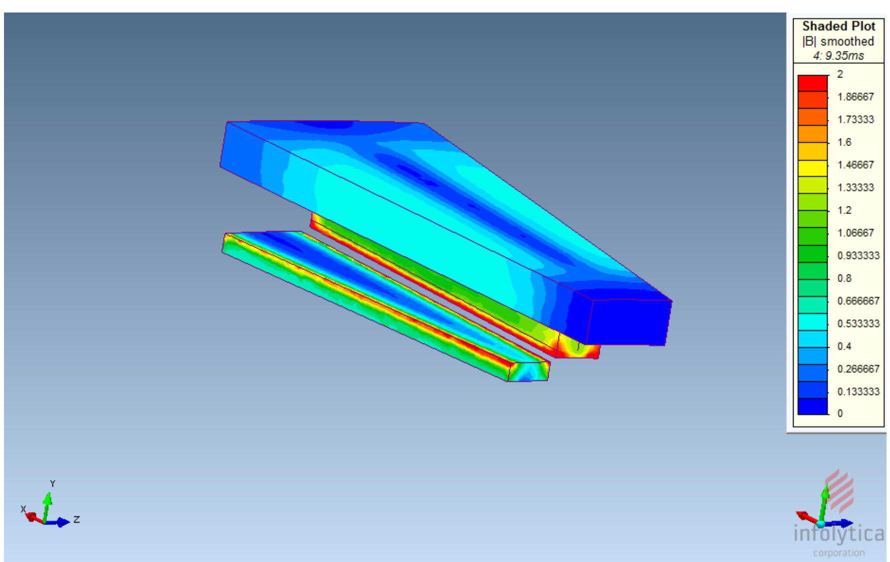

Figure 28 – Multi Coil Axial Gap SRM FEA Result - |B| Flux Density Plot

Figure 29, Figure 30, and Figure 31 plot the torque, flux linkage and axial force for a 28 tooth case with a 2.5 mm gap.

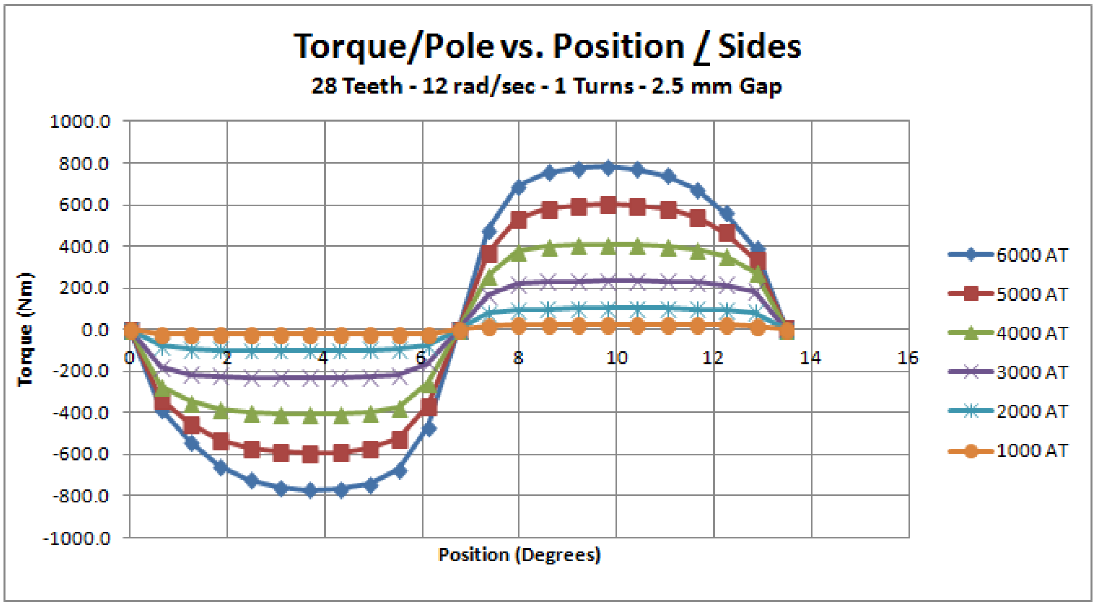

Figure 29 – Multi Coil Axial Gap SRM FEA Result - Torque versus Position

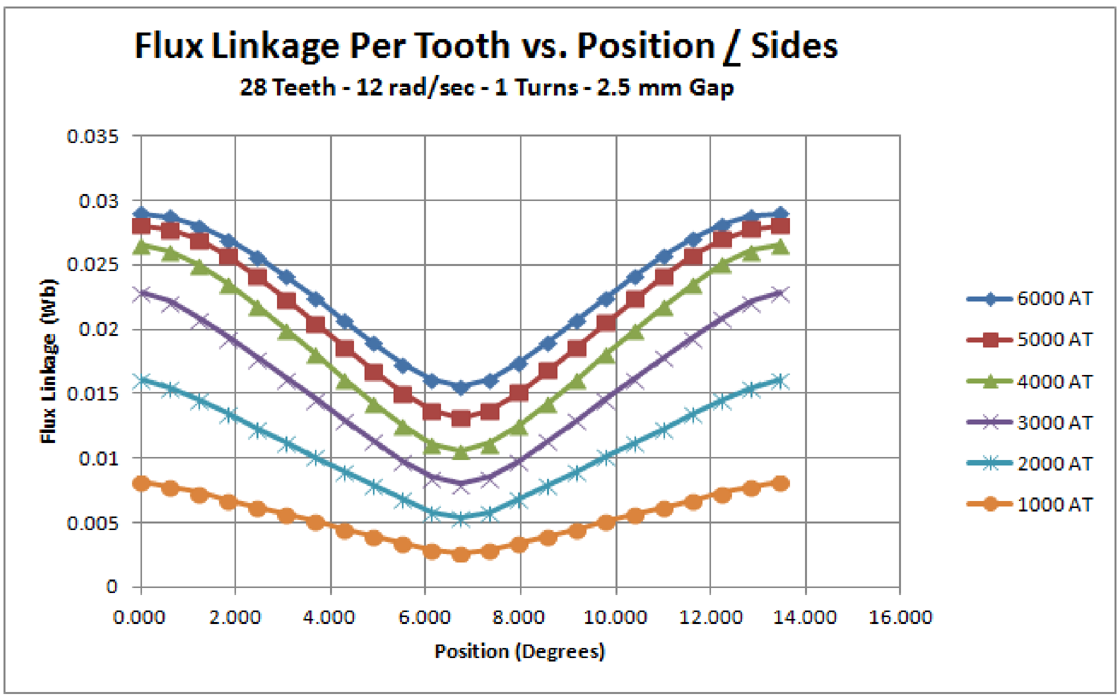

Figure 30 – Multi Coil Axial Gap SRM FEA Result – Flux Linkage versus Position

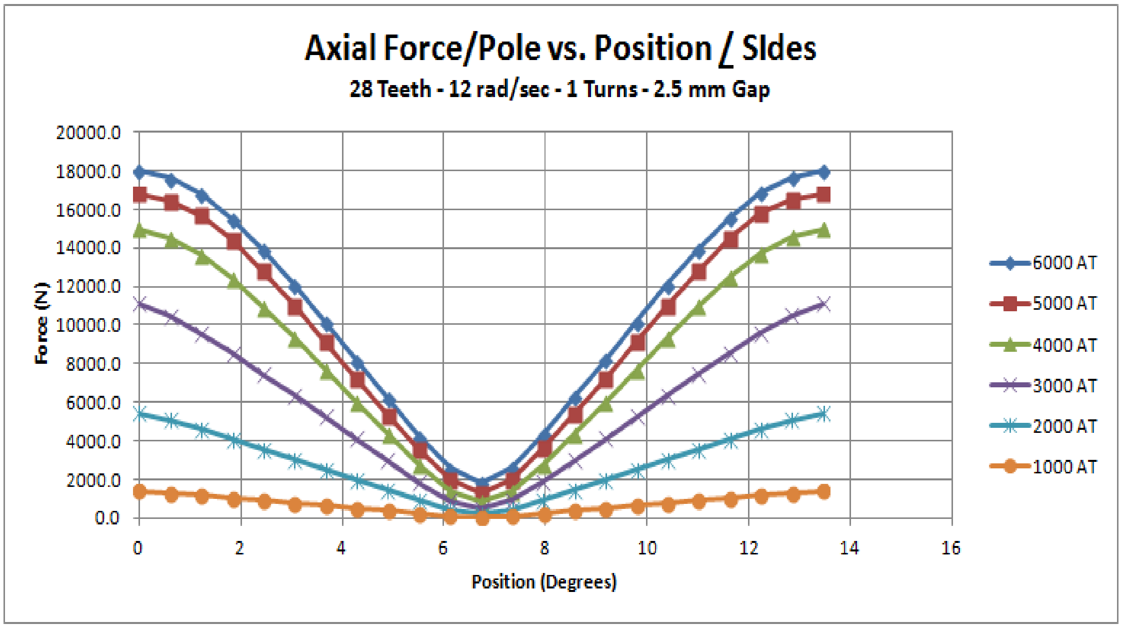

Figure 31 – Multi Coil Axial Gap SRM FEA Result – Half Tooth Axial Force versus Position

Significant results (Task 2)

The value of taking time to parameterize the 3D FEA models facilitated the study of key parameter variations and led to the discovery of benefits of the straight tooth with a radially diverging slot taper in high tooth count configurations.

Key outcomes (Task 2)

Both single coil approaches, while elegant from a winding connection and configuration point of view, incur a high penalty in the back iron increasing the weight, the axial length and the phase inductance of the machine over that which would be desirable, though the machine would still be smaller than the radial machine. The parametric 3D model was readily adapted to a multi coil configuration, in subsequent analyses, to deal with the penalties of the single coil approach.

Task 3: Preliminary Manufacturing Process and Cost Analysis

Specific objectives (Task 3)

As with the switched reluctance machine of the original project, the Axial Flux Reluctance Machine must be designed with the manufacturing process in mind to ensure that the machine can be manufactured in volume at the lowest possible cost, using standard manufacturing processes. The manufacturing process was considered in this task and a preliminary manufacturing plan was created. A preliminary bill of materials was used to estimate production costs for the machine.

Major activities (Task 3)

For the same reason that 3D analysis is required to handle the flux simulation in the axial machine, the manufacture of the machine involves directions of flux flow that require clever orientation of the magnetic material. An important objective is the economically manufacture-able configuration of magnetic laminations related material composite structures. This involves not only the shape of the structure but an insight into a practical assembly process.

Manufacturing and Assembly Issues

Structural design of the axial gap SR machine has unique and demanding requirements. The assembly must achieve and maintain small, equal clearances on both sides of the rotating elements (rotor), inside the stationary element (stator). Magnetic and electrical material properties of the assemblies, as well as construction features (e.g., lamination) are paramount in meeting performance goals.

Axial Gap Machine Structural Support and Negative stiffness

A key design issue is the structural stiffness of the assembly; the structure must be stiff enough to prevent the magnetic field induced, negative stiffness from causing significant deflection or loss of mechanical clearance. Preliminary design efforts used a homogeneous disk approximation to evaluate structural support options. Closed form equations from Roark's Formulas for Stress & Strain, 6th Edition, were used in a spread sheet to evaluate the fundamental design requirements for the types of axial machines being considered.

A two sided Finite Element Model (FEA) was generated by mirroring the existing FEA model about the x-z plate, as illustrated in Figure 32 to confirm axial stiffness predictions based on the half model. Given the non-linear nature of phenomenon, importance in the machine structural design, and the overall axial length, this effort was considered prudent. In this static FEA, the rotor is offset axially in the gap by -10%, 0 & 10% and the resulting change in force is used to calculate the static stiffness at the rotationally aligned position. The static case FEA per pole stiffness of -4.50E5 N/m (Table 2) compares favorably with the estimated value of -4.33E5 N/m from rotary dynamic FEA results.

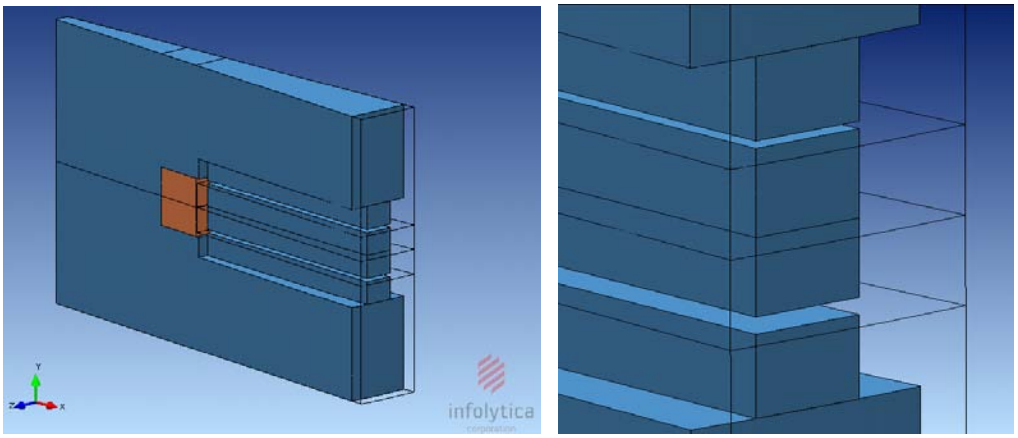

Figure 32 - Axial Stiffness FEA Model (L) and Gap Close-Up (R)

Exaggerated Offset, Single coil machines

Table 2 - Axial Stiffness, Rotationally Aligned Static Case

STATIC SOLUTION					
		NT	56		
gap	0.005	m	Dg	0.0005	m
Rotor Per Pole	Stator Per Pole	Avg of Abs	Per Pole	Per Phase	Per Pole
Force(N)	Force(N)	Force(N)	K (N/m)	K (N/m)	Flux Linkage(Wb)
203.0	-237.3	220.1	-4.40E+05	-2.47E+07	0.0404
177.7	-208.4	193.0	-3.86E+05	-2.16E+07	0.0313
150.3	-176.9	163.6	-3.27E+05	-1.83E+07	0.0238

With the multiple coils per phase SRM configuration having a different magnetic circuit than the single coil per phase, another negative stiffness analysis was performed. The same method used with one coil per phase design (Figure 32) was employed. By mirroring the model about the centerline of the tooth, as illustrated in Figure 33, a FEA model was generated with minimal effort. With odd periodic boundary conditions applied on the two side faces, the aligned rotor tooth was displaced axially and the change in axial force used to calculate the axial negative stiffness on a per pole or tooth pair basis (Table 3).

Note that this analysis is sensitive to the mesh size in and around the gap. The difference in the axial force (Fy) magnitudes at the same NI is a measure of the analysis accuracy; an error of ~1% is found in the results. As expected the axial force on the rotor at the centered position is zero, but the stiffness is still present.

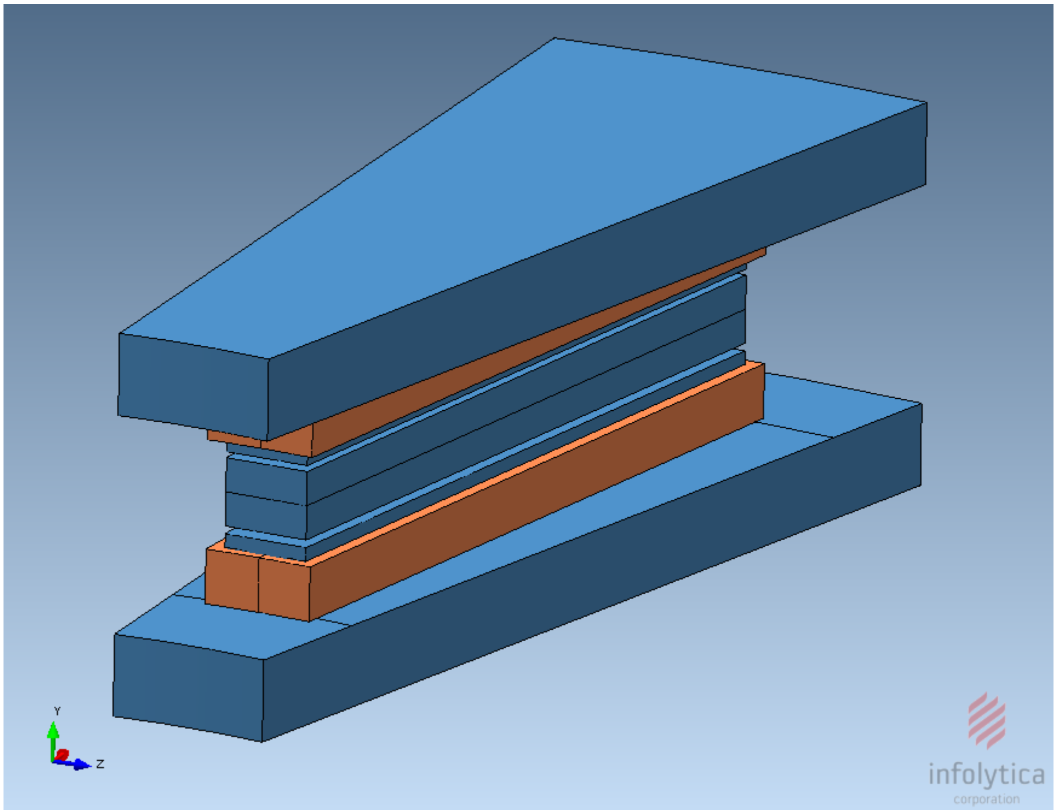

Figure 33 - Negative Stiffness Model Multi-coil machine

Table 3 – Negative Stiffness Analysis Results

	Δg(m)	-0.0003	Δg(m)	0.0003	Average
NI (AT)	Force(N)	Stiffness (N/m)	Force(N)	Stiffness (N/m)	Stiffness (N/m)
0	0	0	0	0	0
1000	82.8	-2.76E+05	-78.2	-2.61E+05	-2.68E+05
2000	327.9	-1.09E+06	-302.6	-1.01E+06	-1.05E+06
3000	621.4	-2.07E+06	-589.1	-1.96E+06	-2.02E+06
4000	782.2	-2.61E+06	-746.9	-2.49E+06	-2.55E+06
5000	817.7	-2.73E+06	-796.1	-2.65E+06	-2.69E+06
6000	843.2	-2.81E+06	-803.0	-2.68E+06	-2.74E+06

Figure 34 shows the stiffness plot vs. current levels, on a per tooth pair basis for the aligned teeth case. The stiffness begins to roll off with NI at and above the 4000 AT range due to saturation effects. Based an approximate worst case -4E6 N/m stiffness result and multiplying by the number of teeth pairs (28) a phase stiffness of -1.1E8 N/m is calculated. Series combination of the stiffness of all mechanical elements in the structural path should have a resultant stiffness on the order of 1.1×10^9 N/m per phase. The negative stiffness must also be considered when evaluating structural resonances because the reduced stiffness lowers the resonant frequencies.

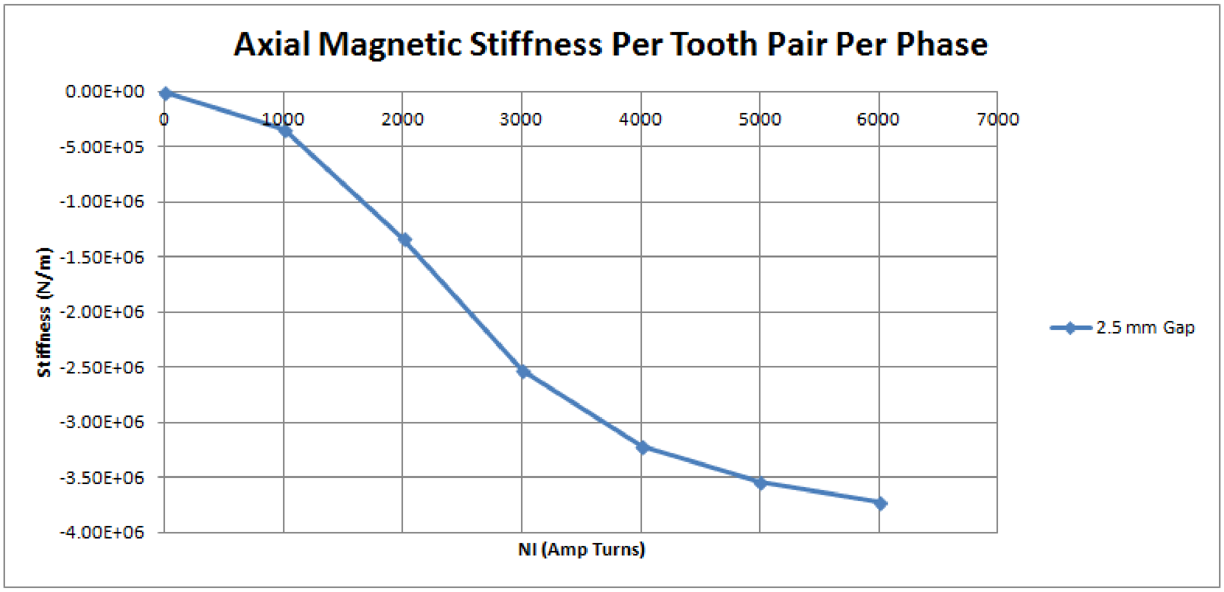

Figure 34 - Axial Stiffness versus NI - 2.5 mm gap

Torsional Negative Stiffness Estimation

In addition to the negative axial magnetic stiffness, the SRM machine also has a negative torsional magnetic stiffness that must be considered in the machine design. Given the size limit on the FEA analysis, performing a torsional stiffness analysis of an entire rotor is not feasible. Therefore, the torsional stiffness is calculated from the tooth pair analysis results.

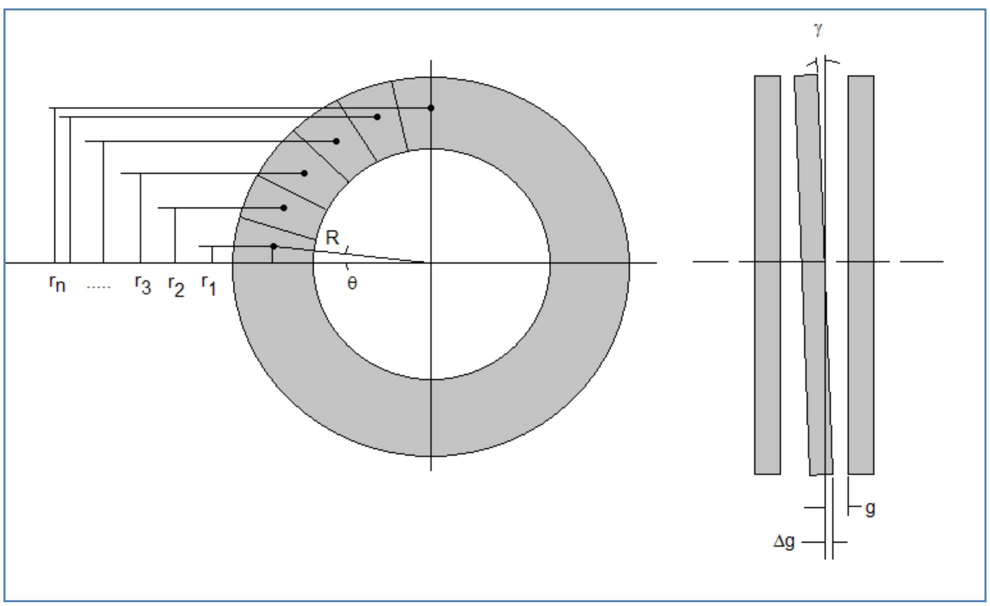

Figure 35 - Angular Negative Stiffness - Angular Displacement of the Rotor between Parallel Disks

Using Figure 35 for reference, the following describes how the negative angular stiffness about the x or z axes or any axis in between is estimated; y is the spin axis. Let NT be the number of teeth on each disk side. The stiffness is calculated from the following:

$K_\Theta = T / \gamma$

$T = \Sigma T_n = \Sigma r_n F_n$

$F_n = C I^2/g_n^2$

$r_n = R_m \sin \theta_n$

$g_n = (g+\Delta g_n)$

$\Delta g_n = r_n \sin \gamma$

$T = \Sigma (C I^2 R_m \sin \theta_n)/(g+\Delta g_n)^2$

$\theta_n = (2n-1)\theta$

$\theta = 2\pi/2NT$

N= 1 to NT

From the axial stiffness analysis, the peak forces and negative stiffness occur when the teeth are aligned; the same is true for the angular stiffness. For the maximum angular stiffness, the aligned tooth position is used and an angular displacement gamma (γ) is assumed about any axis normal to the spin axis (y-axis). The resulting change in gap (Δg) at the midpoint of each tooth is found. Using the Δg at each tooth, an estimate in the change in force for each tooth is calculated and using the distance from the axis of rotation the torque is calculated. Summing the resultant torques for all the teeth and dividing by the angle yields the estimated angular stiffness. Only one quadrant need be analyzed and the result multiplied by 4 times to obtain the total angular stiffness value between the rotor and stators of one phase. Table 4 summarizes the result.

Table 4 – Negative Torsional Magnetic Stiffness Analysis Result

Parameter	Value	Unit
No. Teeth	28	
No. Teeth per Q	7	
Mean Radius	0.464	m
Nominal Gap	0.0025	m
Max Delta Gap	0.0003	m
Angular Tilt	0.000647	radian
Pole Span	0.2244	radian
Force	823	N
Torque	1325	Nm
Torsional Stiffness	8.20E+06	Nm/rad

Appendix C has background on negative stiffness. Appendix A has information on Disk Stiffness.

Rotor Construction

In Figure 36 are illustrations of several fabrication options, which include a solid, compressed powder and three lamination configurations. To minimize magnetic field (B) induced eddy currents (J) in the tooth (Figure 36a) it is desirable to construct the rotor tooth from powdered metal (Figure 36b) or laminated material (Figure 36c, d, & e).

Powdered metals can be formed and machined to shape or Hot Isostatically Pressed (HIP) into final form with a significant investment in capital tooling. Pressed parts are usually limited in size due to the high forces required to press large parts. Also, to achieve high density and good magnetic properties, Hot Isostatic Pressing (HIP) of powdered metals usually end up with high Eddy current losses.

With computer controlled laser cutting methods, option **c** is feasible, but adds a sorting task during in assembly. Option **d** requires tapered laminations which are not impossible, but more costly as lamination sheet mills will not accept this work, so a secondary rolling step is needed to impart the taper. Grinding each piece will also work, but is too costly for large assemblies.

Alternatively, a laminated block can be assembled and then machined into final shape (Figure 36 **c** & **e**). Option (Figure 36 **e**) uses uniform thickness laminations but requires machining after assembly and relies on bonding material to hold the outer most laminations in place. An etching process is also needed to clean up the smeared material that shorts the laminations together during milling and/or grinding operations. Wire EDM (electro discharge machine) can avoid the need for etching, but may be more costly. Both machining methods are in use today.

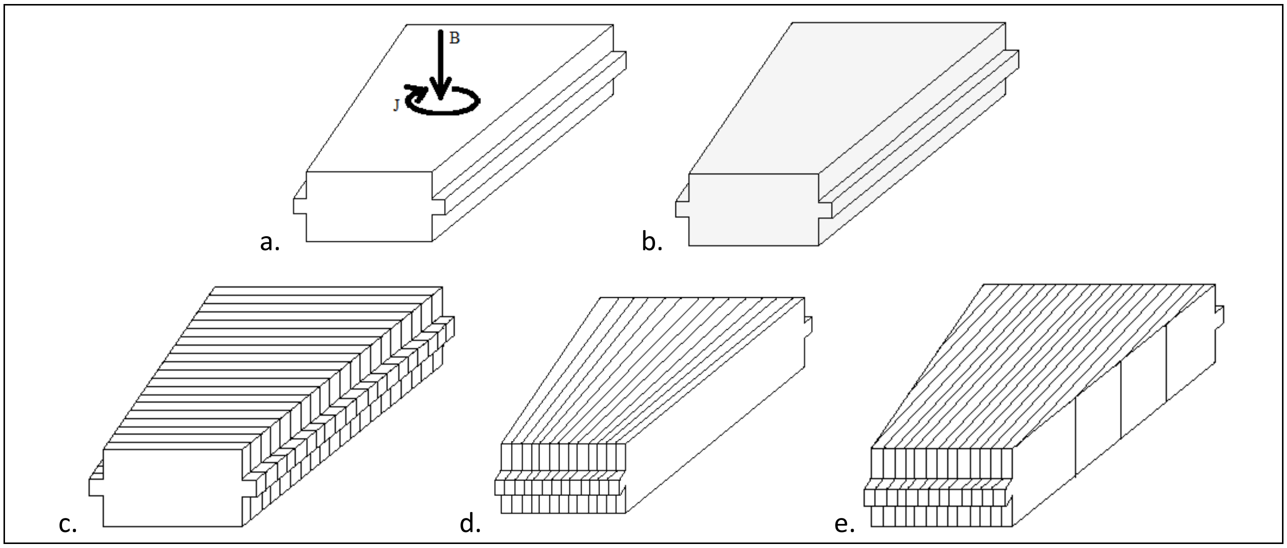

Figure 36 - Tapered Rotor Tooth Construction Options

In addition to the wedge shapes, rectangular shapes with parallel sides are practical, Figure 37. They may be built by methods similar to Figure 36 **c** and **e**.

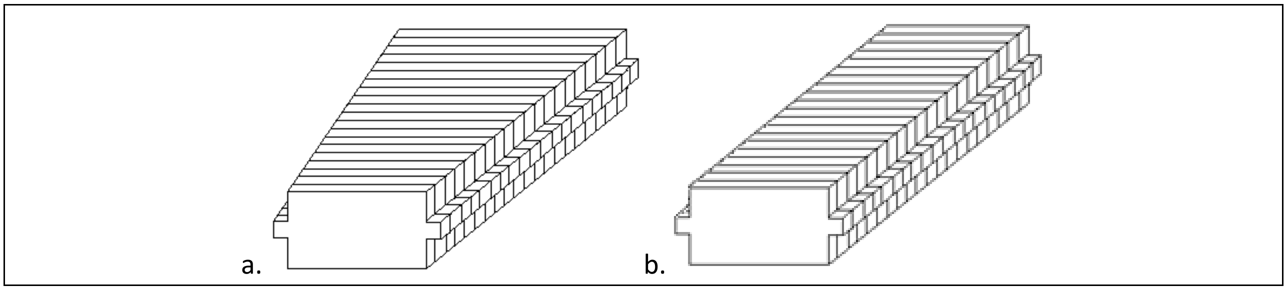

Figure 37 - Rotor Tooth Construction - Tapered vs. Parallel Side

RCT recommends tapered tooth fabrication of a prototype machine using the configuration of Figure 36 **c** and volume production should consider utilizing powered metals if production is practical and performance is acceptable. However, if the parallel sided tooth, Figure 37 **b**, can be used, it is the most preferred due to the identical laminations, ease of assembly and no need for machining.

Stator Construction

Stator construction may consist of a complete solid (e.g., casting), two identical halves joined at the equator or two plates and a ring. The stator may also be assembly of angular C-cores segments, as illustrated in Figure 38 for the rotor inside configuration. The following discusses stator fabrication options and trades, as each configuration has assembly and tolerance issues. Similar configurations for the rotor outside configuration exist but are not presented for ease of discussion in this section. For all options, the stator must enclose a toroidal coil. It is preferable for the coil to be prefabricated and the stator assembled around it. However, the coil may be wound in place for the rotor outside configuration with relative ease. That is not the case for rotor inside configuration. Therefore, assembly of the rotor inside configuration should accommodate the pre-wound coil.

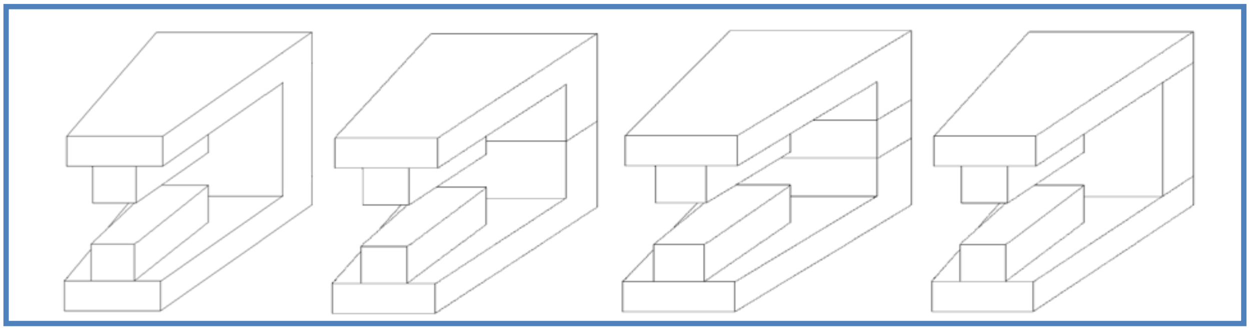

Figure 38 - Stator Segments: Assembly Options (Solid, Two Halves, Two Plates, Hoop)

The shape of the stator teeth is a design issue to be evaluated. The teeth may have sides that are parallel (Figure 39, Left) or with a fixed angular span (Figure 39, Right) between the teeth sides whose planes pass through the center axis. The latter configuration (Figure 39, Right) is the most analogous configuration to a radial gap SR machine, as the entire edge of the rotor and stator teeth align at the same angular position as the teeth move from an unaligned to an aligned orientation. Alternatively with Figure 39, Left, the stator tooth edge engages the rotor edge at the inner radius first and progresses outward over a range of rotation. The difference in this application may or may not be an issue for the electrical system. The shape of the machine voltage waveform (harmonic content) and force versus position is different for the two configurations.

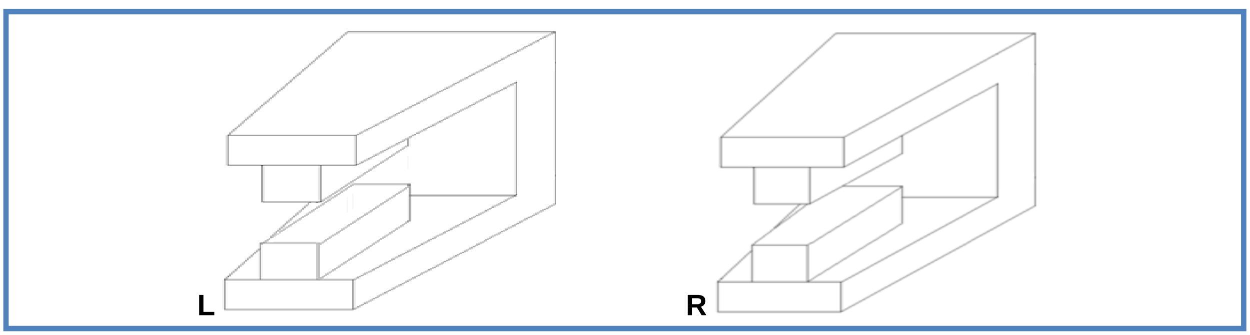

Figure 39 - Stator Tooth Geometry: Parallel (L) and Angular (R)

While the individual stator teeth could be assembled and fastened to the end plates, it is preferable for them to be an integrated structure, which will become apparent when discussing laminations.

A second design consideration is the geometry options for the valley between the teeth. Figure 40, Left shows a constant slot depth (or tooth height), and in Figure 40, Right, a varying slot depth. For optimal SR machine design it is desirable to keep the slot depth equal to the tooth width. In a disk SR machine the varying tooth height can be accomplished by allowing the valley floor to slope down (Figure 40, Right) or allow the gap to be conical. The mechanical issues with a conical gap are not considered due to complexity and cost in fabrication and assembly as compared to a planar gap.

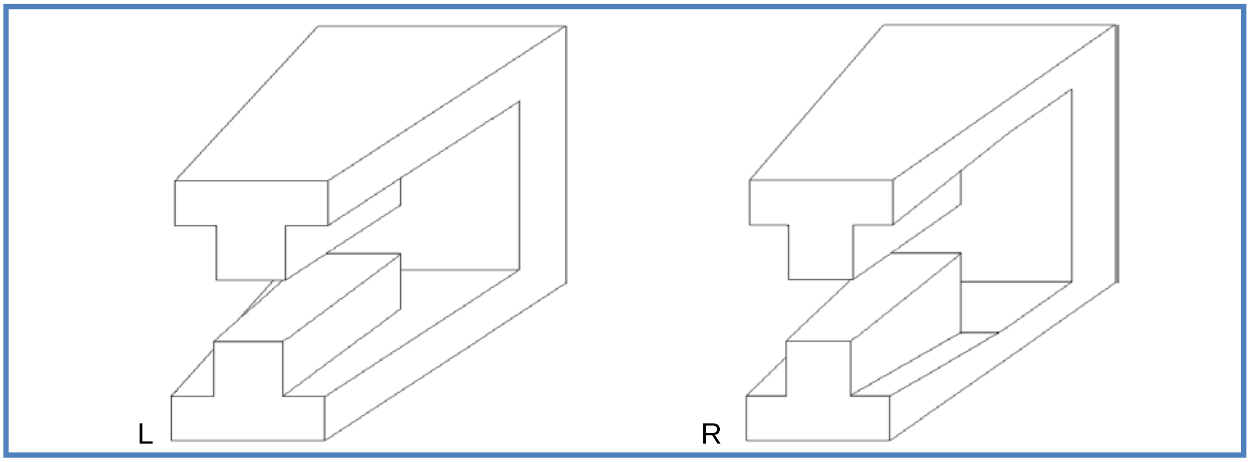

Figure 40 - Stator Tooth and Back Iron Geometry

Tooth Width Varies with Radius Constant Slot Depth (Left) and Constant Tooth Width to Height Ratio (Right)

The illustrations show angular stator segments for illustration purposes. However, these segments are a valid assembly option where a group of these C core segments are assembled circumferentially in a support structure. However, there are geometry constraints for the coil height and the gap between poles. An assembly of C core segments will have a greater challenge controlling gap clearances but can be more readily fabricated from powdered metals and/or laminations, if needed.

The need to break up Eddy currents is a dominant fabrication issue. Figure 41 shows the flux path (ϕ) around a segment of the stator core. Eddy currents (J) are induced in the plane normal to the magnetic flux whenever the flux varies with time ($d\phi/dt$). As discussed in the rotor section, laminated assemblies are the preferred method to minimize Eddy currents to limit core losses and improve dynamic behavior. In addition, the vast majority of ferromagnetic materials come in sheet form as the magnetic properties can be consistently controlled during annealing.

A segmented C core with parallel sides can easily be fabricated from two laminations shapes, one C the valley and one C with the tooth as illustrated in Figure 42, Center. Waste can be minimized by nesting the C shapes when cutting from the laminated strip. In an even simpler form, a single lamination can be used to construct a shape with no valley (Figure 42, Right).

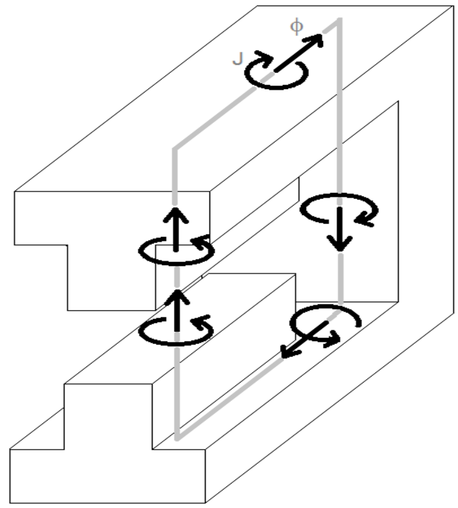

Figure 41 - Stator Tooth and Back Iron Flux and Eddy Current Paths

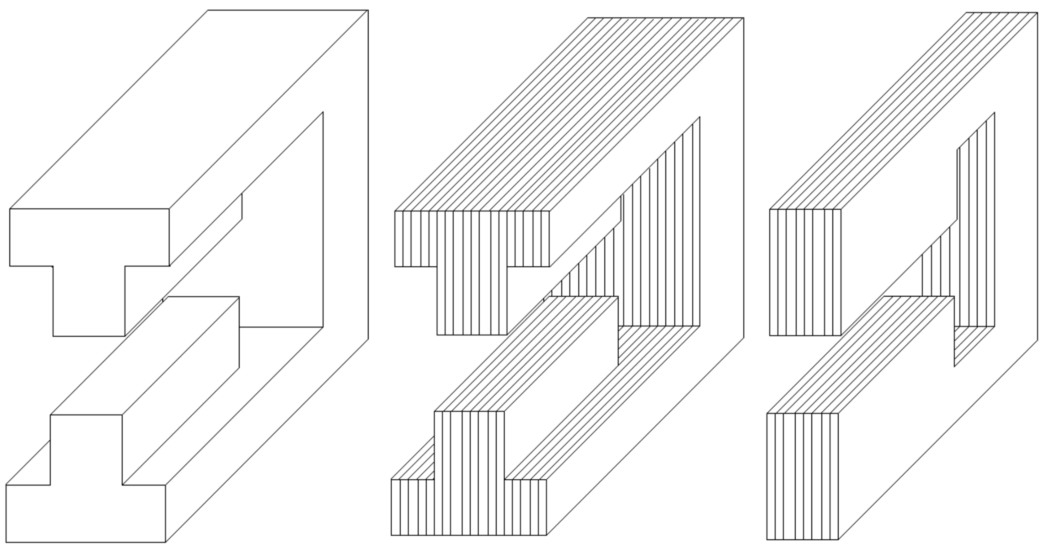

Figure 42 - Stator Tooth and Back Iron Construction

Tapered segments can be constructed from uniform laminations and machined into wedge shapes as illustrated in Figure 43. Tapered lamination material can be used to construct wedges, which are not impossible, but impracticable to obtain as rolling mills will not accept this work on a small volume basis. Angular tolerances are not an issue; laminations cut with reverse taper can be occasionally inserted in the layup to maintain the proper angles. Therefore, the parallel sides are preferred if lamination is required.

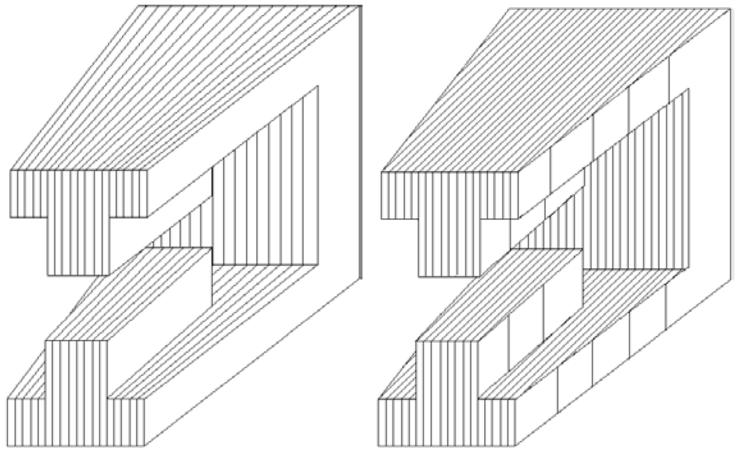

Figure 43 - Stator Tooth & Back Iron Construction: Flat and Wedge Shape Laminations

Alternative construction with a continuous tape wound ring and laminated end plate segments are illustrated in Figure 44 (note that while the illustration is of a segments, the back of the C core is a continuous hoop). The joints between the end plates and tape core are beveled to allow the flux to pass from one lamination orientation to another without Eddy Current losses. Similar techniques are used in transformers. In this case the gap in the SR machine eases the demand of maintaining a tight joint as it will only be a small added reluctance to the total SR magnetic circuit.

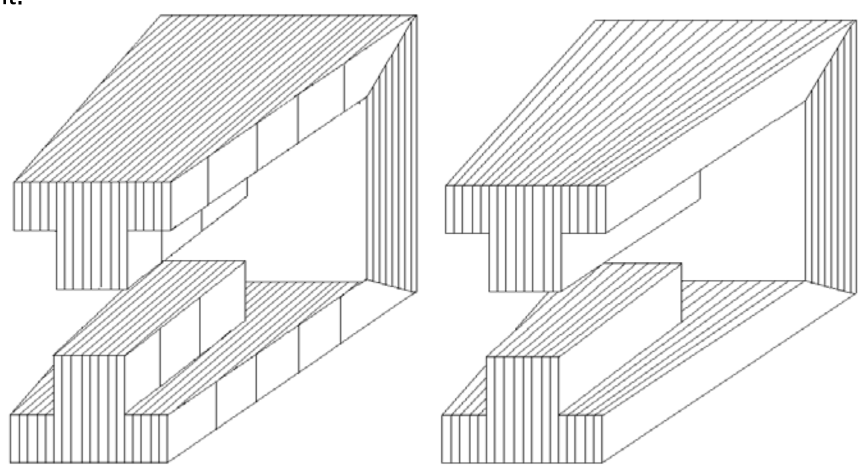

Figure 44 - Stator Tooth & Back Iron Construction: Spiral Wound Back Iron & Laminated End Plates

In conclusion, the geometry in Figure 40 Right is the preferred stator construction. Pre wound coil assembly will require the coil height to be same as the rotor height if the segmented laminations are one piece, if this is not too restrictive on the design trade space and optimization.

For the outside rotor configuration, the only way to assemble C-core segments is to form or wind the coil in place, after stator assembly using either Figure 45 Right or Left.

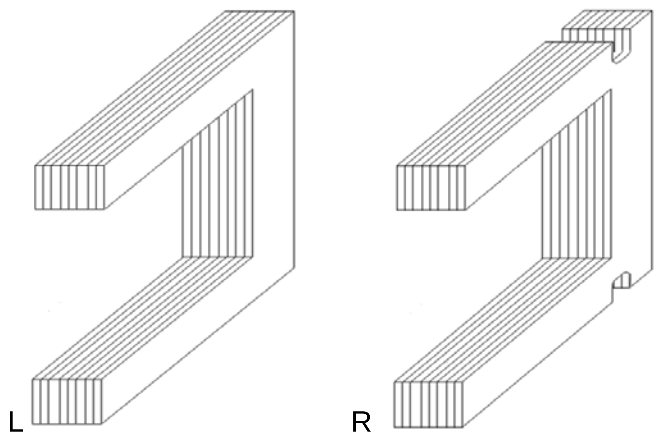

Figure 45 - Stator Tooth C-Core: Air Space for Valley (L), Slots for Mech. Attachment (R)

Given the high cyclic nature of a SRM because of the torque and force variations every time the rotor teeth in a phase align and un-align with its stator, the load bearing parts must be designed with cyclic fatigue in mind. It is paramount that the mechanical structure be designed for stresses below the endurance limit. Figure 46 shows stresses must be designed below 30 ksi for steel; structural materials without endurance limits such as Aluminum should be avoided.

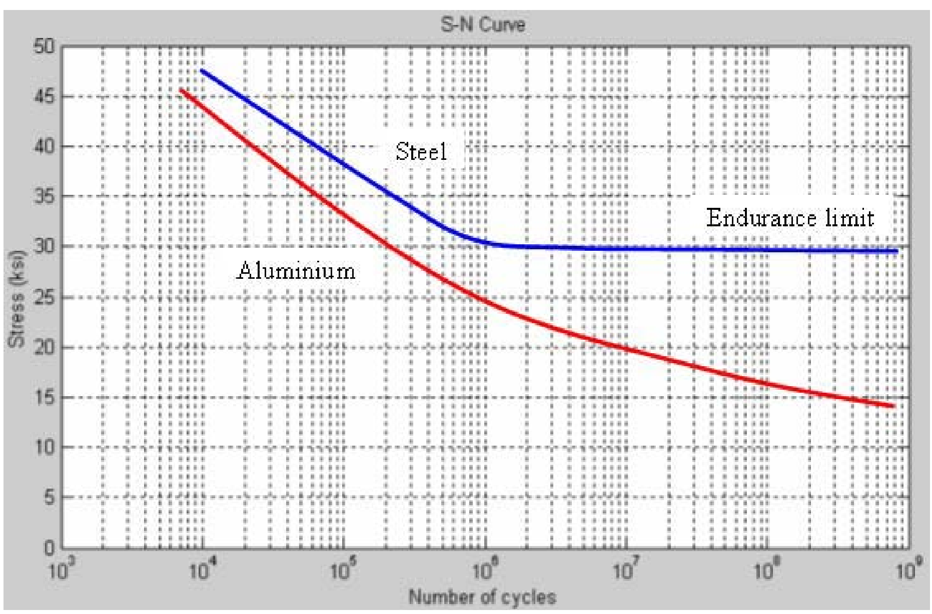

Figure 46 – Stress Endurance Limit vs. Number of Cycles

Rotor and Stator construction, Multi-coil version

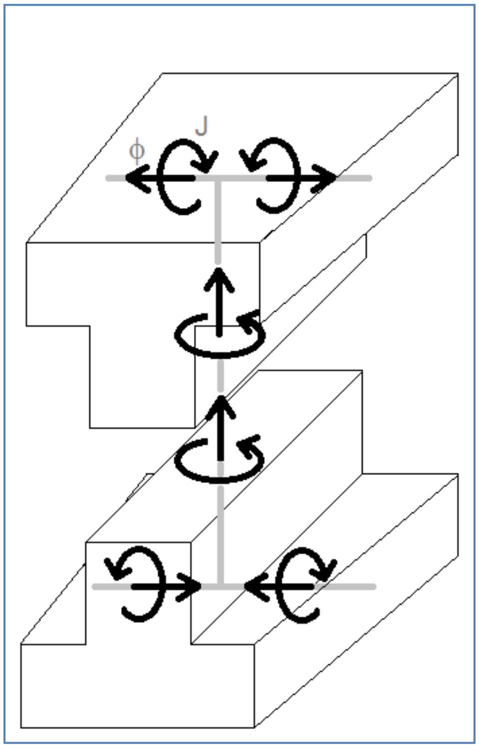

Figure 47 – Lines of Flux (ϕ) and Planes of Induced Eddy Currents (J)

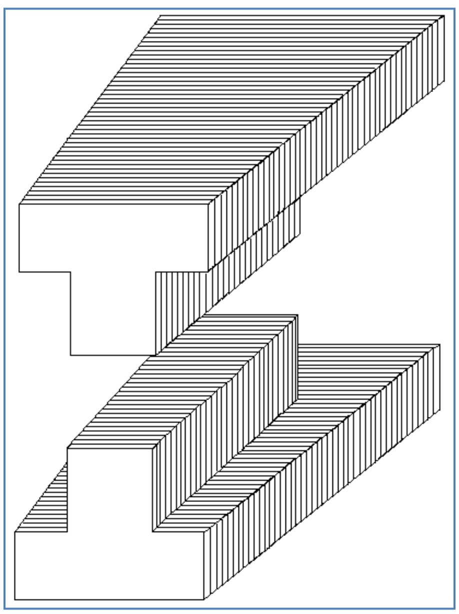

Figure 48 – Preferred Lamination Orientation

Figure 47 shows the flux paths and planes that eddy currents are induced into one tooth segment of the multi-coil version of the axial flux machine. Figure 48 illustrates a laminated segment that will break up the eddy currents in the needed directions.

For a full 360° structure, a fabrication method to achieve the desired lamination orientation is to spiral wrap sheet stock (Figure 49). In low volume production the valleys may be cut out of the laminated roll using wire Electro Discharge Machining (EDM). In larger production, the valleys could be laser or die cut with progressive spacing of the slots such that when rolled, the tabs align to form the teeth. This method is similar to the way automotive alternators are fabricated. The latter method will require additional investment in tooling and manufacturing procedures that may not be warranted in a prototype phase.

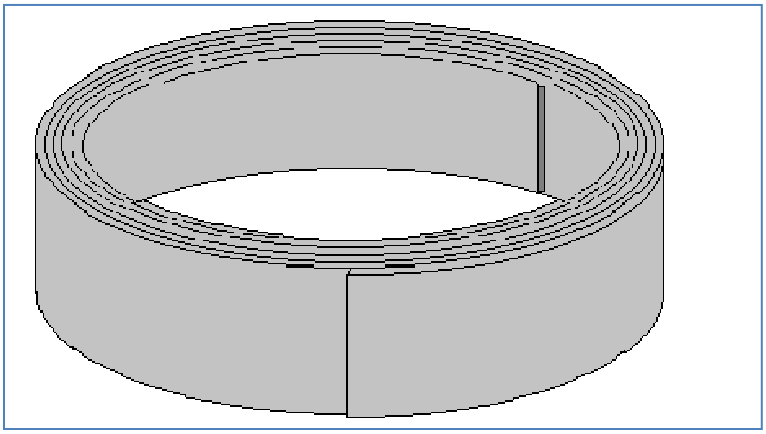

Figure 49 – Lamination Structure

Gap

SRM machines are quite sensitive to gap. Figure 50 shows a comparison in the Torque at 2.5 and 3.5 mm gaps. The peak torque drops by 2 times for a 40% increase gap which is consistent with the inverse gap squared relationship.

Flux linkage (Figure 51) for the models with all the same parameters except for gap differences show a significant drop in max to min ratios versus position.

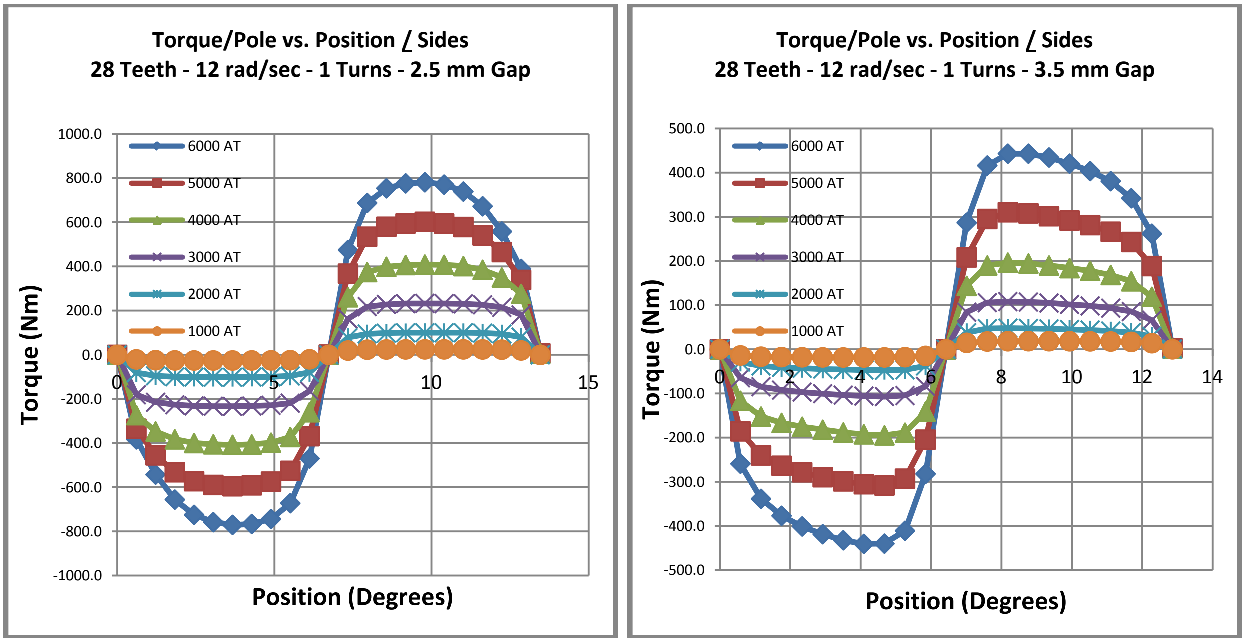

Figure 50 - Torque Sensitivity to Gap

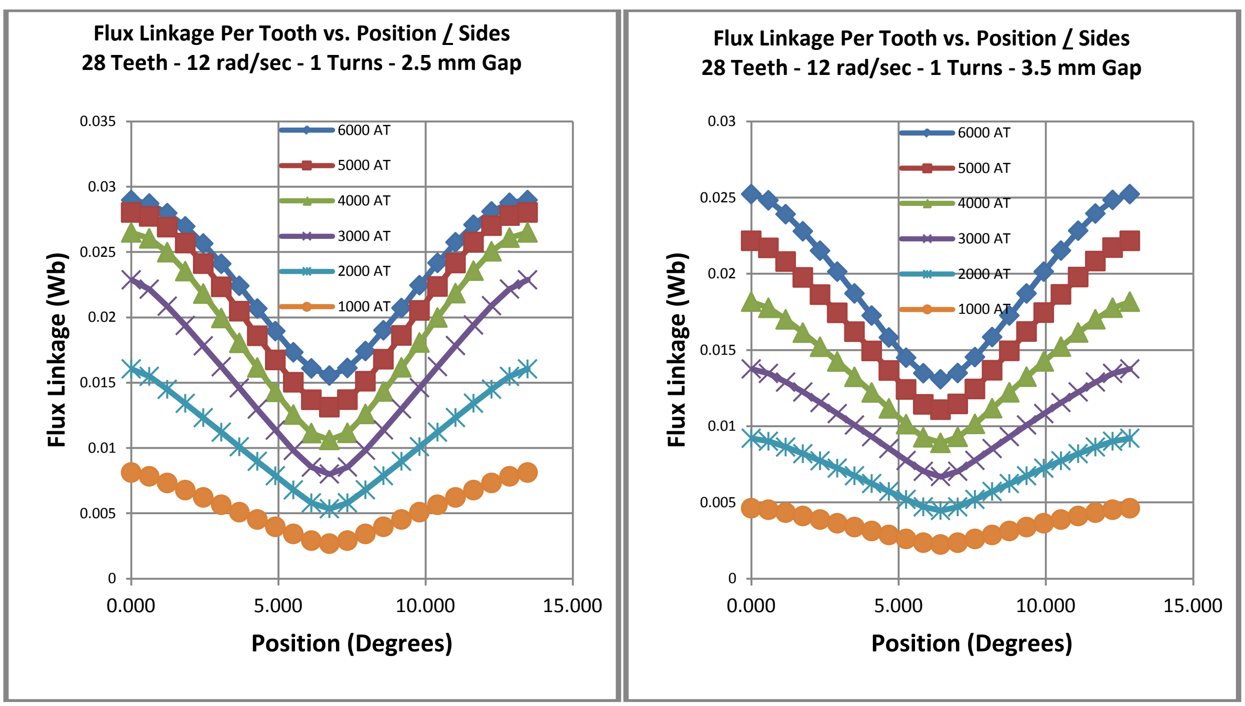

Figure 51 - Flux Linkage Sensitivity to Gap

The maximum variation on flux linkage over one cycle is desired for good electrical energy extraction. The goal of greater than 2 to 1 variation from the aligned to tooth unaligned position is met with the 2.5 mm gap but not with the 3.5 mm gap.

Saturation

Figure 52 shows the effect of saturation in the iron. As the NI increases, the flux linkage (Left plot) increases and a consistent rate but above 3000 AT the incremental increase begins to fall off and at 6000 AT the increase is not worth the cost of the power. The voltage generated across the coil is equal to the derivative of flux linkage (Right plot) and clearly shows the effects of saturation.

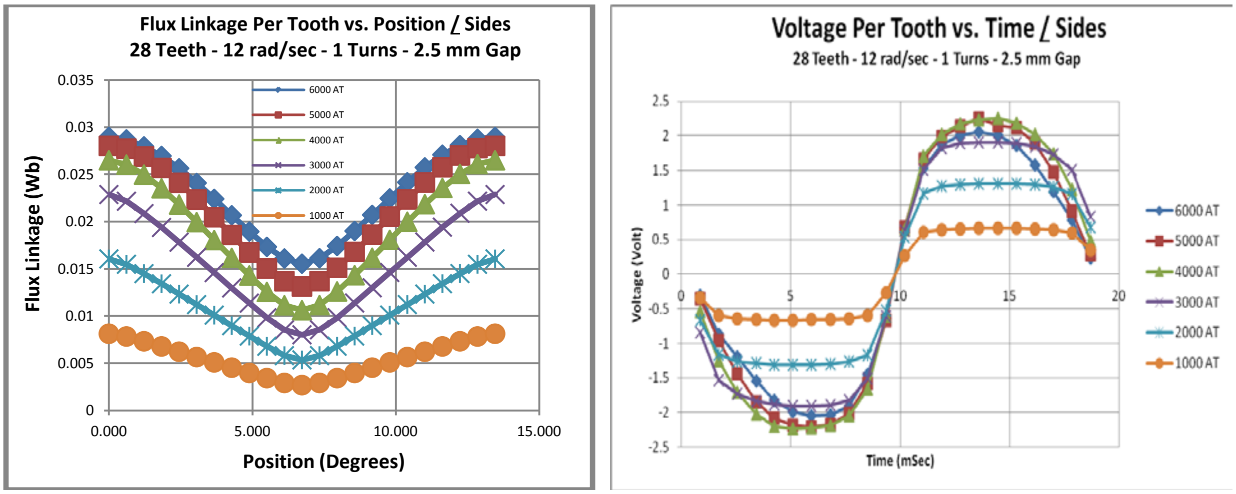

Figure 52 - Saturation Effects on Flux Linkage and dλ/dt

Parallel (//) versus Angular (/)Teeth Sides

The shape of the tooth sides was evaluated using parallel sides and sides that are coincident with rays emanating from the spin axis. The geometry impacts the waveforms of the torque and flux versus position. While teeth with parallel sides are easier to fabricate they cannot provide the desired performance, especially at low tooth count. The torque is lower and the ripple commutating between phases require flatter waveforms spanning 60 electrical degrees (2.5 mechanical degrees for 28 teeth). Comparison of Figure 53 with Figure 29 shows the peaks are about the same up to 4000 AT but saturation causes lower torque levels above that value.

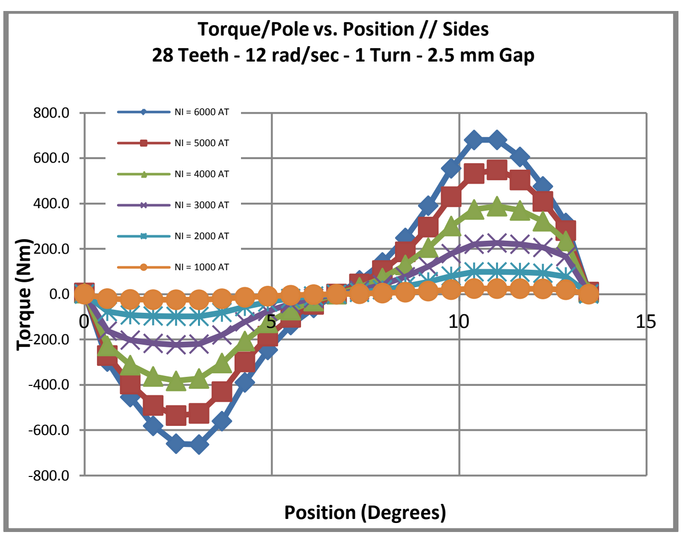

Figure 53 - Parallel Sided Tooth Torque vs. Position for Various NI

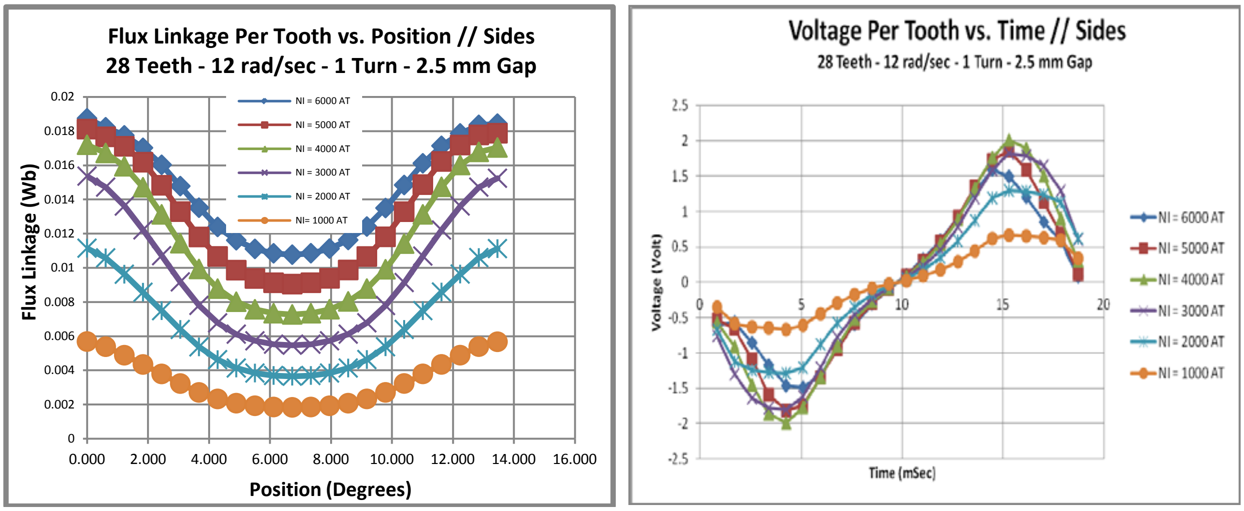

Figure 54 - Parallel Sided Tooth Flux Linkage & Voltage vs. Position for Various NI

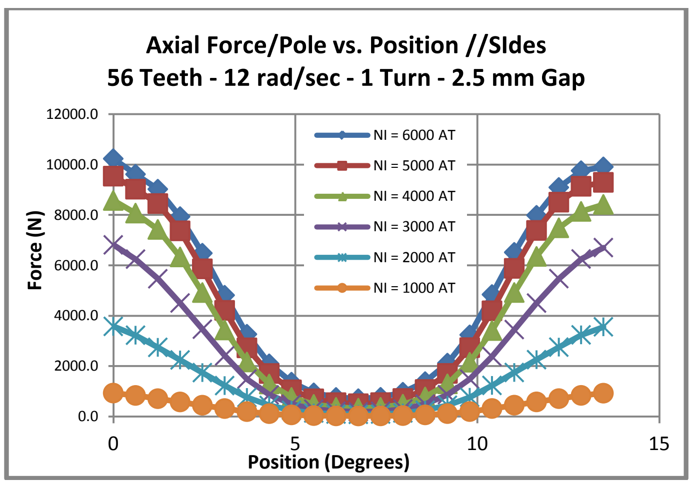

Figure 55 - Parallel Sided Tooth Torque vs. Position for Various NI

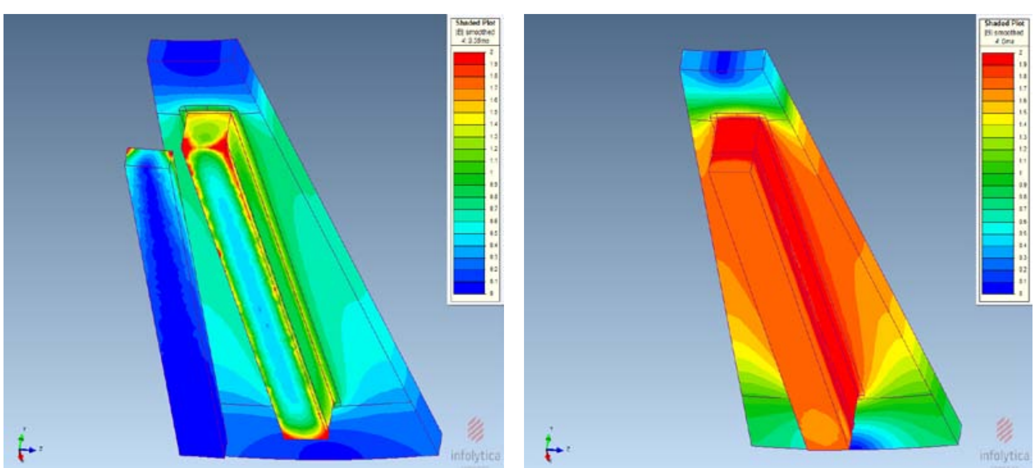

Figure 56 - Unaligned (Left) and Aligned (Right) Flux Density Plots at 4000 AT

Tooth Count

A comparison of the number of teeth was performed and a Torque vs. Position plot at various currents is shown in Figure 57 with the 28 tooth geometry (Left) compared to the 56 tooth geometry (Right). Besides the fewer number of cycles over 1 rev. and the associated larger angular span for the 28 teeth, the torques amplitudes are higher and the peak flat top is wider. The flat top waveform is desirable to minimize ripple when switching between phases.

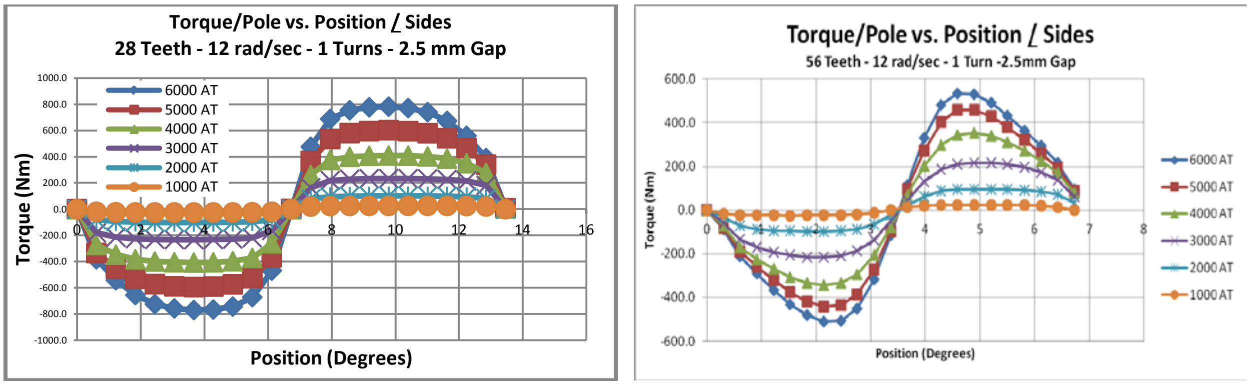

Figure 57 – Effects of the Number of Teeth

Coil Options

Figure 58 shows two coil configurations that can be used in the SRM machine; rectangular poles are used for ease of illustration. The top illustration shows N multi-turn coils around each tooth. The bottom shows N/2 multi-turn coils around every other tooth. Magnetically, a similar result is achieved with both configurations but electrically there is a difference. The mean turn lengths (black lines) for the two configurations are different, so the resistance and I^2R losses are higher by the ratio of these lengths. Coil cross sectional area are roughly equal, with a slightly better packing factor for N/2 coils because there is no need for insulation and clearance between coils as is the case for the N coil configuration. Given the lower cost to fabricate and assemble the N/2 coil option, it may be more desirable for prototyping.

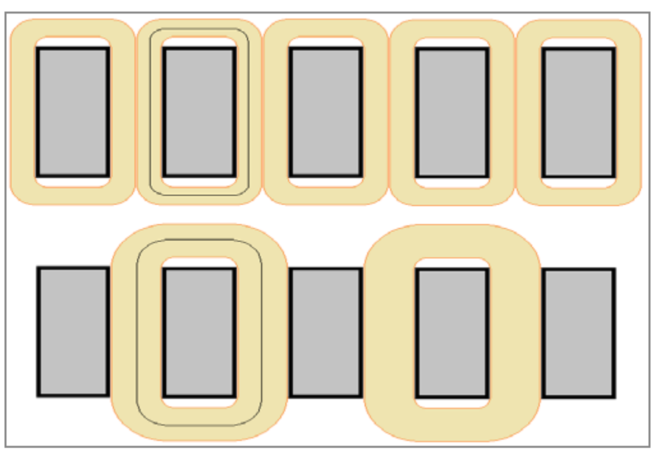

Figure 58 – Coil Options

The rotor lamination fabrication and structure will remain the same as discussed previously, with Figure 37 **b** illustrating the preferred method.

Concept layouts of the 1 coil per phase concepts are contained in Appendix A.

Significant results (Task 3)

Stator and rotor tooth lamination assemblies have been investigated that are consistent with the three Axial Flux machine configurations. These are shown in the figures and as can be seen, rely on some possibly difficult mechanical arrangements such as tapered thickness laminations or butt joints.

Key outcomes (Task 3)

In addition to the undesirable effects of the added back iron of the first two configurations selected, the manufacturing studies indicate the difficulty associated with an economically and magnetically acceptable magnetic path assembly, so further pointing away from these first two configurations. The only benefit ascribable to these two configurations is the convenience and elegance of the single coil winding.

Task 4.0: Electronics Analysis

Specific objectives (Task 4)

The power takeoff electronics developed for the original project have been evaluated for use with the new Axial Flux Reluctance Machine. Voltage, current and power requirements of each of the elements has been considered in the evaluation. Circuit simulation of the system using PSIM has been performed to verify that the expected operation can be achieved.

Major activities (Task 4)

Establishing Specifications and Design Guidelines for the AFSRM Drive Electronics

Specifications for the AFSRM drive are the same as those for the RFSRM drive, and are derived from the specifications of AWEC PTO (Advanced Wave Energy Conversion Power Take Off) system, shown in Figure 59. The PTO needs to provide 100kN linear force for the relative linear input speeds up to 1m/s. Above 1m/s, the linear force rolls off with speed to maintain constant power extraction. The maximum operating velocity is 2m/s. The linear to rotary conversion is provided by a belt/sprocket based mechanical linkage interface, with a conversion ratio of 8rad/s per 1m/s for input to the SRM. The SRM shaft torque specifications therefore are 12.5kNm for rotation speeds up to 8rad/s, and this will roll off to maintain constant power operation for rotation speeds from 8rad/s to 16rad/s.

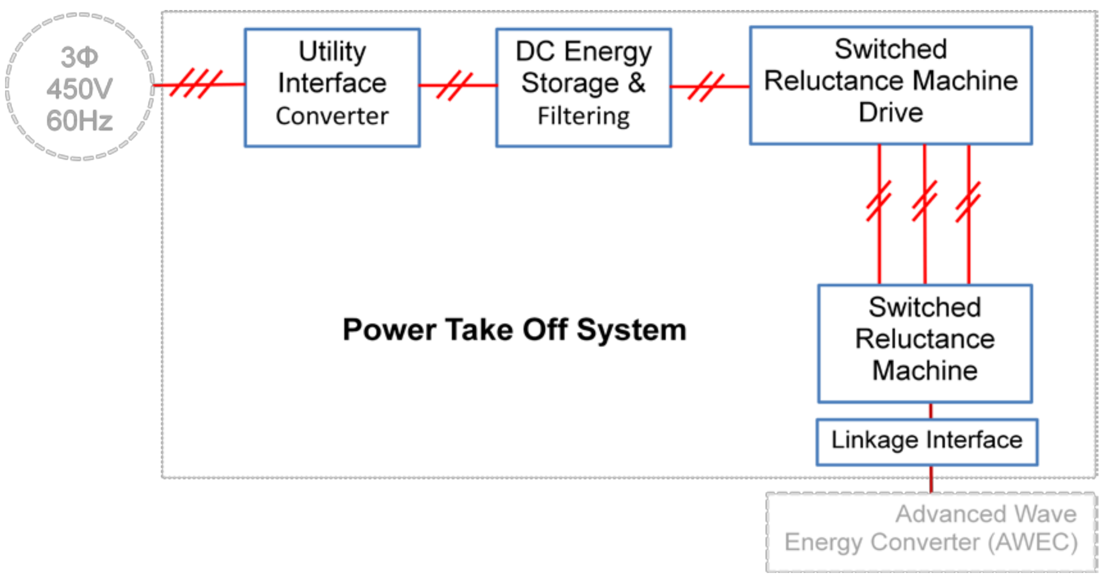

Figure 59 - PTO System Configuration for the AWEC

The SRM drive is the standard drive configuration as shown in Figure 60. Each phase is driven by an H-bridge. Unlike the typical SRM asymmetrical H-bridge consisting of two active switches and two diodes, each of the four switches is implemented with an IGBT with an anti-parallel diode. This choice is to relieve the thermal stress on the power switching devices due to the peculiarities of the wave energy conversion application by permitting use of both sides of the bridge alternately. It is operated from a DC link regulated by a utility interface converter. The DC link voltage is regulated at 1000Vdc nominal. The utility interface converter uses an existing design and is sized to allow a nominal power flow of 150kW, higher than the PTO power requirement. To be consistent with the utility interface converter power capacity and allow growth of the PTO capacity, the SRM drive is specified with a rated capacity of 150kW as well. The SRM drive specifications are derived as follows:

Rated DC Link Voltage: 1000Vdc
Rated Current: 450A
Rated Capacity: 150kW
Efficiency: 95% at Full Power
Cooling: Liquid (EGW 50/50)

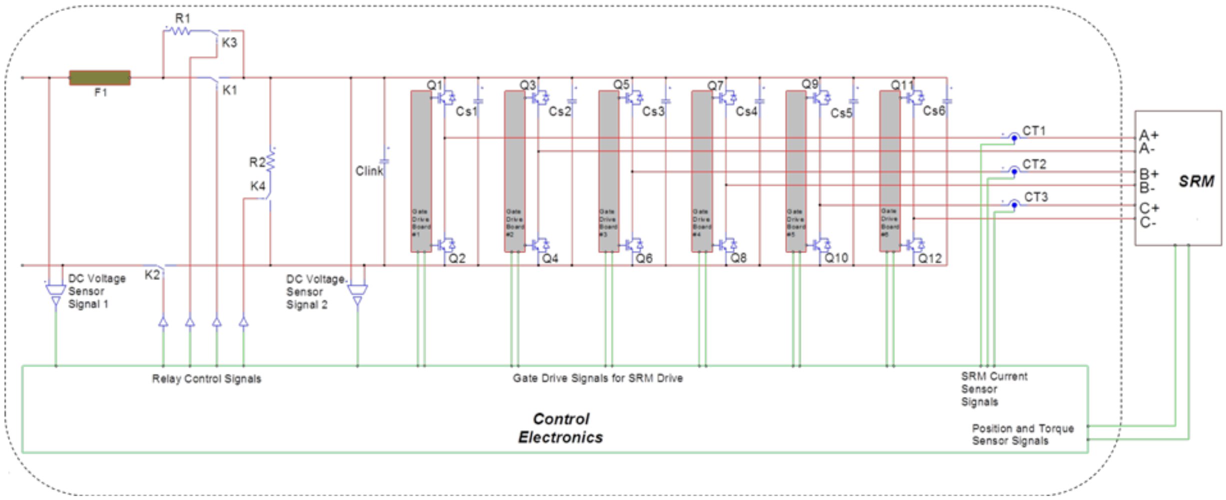

Figure 60 - SRM Drive Configuration

Guidelines for the SRM drive electronics design are similar to those for other machine types. Given the DC link voltage range available to the drive electronics and the Ampere-Turns required for torque generation, the machine winding details are determined so that the drive Volt-Ampere (VA) requirement is minimized. However, due to the highly nonlinear behavior typical of an SRM, closed-form design equations do not readily apply. Instead, Finite-Element Analysis (FEA) of the SRM needs to be performed to produce the data describing the relationship between the flux linkage and the current and rotor position, $\lambda=f(i, \theta)$, and the torque function $T=g(i, \theta)$ as well. These highly nonlinear functions cannot be easily represented in closed form, and usually are used as Look-Up Tables (LUTs) to facilitate simulation study and drive electronics design.

Modeling of AFSRM for Electronics Design and Extraction of AFSRM Model Parameters

The AFSRM model for circuit simulation is shown in Figure 61. This figure represents a phase winding of the AFSRM. Since mutual coupling between different phases is absent, the phase windings are independent of one another, and the complete three-phase AFSRM can be represented by three of such phase winding models. In this model, there are two two-dimensional LUTs, representing $\lambda=f(i, \theta)$, and $T=g(i, \theta)$, respectively. The table data is per-pole based, and scaling factors are used to allow flexible selection of the number of turns per coil and the way these coils are connected, without creating different tables for different stator winding configurations.

As described in other tasks, different AFSRM layouts have been considered, including the inner ring coil, outer ring coil, and multiple coils distributed among the teeth. The comparison based on cost, size/weight and manufacturability indicates that the multiple-coil version is the most practical structure. The electronics design therefore focuses on the multiple-coil AFSRM, which is similar to the RFSRM in circuit model. The noticeable difference lies in the fact that the AFSRM has the two stator sides, with the rotor disk positioned in between. The two-sided stator has 28 teeth on each side, and correspondingly there are 28 teeth on the rotor. Each pole is comprised of two facing stator teeth and one rotor tooth. Each stator tooth is fitted with one coil, and the two coils fitted on the two facing stator teeth (therefore belonging to one magnetic pole) which are always connected in series are considered as a full coil, resulting in the term "half coil" applied to the coil on each stator tooth. The number of turns per half coil as well as the connection of the full coils determines the phase winding VA characteristics and requirements on the drive electronics.

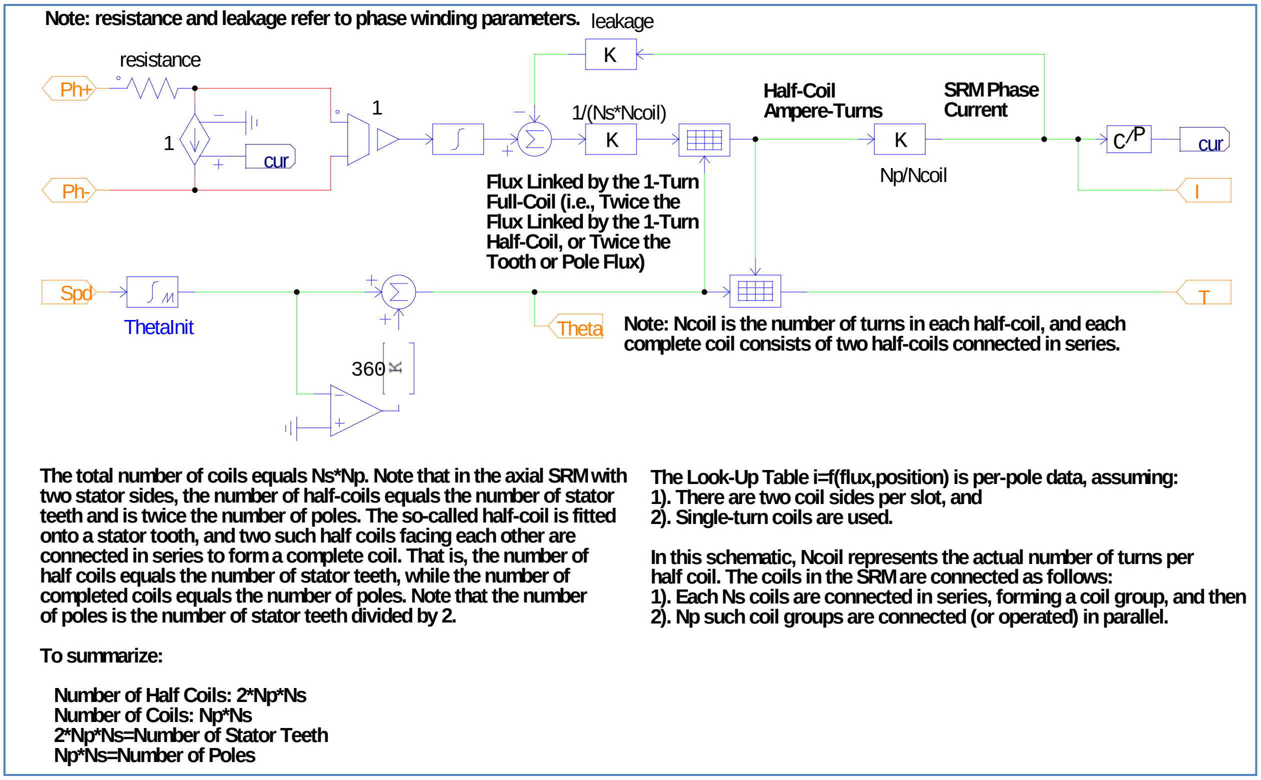

Figure 61 - SRM Phase Winding Model Used for Circuit Simulation

Post-processing of the FEA data of the AFSRM is performed to generate the two LUTs shown in Figure 61. The FEA data are exported into an Excel spreadsheet, and Mathcad (Version 15.0) is used for data post-processing. Figure 62 presents the total torque as a function of the phase current and rotor position for a single-phase of the AFSRM. Figure 63 through Figure 66 present the phase winding flux linkage, back EMF, incremental inductance, and apparent inductance as functions of the phase current and rotor position, with the number of turns per half coil chosen to be 175, and all the coils connected in parallel. The Mathcad script provides a fast and convenient approach to initial choice of the appropriate number of turns per half coil, given the DC link voltage and coil connection method, parallel in this application for balanced magnetic excitation to all the poles. The circuit simulation tool PSIM (Version 9.3) is used to conduct more detailed study to evaluate the performance of the AFSRM and drive electronics, and to determine the requirements on the power semiconductor switches and passive components.

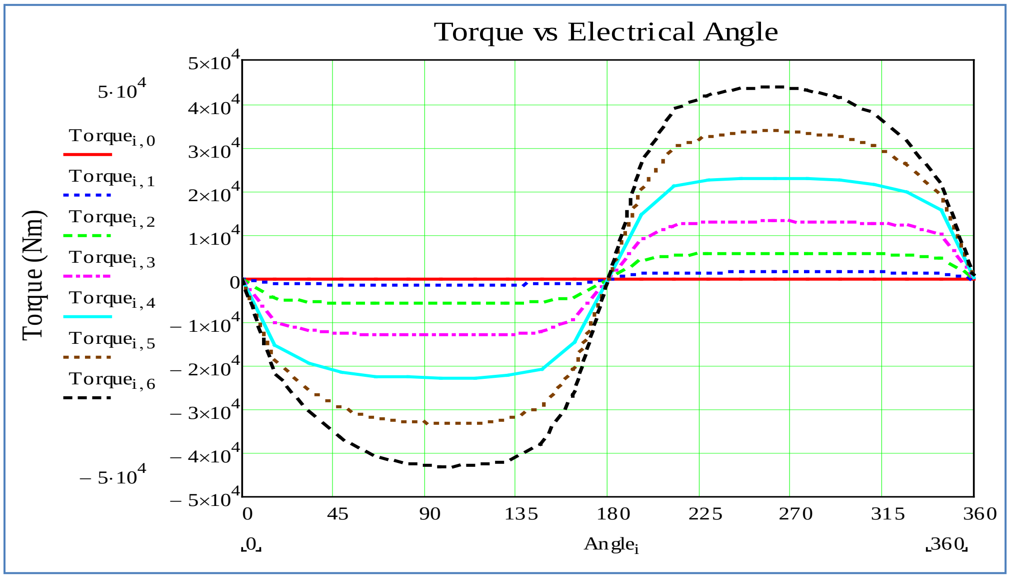

Figure 62 - Torque as a Function of Current and Rotor Position

Current from 0 to 6000AT per Half Coil, in Steps of 1000AT
Rotor Position in Electrical Degrees

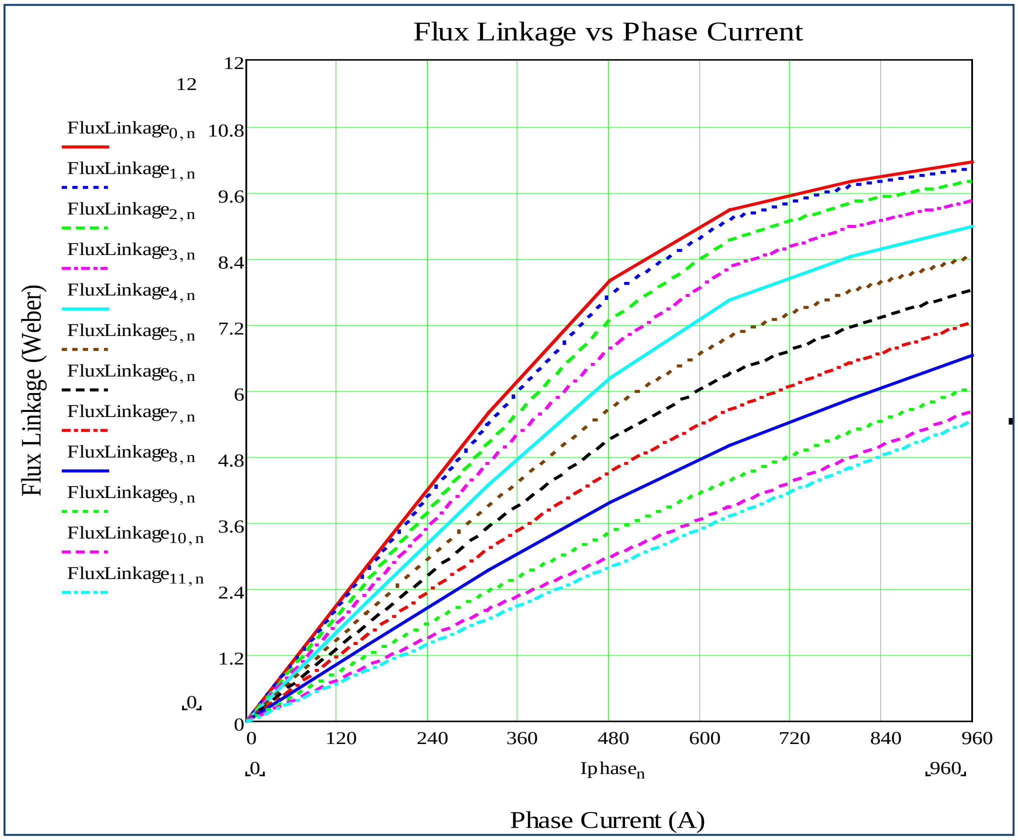

Figure 63 - Flux Linkage as a Function of Rotor Position and Phase Current

Rotor Position from Fully Aligned to Unaligned, in Equal Steps

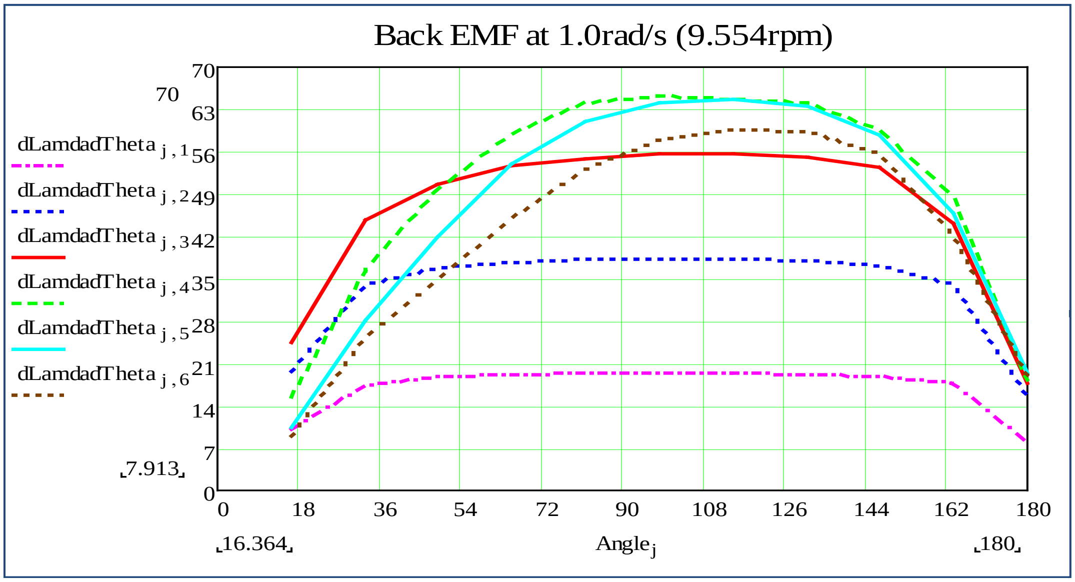

Figure 64 - Back EMF as a Function of Current and Rotor Position

Current from 1000AT to 6000AT per Half Coil, in Step of 1000AT and Rotor Position in Electrical Degrees, at a Mechanical Speed of 1.0rad/s

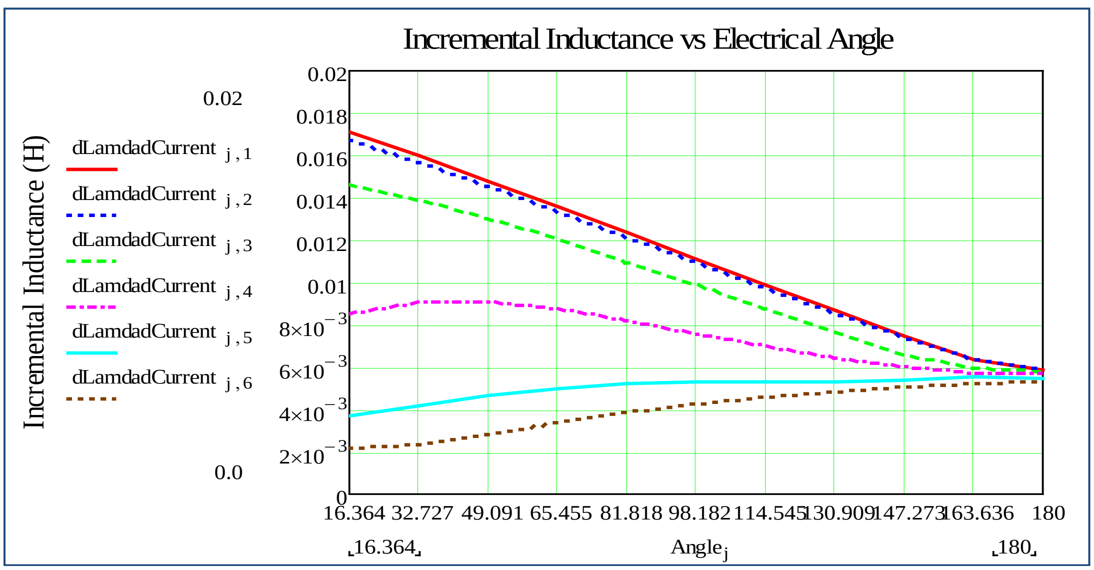

Figure 65 - Incremental Inductance as a Function of Current and Rotor Position

Current from 1000AT to 6000AT per Half Coil, in Step of 1000AT and Rotor Position in Electrical Degrees

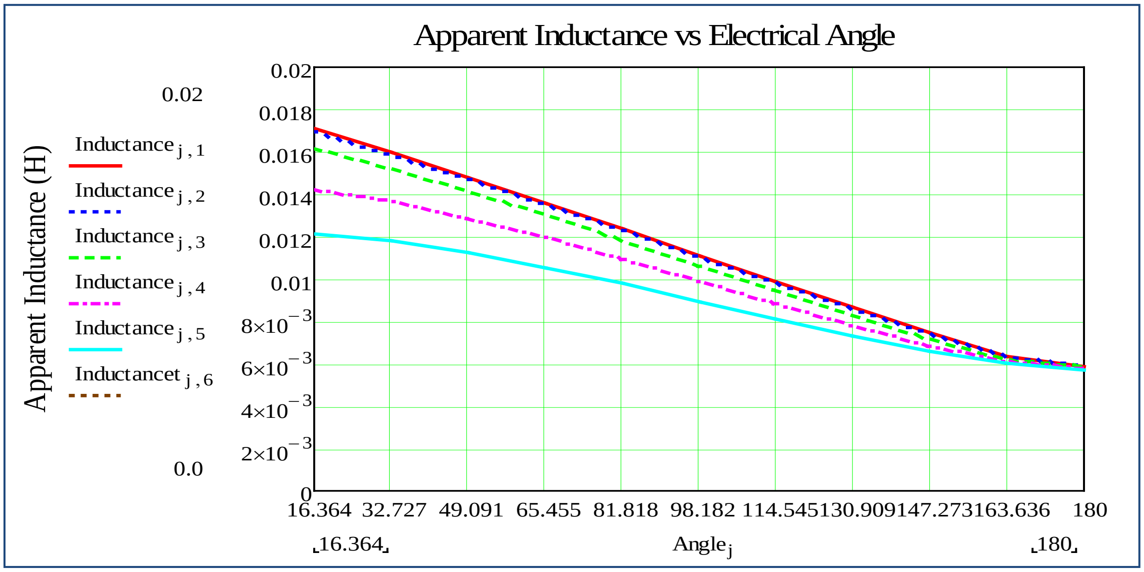

Figure 66 - Apparent Inductance as a Function of Current and Rotor Position

Current from 1000AT to 6000AT per Half Coil, in Step of 1000AT and
Rotor Position in Electrical Degrees

Some comments can be made on AFSRM behavior based on these graphs. First, the torque profile is quite square (and much better than the radial machine shape) up to and well beyond the rated torque of 12.5kNm. The squareness of the torque profile is beneficial to smooth torque production. In the meantime, it is also an indication that the AFSRM is far from deep saturation at the nominal operating point, and there is room for further reduction of iron if optimization of the AFSRM design is to be performed. Second, the incremental inductance, which is the deciding parameter on the phase current buildup, is not too different from the apparent inductance in the perceived operating range. This again indicates that the AFSRM is far from deep saturation. The current buildup for the generator operation therefore can be slow and demands significant advance angle. Compared with the RFSRM where the iron saturation occurs earlier, it is expected that the present AFSRM design would be able to produce smoother torque but be more demanding on the drive electronics.

Simulation Study of the Performance of the AFSRM and Its Drive Electronics

With the AFSRM modeled and parameterized based on the FEA data, circuit simulation with high fidelity was performed to study the performance of the machine and drive electronics. Simulated cases cover the representative operating points. The important circuit variables are tabulated for the sizing of the semiconductor switches and the passive components. Most important are the RMS and peak values of the phase current, the RMS current of the DC link capacitor, and charge variation experienced by the DC link capacitor. Unique to the AWEC application are the low speed high torque operation and significant energy circulation between the SRM and the DC link, necessitating high reliance on the DC link capacitance and buffering inductance for sufficient blocking of the low frequency ripple power flow into the utility interface converter.

Figure 67 presents the simulated waveforms at the rated operating point. Table 5 tabulates the values of the important operating variables at the selected operating points.

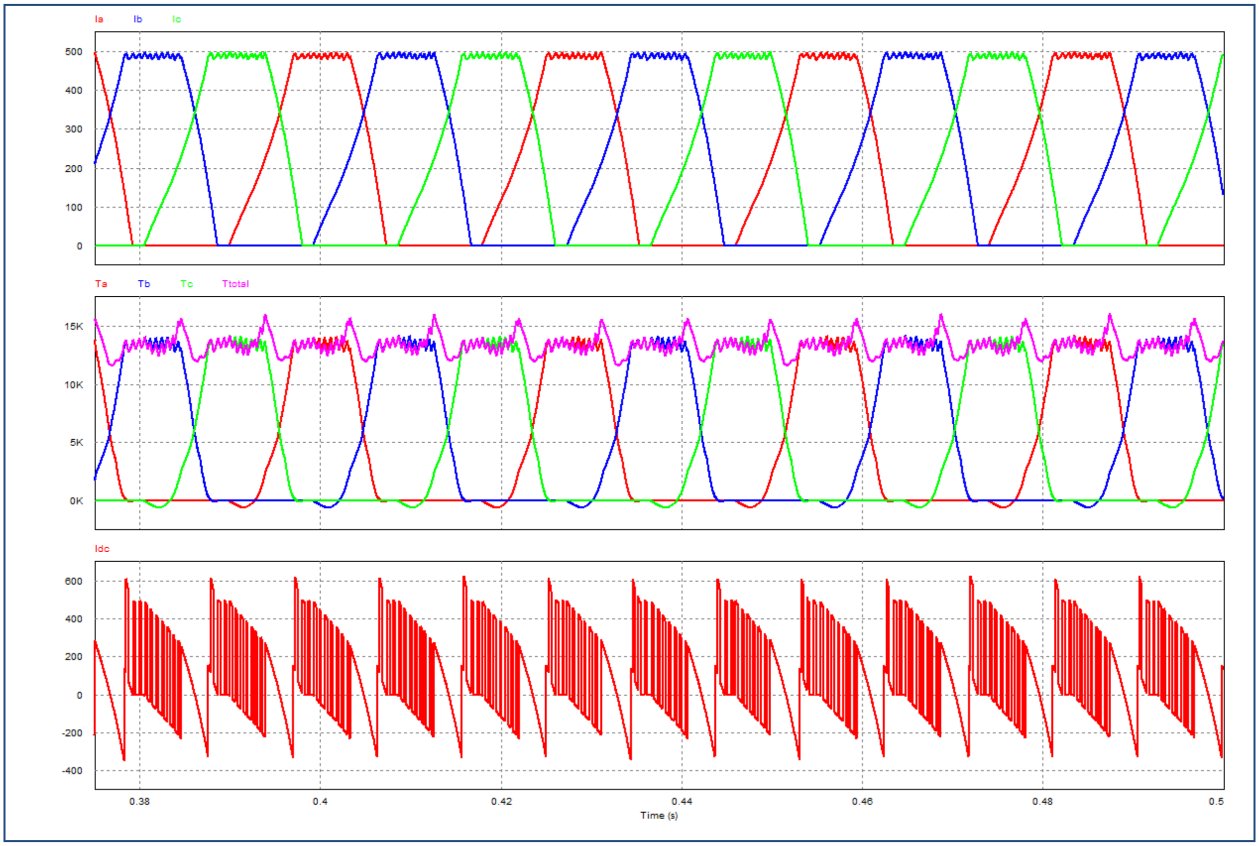

Figure 67 - Simulated Waveforms at the Rated Operating Point (1m/s)

From Top to Bottom: Phase Currents of the Three Single-Phase AFSRMs; Torque Components Produced by Each of the Three Single-Phase AFSRMs and the Total Torque (Pink Trace); and DC Link Current

Table 5 - Summary of Operating Variables for Drive Electronics Sizing

Case #	1	2	3	4
AWEC Relative Velocity (m/s)	0.5	1.0	1.5	2.0
AFSRM Rotation Speed (rpm)	38.2	76.4	114.6	152.8
AFSRM Electrical Frequency (Hz)	17.8	35.7	53.5	71.3
AFSRM Phase Current (A_{RMS})	287	289	304	308
AFSRM Phase Current (A_{Peak})	500	500	500	500
DC Link Capacitor Current (A_{RMS})	197	240	235	237
DC Link Capacitor Charge Variation ($C_{Peak\text{-}to\text{-}Peak}$)	0.70	0.45	0.36	0.48
Average Torque (kNm)	13.45	13.35	13.22	12.07

Component selection for the AFSRM drive electronics is based on Table 5. An important objective of the study is to verify whether the drive electronics designed for the RFSRM can also be used to drive the AFSRM. Table 6 provides a list of the major components of the RFSRM drive.

Table 6 - List of the Major Components of the RFSRM Drive

Component	Description	Quantity
FF450R17ME4	IGBT, EconoDUAL™3, 1700V, 450A	6
2SP0115T2A0-FF450R17ME4	IGBT Driver, Dual Channel, Plug-and-Play	6
EV250-2B	Contactor, 1800VDC, 400A	2
G81A335	Contactor, NO, 10kV, 5A, PCB Mounted	1
G81B335	Contactor, NC, 10kV, 5A, PCB Mounted	1
UP9-19780K, REV E	Capacitor, Film, 1200VDC, 6500µF	3
PT8-19251K	Capacitor, Film, 1200VDC, 0.47µF	6
LPS0600H4700JB	Resistor, 600W, 470Ω	2
CLN-500	Current Sensor, 500A	4
D72SG120V250QF	Fuse, 1200VDC, 250A	1

Comparing the ratings of the components listed in Table 6 and the AFSRM drive electronics requirements embodied in Table 5, it is apparent the only component that appears marginal is the IGBT module FF450R17ME4. This IGBT module has a continuous DC current rating of 450A, which was the highest rating available for the Infineon's EconoDUAL™3 package at the time the RFSRM drive electronics was designed. At present, Infineon offers 600A IGBT module in the EconoDUAL™3 package. The 600A EconoDUAL™3 IGBT module, FF600R17ME4, can be a direct replacement of the FF450R17ME4 without any modification to the mechanical layout, and is sufficient for the AFSRM drive electronics. Table 7 provides a list of the major components of the AFSRM drive, and Figure 68 presents the drive electronics layout, which is the same for both the RFSRM and AFSRM drives.

Table 7 - List of the Major Components of the AFSRM Drive

Component	Description	Quantity
FF600R17ME4	IGBT, EconoDUAL™3, 1700V, 600A	6
2SP0115T2A0-FF600R17ME4	IGBT Driver, Dual Channel, Plug-and-Play	6
EV250-2B	Contactor, 1800VDC, 400A	2
G81A335	Contactor, NO, 10kV, 5A, PCB Mounted	1
G81B335	Contactor, NC, 10kV, 5A, PCB Mounted	1
UP9-19780K, REV E	Capacitor, Film, 1200VDC, 6500µF	3
PT8-19251K	Capacitor, Film, 1200VDC, 0.47µF	6
LPS0600H4700JB	Resistor, 600W, 470Ω	2
CLN-500	Current Sensor, 500A	4
D72SG120V250QF	Fuse, 1200VDC, 250A	1

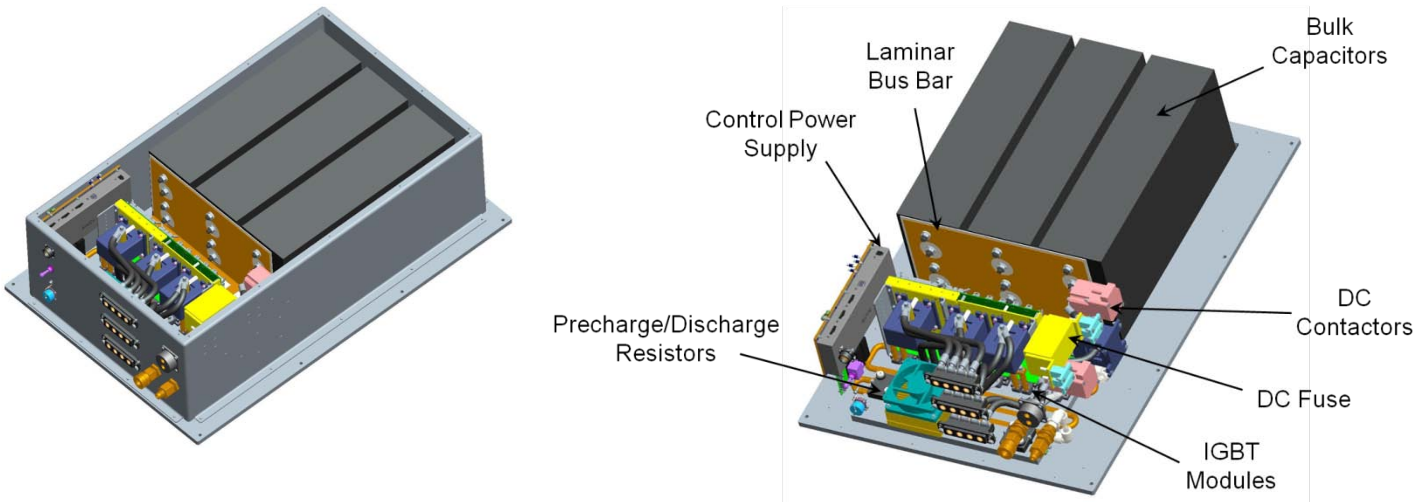

Figure 68 - Drive Electronics Layout, Applicable to both the AFSRM and RFSRM

Comparison between the RFSRM-Based AWEC and the AFSRM-Based AWEC PTOs
Comparing the drive electronics for the AFSRM and RFSRM, it is apparent that the impact on the existing RFSRM drive electronics is minor. The only change necessary is the IGBT module and its plug-and-play gate driver. This change does not result in any mechanical layout change, since the IGBT modules in both drive electronics use the same package and same footprint. As a matter of fact, if the RFSRM is to be used in the AWEC application, it is beneficial to use the 600A IGBT module as well. The 600A module was not available when the RFSRM drive electronics was designed. Now that higher current rating is achievable in the same device package without any modification to the mechanical layout, the RFSRM can be wound with a reduced number of turns in exchange for wider operating speed range. The final choice would depend on the AWEC system level evaluation and the installation site specifics.

It is worthwhile to study the torque and power producing capability of the SRM and drive electronics combination. Since the focus is on the generating capability, the power limit (150kW) imposed by the utility interface converter is ignored in this evaluation. Figure 69 presents the maximum torque versus the relative speed up to 3m/s, and Figure 70 shows the corresponding maximum shaft power versus the relative speed. It is apparent the RFSRM's maximum torque and power boundaries can be expanded noticeably if the 450A IGBT modules are replaced with the 600A IGBT modules. In the meantime, the AFSRM and RFSRM behave quite closely if 600A and 450A IGBT modules are used in the AFSRM and RFSRM drive electronics, respectively.

It is also noticed that the copper loss in the AFSRM is much higher than that in the RFSRM. This is due to the poor utilization of the slot area as well as the limited slot depth. The weight of the copper in the present AFSRM design is only 1/3 that of in the RFSRM. An optimization design procedure might be necessary to arrive at a better design with reduced copper loss at the cost of more copper, and, as pointed out earlier, there appears to be room for improvement of the iron usage to reduce iron volume and weight.

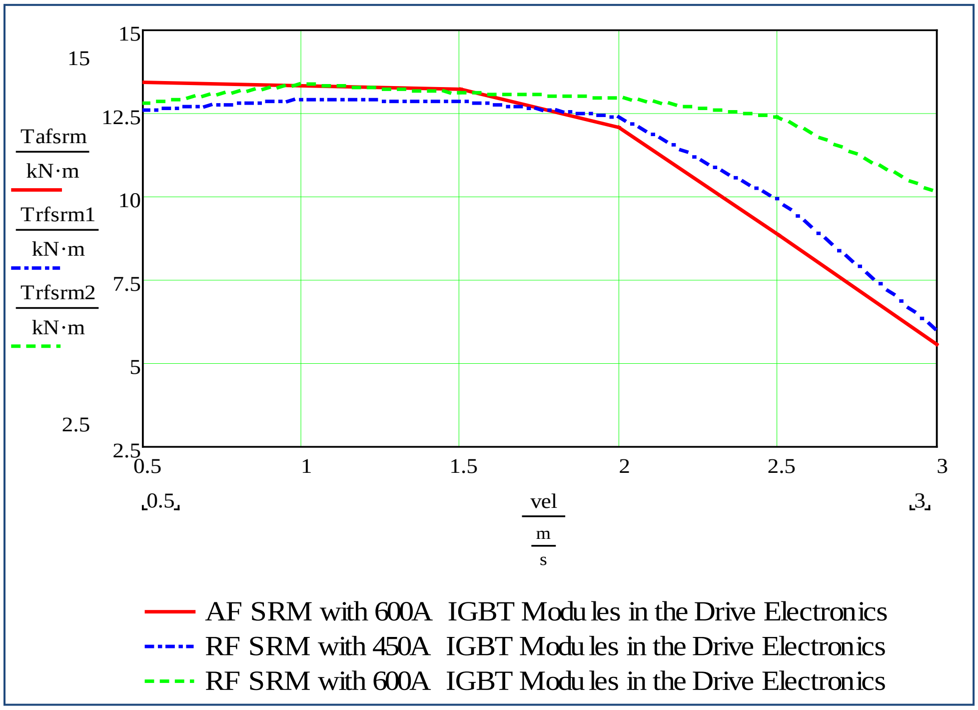

Figure 69 - Maximum Torque as a Function of the Relative Speed

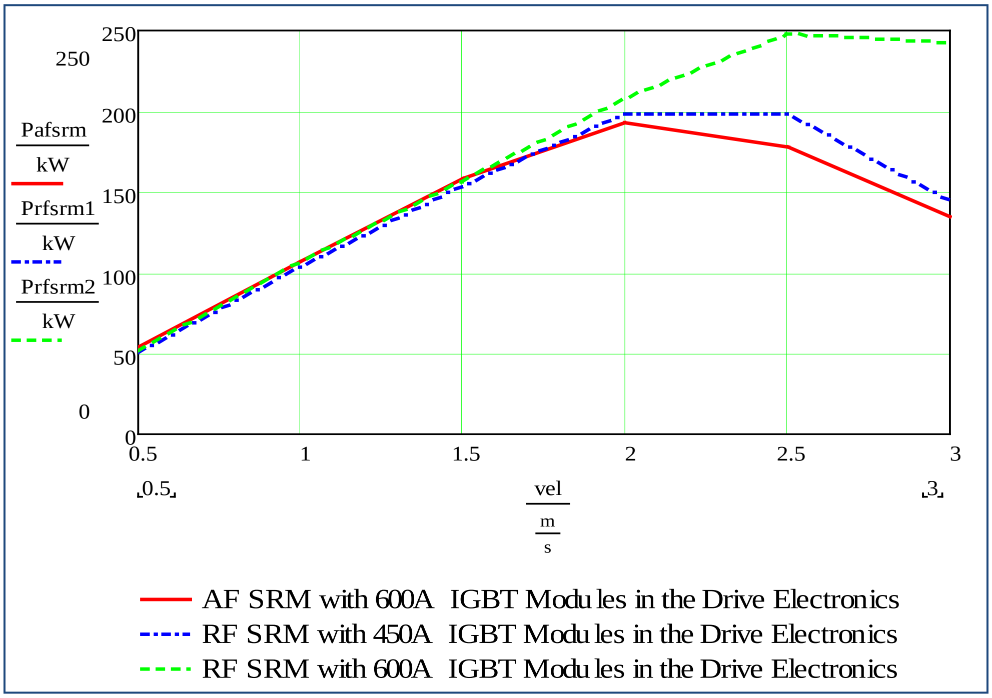

Figure 70 - Maximum Shaft Power as a Function of the Relative Speed

Significant results (Task 4)

The drive electronics design for the AFSRM has been performed. The specifications and design guidelines has been established for the AFSRM drive electronics. LUT-based circuit model has been created from the AFSRM FEA data to facilitate the simulation study of the performance of the AFSRM and its drive electronics. Values of the important circuit variables were extracted from the simulation results and used in drive electronics component selection. A list of major parts and the mechanical layout of the drive electronics has been presented. A comprehensive comparison was made between the AFSRM based and RFSRM based AWEC PTOs.

Key outcomes (Task 4)

The existing RFSRM drive electronics can be used to drive the AFSRM with a simple replacement of the IGBT modules and the corresponding plug-and-play gate drivers. The replacement of the IGBT modules does not incur any mechanical layout modification, since the IGBT modules in both drive electronics use the same package and same footprint. The AFSRM drive electronics design, which offers higher current capability, can be used to drive the RFSRM as well, allowing a reduction of the number of turns per coil and resulting in noticeable enhancement to the operating range.

Task 5.0: System Comparison

Specific objectives (Task 5)

The results of tasks 1-4 were used to perform a direct comparison between the two machine designs (radial flux switched reluctance machine of the original project, and the axial flux reluctance machine of this project). A table comparing size, weight, and volume has been created summarizing the results.

Major activities (Task 5)

A third axial gap SRM configuration consisting of multiple coils per phase was analyzed. Figure 71 illustrates the second SRM FEA model geometry of 1 coil per tooth. In this configuration, the stator tooth has a coil wrapped around its circumference. The total number of coils is 2*NT for the model and odd periodic boundary conditions is imposed in the FEA model to facilitate analysis. Variations on this geometry also included parallel vs. angular sided teeth. There are alternate coil configurations that have NT and NT/2 coils that also are feasible.

Significant results (Task 5)

Results from the model illustrated in Figure 71 can be scaled for the other configurations. Results can also be scaled for all manner of parallel, series and parallel/series combinations of coils, as well as the coil on every other tooth and/or a coil on every other tooth on only one side or alternating teeth on alternating sides. Configurations with coils on every other tooth wound to fill the slot are of interest as half the number of coils need be built and assembled. It is also beneficial thermally if the coils on every other tooth alternate position on the opposing side of the tooth. Although a coil on every tooth is likely to have the best thermal performance.

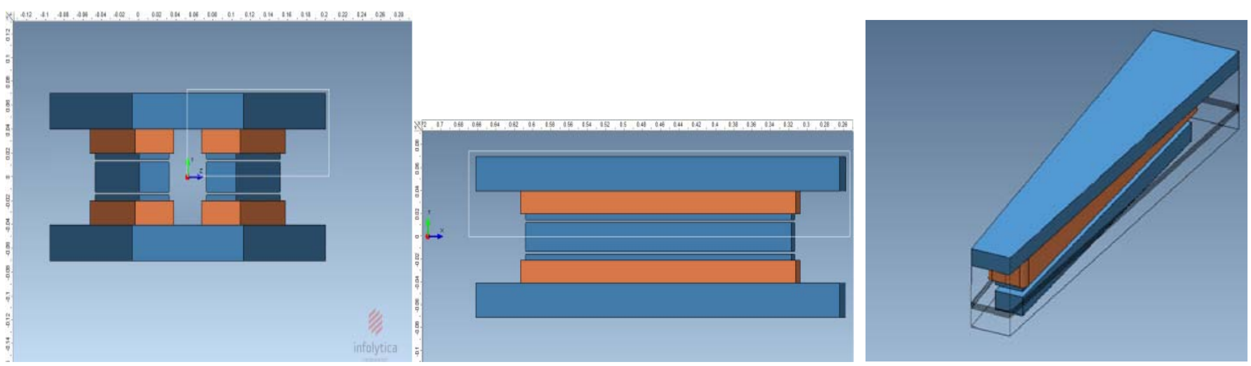

Figure 71 – Multi Coil Axial Gap SRM FEA Model

The flux density plot (Figure 72) illustrates how the magnetic flux now travels axially through teeth and then splits traveling circumferentially through two parallel paths in the disk of iron (Top wedge in the FEA model) that supports the stator tooth. No flux path is needed at the ID or OD as was the case with the single coil configuration. The coil on each tooth structure has a lower mass of material that the single coil configuration. The lower weight comes at the cost of an associated increase in complexity of multi coil connections and added manufacturing & assembly cost. This configuration is most similar to the baseline radial gap SRM.

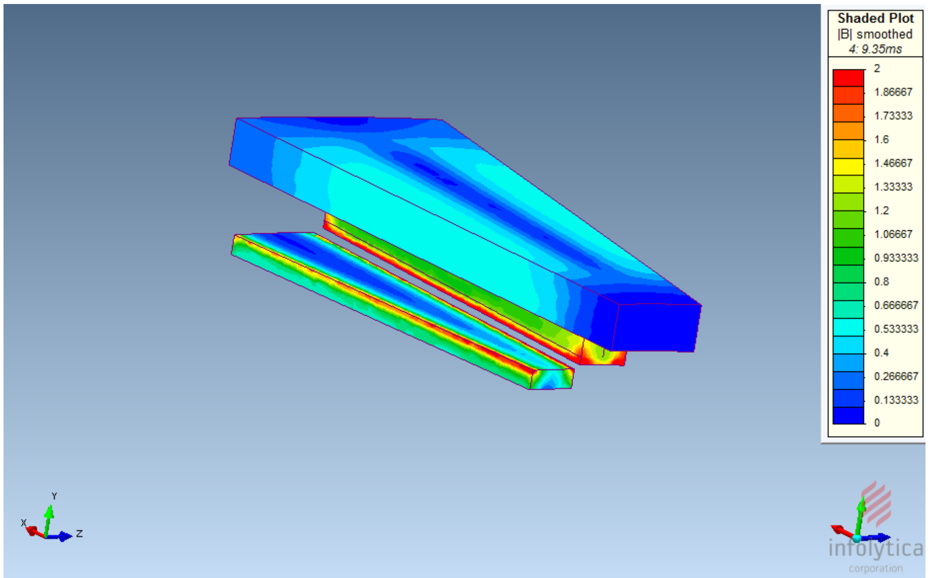

Figure 72 – Multi Coil Axial Gap SRM FEA Result - |B| Flux Density Plot

Figure 73, Figure 74 and Figure 75 plot the torque, flux linkage and axial force for a 28 tooth case with a 2.5 mm gap.

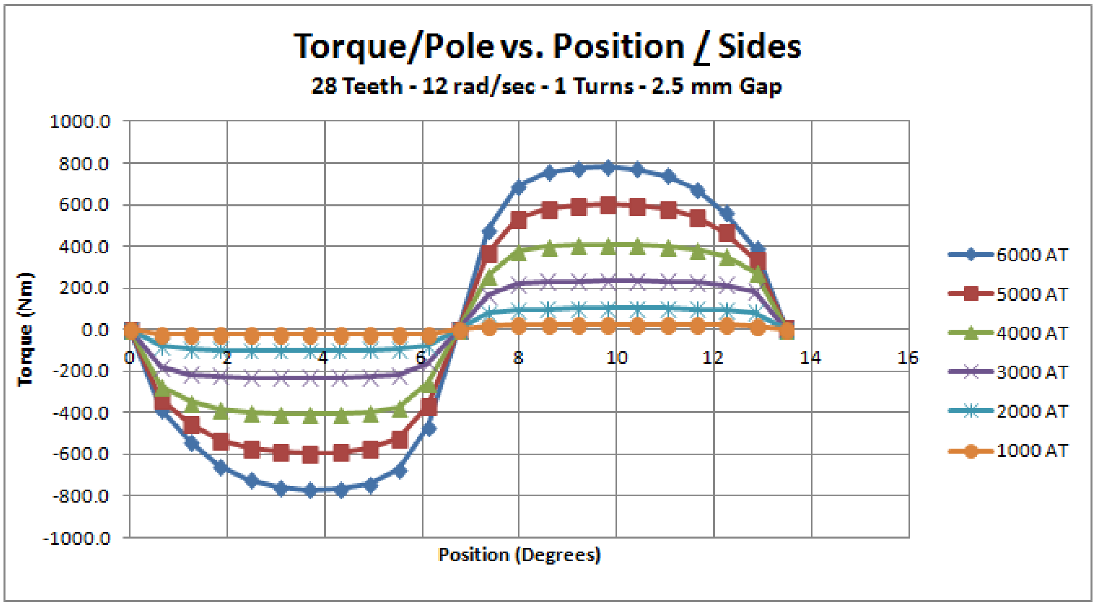

Figure 73 – Multi Coil Axial Gap SRM FEA Result - Torque versus Position

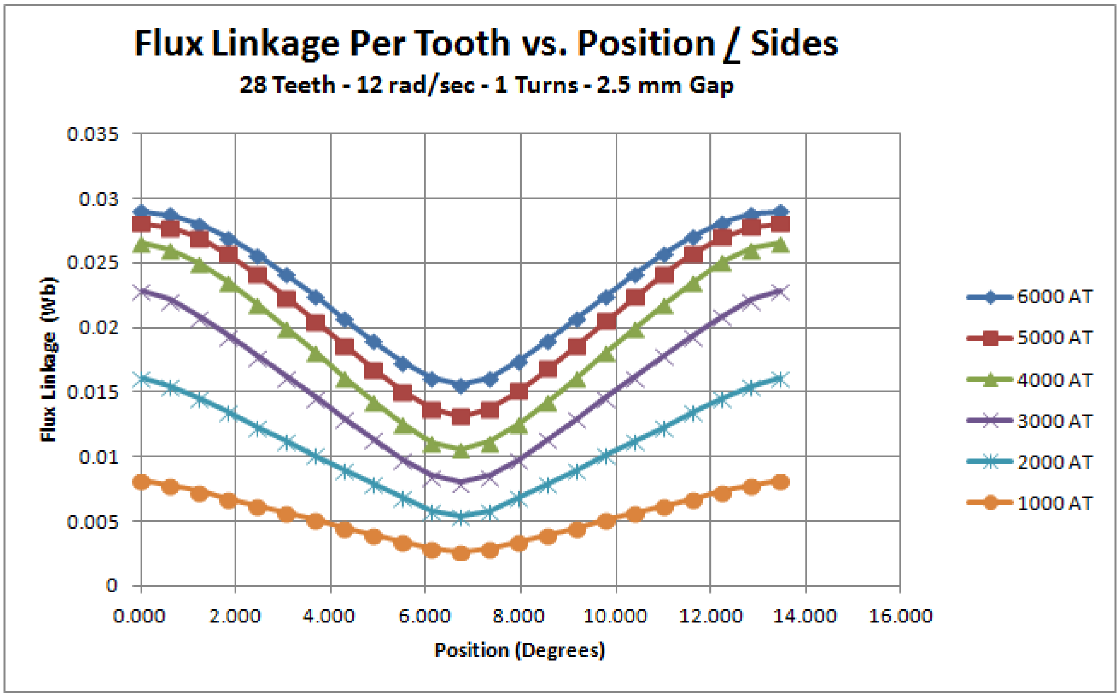

Figure 74 – Multi Coil Axial Gap SRM FEA Result – Flux Linkage versus Position

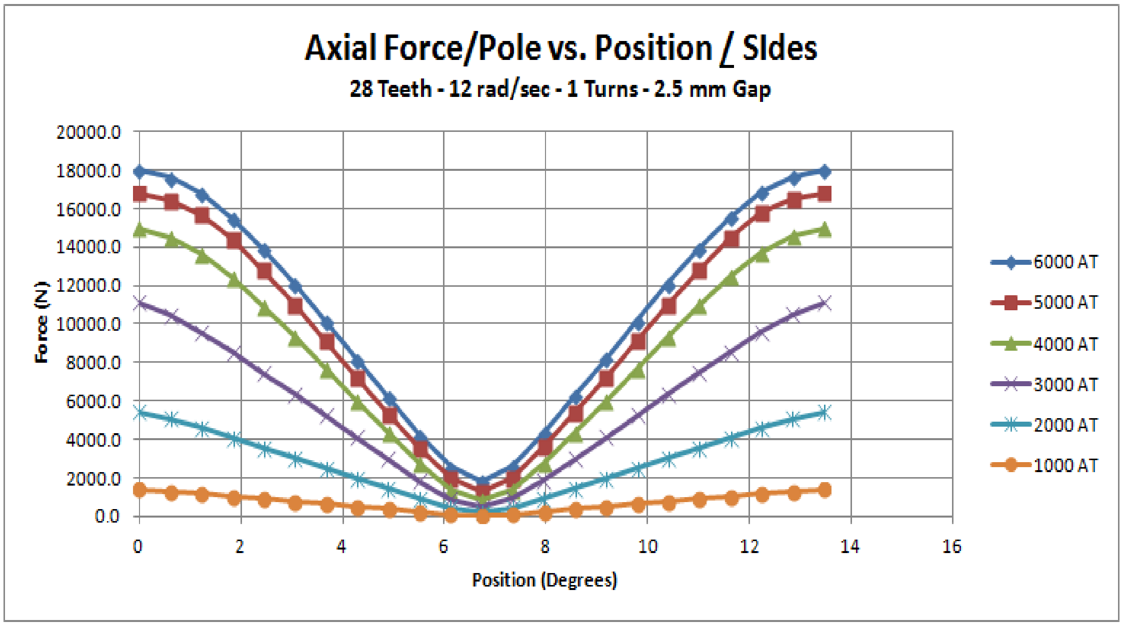

Figure 75 – Multi Coil Axial Gap SRM FEA Result – Half Tooth Axial Force versus Position

Radial Gap SRM (Cylindrical) Configuration

Figure 76 illustrates the radial gap SRM geometry for comparison to the axial gap SRM. The cylindrical gap SRM structure has three separate phases, rotationally aligned to be phase shifted 120 electrical degrees apart. Each phase has 28 poles; only one pole of a phase need be analyzed to predict the machine performance. Using 2D FEA a model was set up that bisects the teeth; boundary conditions applied to the bisecting surfaces is adequate to replicate the magnetic field distribution in the SRM.

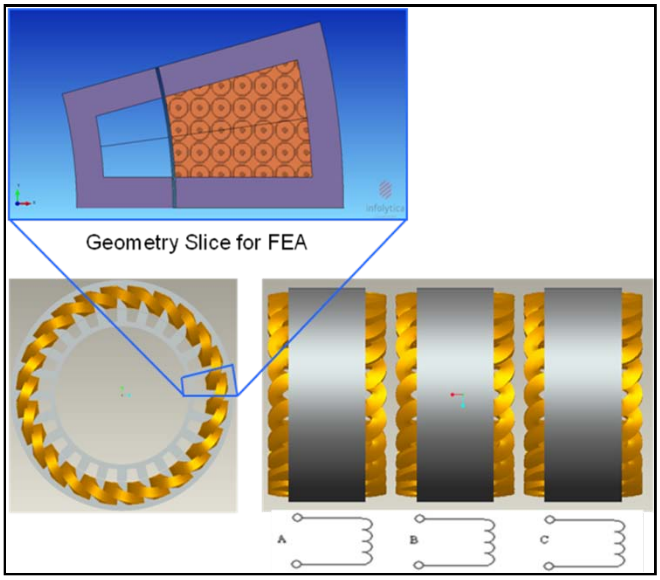

Figure 76 – Radial Gap SRM Geometry and FEA Model

Figure 77 shows magnetic flux field lines and flux densities (B) in the rotor, stator and gap for the aligned (left) and unaligned (right) positions. The colors show a variation in flux density at the two positions with gap field strengths of over 1.7 Tesla (T) aligned and below 1 T unaligned.

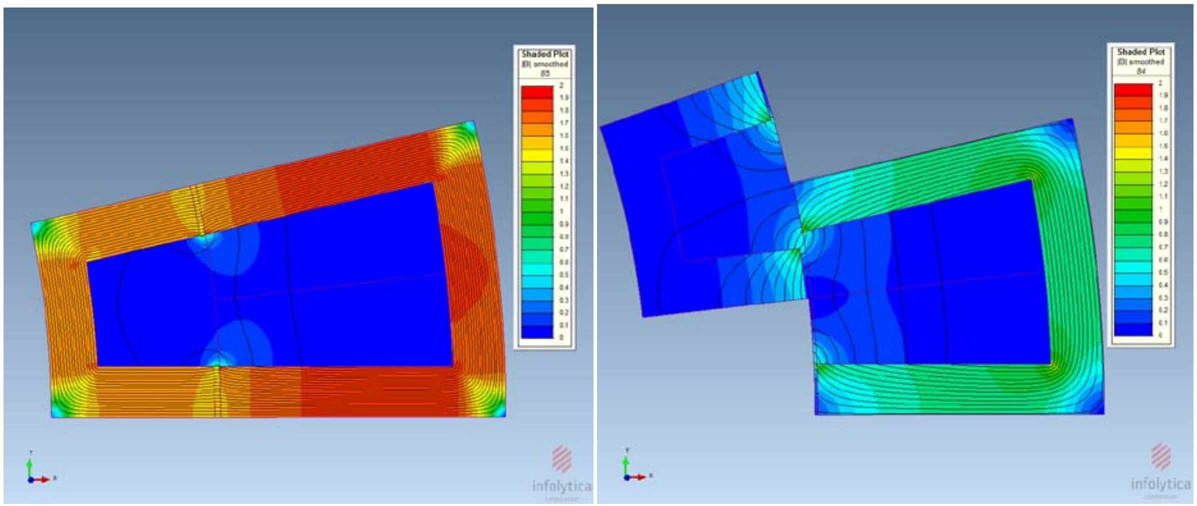

Figure 77 – Flux Plots in the Aligned and Unaligned Position – 2.5 mm gap 8000 NI

The change in the magnetic field in the gap is paramount for machine performance. The FEA uses the change in energy to calculate torques at different positions and currents (Figure 78). Inductance variations are also calculated (Figure 79) for use in power electronic simulations.

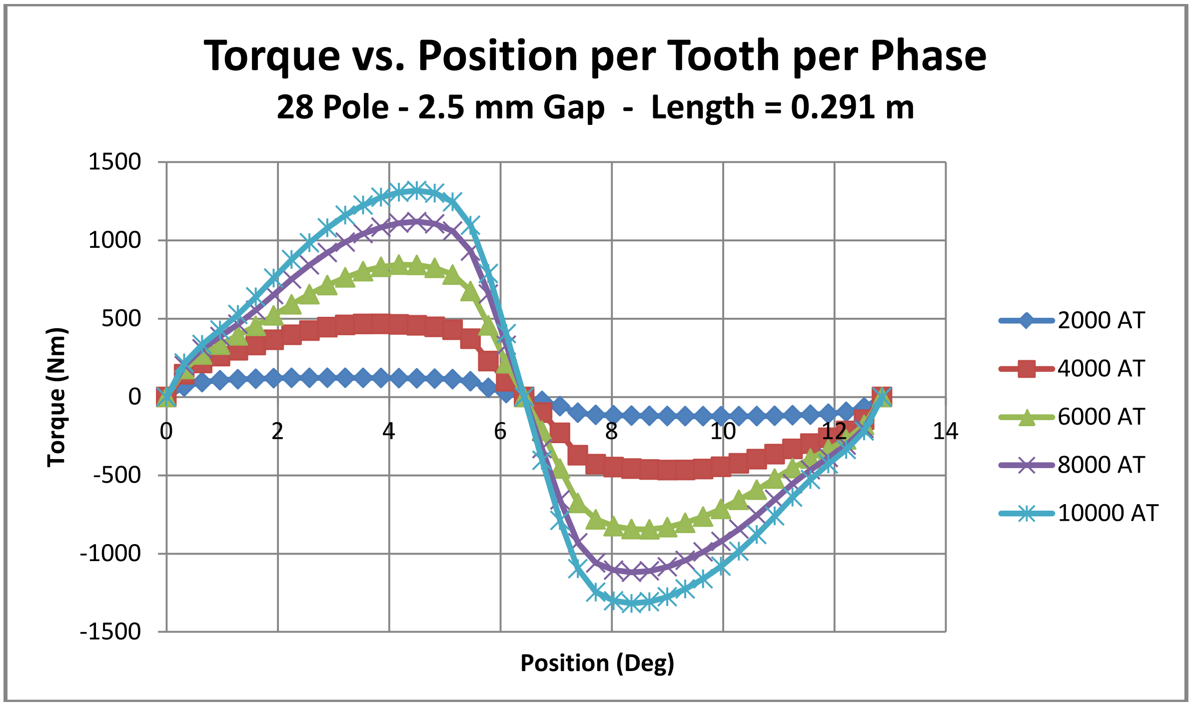

Figure 78 – Radial gap Machine, Torque per Tooth vs. Position

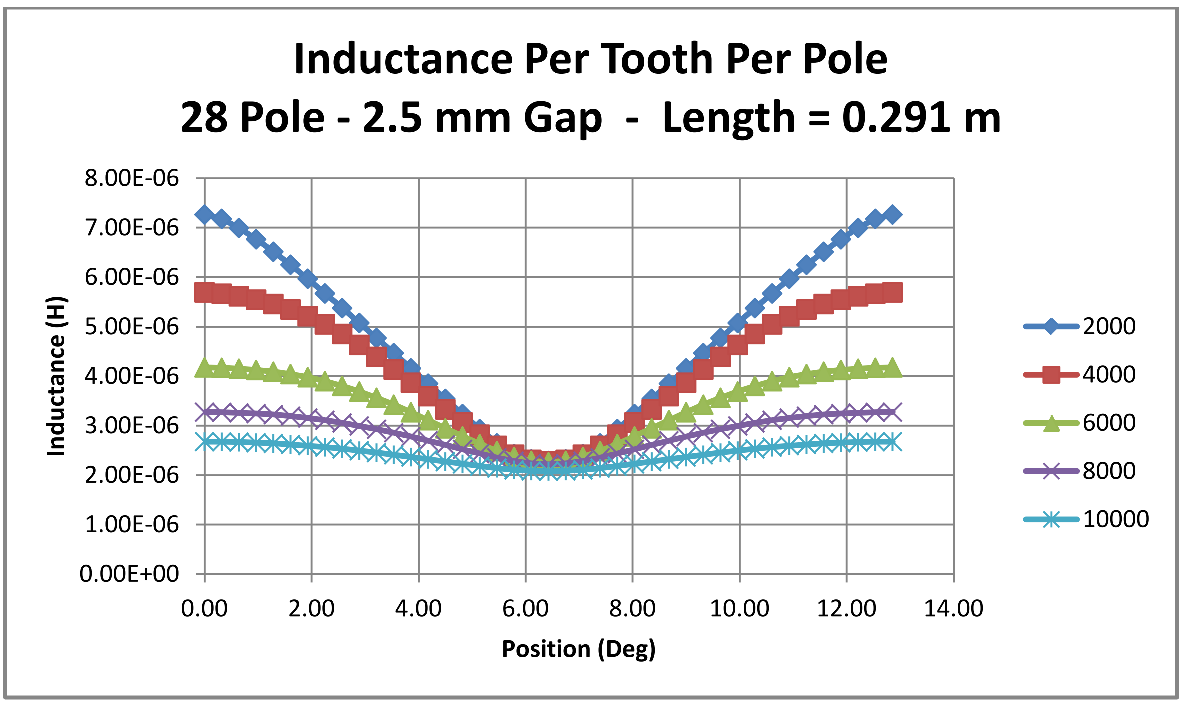

Figure 79 – Radial gap Machine, Inductance per Tooth vs. Position

Radial and Axial Gap SRM Comparison

Table 8 summarizes key parameters of the two cases used for radial and axial gap SRM comparison.

Table 8 – Radial and Axial SRM Parameter Comparison

Parameter	***RG SRM Model***	***Unit***	***AG SRM Model***	***Unit***
Poles (N)	28		28	
Pole Span	12.857	deg	12.857	deg
ID	0.77815	m	0.637	m
OD	1.8815	m	1.219	m
Axial Direction Stack Length (1 phase length)	0.291	m	0.14	m
Radial Gap & Mean Pole Dia.	0.928	m	0.928	m
Air Gap	0.0025	m	0.0025	m
Tooth Width	5.557	deg	5.784	deg
Valley/(Tooth + Valley)	0.5687	m	0.55	m
Phase Length	0.29	m	0.14	m
Thickness stator back iron	0.0236	m	0.0125	m
Thickness rotor back iron	0.0224	m	NA	m
Depth stator slot	0.105	m	0.025	m
Depth rotor slot	0.053	m	0.025	m

For Table 8 comparison, the multiple coils per phase axial gap SRM configuration is used.

Table 9 – Machine Comparison - Pugh Matrix

			Parameter	*Phase Seperation*	*Machine Density*	*Gap Shear Stress*	*Inductance Variation*	*Average Inductance*	*Negative Stiffness*	*Structural Stiffness*	*Ease of Assembly*	*Ease of Lamination*	*Heat Transfer*	*Winding Simplicity*	*EMF Harmonics*	*Score*
ID			Description \ *Weighting*	*8*	*7*	*5*	*5*	*4*	*3*	*3*	*2*	*2*	*3*	*1*	*1*	*220*
1	a		Cylindrical Gap Multi Pole	5	1	5	5	5	4	4	3	4	5	3	4	177
1	b		Cylindrical Gap - 2 Pole	5	0	4	5	3	3	3	1	4	3	5	4	143
2	a	i	Axial Gap - 2 Pole- Coil In - ∠ Tooth	5	4	3	2	2	1	1	1	2	2	5	3	127
2	a	ii	Axial Gap - 2 Pole- Coil In - // Tooth	5	4	3	3	3	2	1	1	3	2	5	4	142
2	b	i	Axial Gap - 2 Pole - Coil Out - ∠Tooth	5	3	3	2	1	1	2	2	2	3	4	3	123
2	b	ii	Axial Gap - 2 Pole - Coil Out - // Tooth	5	3	3	3	2	2	2	2	3	3	4	4	138
3	a	i	Axial Gap - Multi Pole - ∠ Tooth	5	5	4	5	4	2	3	3	2	4	3	3	179
3	a	ii	Axial Gap - Multi Pole - //Tooth	5	5	4	4	4	3	3	3	2	4	3	4	178
4	a		Multi Phase & Pole - Single Core -Cylindri	0	3	2	5	5	4	4	4	5	4	2	4	136
4	b		Mult Phase & Pole - Single Core - Axial Ga	0	2	2	5	5	3	4	4	4	3	2	4	121

Table 9 compares the various SRM Machine configurations considered in this effort, based on relative scores on a scale of 1 to 5 for each parameter. Each parameter is weighted on a scale of 1 to 8 for the DOE wave energy application. The composite score for each machine is achieved by summing the products of each machine's parameter weighting and score. The table shows the axial gap, multi-coil SRM configuration scores highest primarily due to the high machine power density (power per unit weight/volume) characteristic. The multiple coil per pole Axial Gap Switched Reluctance Machine (AGSRM) is the best of the three AGSRM options evaluated largely because the multi pole phase allows for reduced end iron thickness and no iron is required to carry flux between the two stator plates. The AGSRM has a much better packing factor than the RGSRM, largely because the AGSRM eliminates the large unused volume inside the RGSRM rotor. This reduces the size of the machine as well as the cost and weight of the housing.

Significant results (Task 5)

Key outcomes (Task 5)

Based on material volumes for the 28 Pole, axial gap, SRM with coils wound around each tooth, the following cost (Table 10) is estimated for magnetic materials.

Table 10 – Estimated Cost for Magnetic Materials

SRM - Axial Gap Magnetic Materials Cost		
Parameter	Value	Unit
Phases	3	
Teeth	28	
Stator Steel Volume	2808	in3
Rotor Tooth Volume	24.0	in3
Stator Coil Volume	44.45	in3
Lamination Packing Factor	0.95	
Coil Packing Factor	0.7	
Scrap Factor	0.6	
Total Copper Volume	2614	in3
Total Copper Mass	846.826	Lb
Total Steel Volume	29856.6	in3
Total Steel Weight	8240.42	Lb
Magnet Wire Cost	$9,493	
Steel Cost	$9,888	
Total Cost	$19,381	

Table 11 provides the following wire costs based on COTS materials prices from websites and the lamination price from a verbal quote from a vendor (Polaris Laminations).

Table 11 – Estimated COTS Magnetic Materials

Magnet Wire Cost per Pound	11.21	$/Lb
Lamination Cost per Pound	1.20	$/Lb

Task 6.0: Project Management and Reporting

Specific objectives (Task 6)

Reports and other deliverables have been provided in accordance with the Federal Assistance Reporting Checklist following the instructions included therein. Additionally regular conference calls between team members have been conducted.

Major activities (Task 6)

This task has involved the coordination of project activities, including DOE kick-off meeting, assigning project tasks, maintaining the project schedule, holding regular internal program progress reviews, and creating reports.

Significant results (Task 6)

Participated in the DOE kickoff meeting on February 18, 2014.
Participated in the DOE Wind and Water Power Technologies Office Peer Review, on February 25, 2014.
Participated in an interim review presentation to the DOE sponsor on May 20, 2014.

Key outcomes (Task 6)

This final report is the principle output of this task.

Accomplishments

This project has enabled a point design comparison of a radial flux based SRM design with an axial flux variant both using the stacked single phase approach to a three phase machine. The detail to which the design was taken relied on actual detail design backed up with precise analysis and simulation rather than estimation. The work in this study provides templates and tools for evaluation of machine and drive electronics for switched reluctance machines used as either generators or motors.

Conclusions

The comparison between the original radial flux machine and the new axial flux machine, shown in Figure 80, indicate that for the same torque, the axial flux machine diameter will be 27% greater, but it will be much shorter having 30% of the length, and 76% of the weight. Based on these results, it is concluded that an axial flux reluctance machine presents a viable option for large generators to be used for the capture of wave energy.

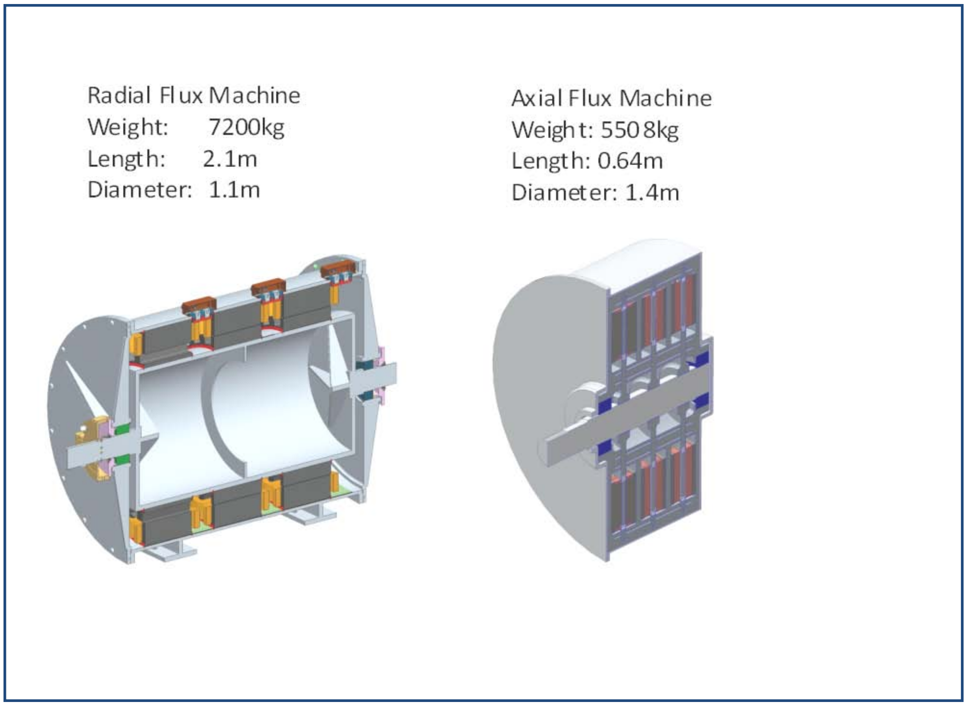

Figure 80 – Radial and Axial Flux Machine Features

Recommendations

In the analysis of Task 4 it is pointed out that our selection of dimensional similarity for the 'apples to apples' comparison did not produce an optimum axial flux machine design. There is torque capability to spare, implying we could reduce the magnetic structure, but the winding area, constrained by the pole separation at the inner pole radius has a higher resistance than desirable, implying we need more room for copper. Our recommendation is to perform an iteration cycle of optimization to balance these better and then proceed to a detailed design phase to produce manufacturing drawings, followed by the construction of a prototype to test the performance of the machine against predicted results.

References

1. K.Watanabe, S.Aida, A.Komatsuzaki, I.Miki: "Driving Force Characteristics of 40kW Switched Reluctance Motor for Electric Vehicle" ICEMS 2007 pp.1894-1898

2. Arihara, H. ; Shibaura Inst. of Technol., Tokyo, Japan ; Akatsu, K., “A Basic Property of Axial Type Switched Reluctance Motor”, (ICEMS), 2010 International Conference on Electrical Machines and Systems;10-13 Oct. 2010, Page(s):1687 – 1690, Print ISBN:978-1-4244-7720-3, INSPEC Accession Number: 11694788

3. Zhan Qionghua, Wang Shuanghong, Ma Zhiyuan, Guo Wei, Qiu Yihui: "Design of a 50kW Switched Reluctance Machine for HEV Propulsion System" Vehicular Technology Conference, 2003. VTC 2003-Fall. 2003 IEEE 58th pp.3207-3211

4. Shuanghong Wang, Qionghua Zhan, Zhiyuan Ma, Libing Zhou: "Implementation of a 50-kW Four-Phase Switched Reluctance Motor Drive System for Hybrid Electric Vehicle" IEEE transaction on Magnetics Volume.41 pp.501-504

5. Z. Wang, Y.Enomoto, M.Ito, R.Masaki, S.Morinaga, H.Itabashi, S.Tanigawa: "Development of an Axial Gap motor with Amorphous Metal Cores" ICEMS 2009 pp1-6

6. Bum-Sik Kim, Won-Hyun Oh, Eun-Chul Shin, Sam-Jun Seo, Sang-Bin Lee, Ji-Yoon Yoo; "Current control method using a double band hysteresis" Industrial Electronics Society, 2004. IECON 2004. 30

7. R.Krishnan: "Switched Reluctance Motor Drives" 2001 by CRC Press LLC pp327

8. Jian Li, Xueguan Song, Yunhyun Cho: "Comparison of 12/8 and 6/4 Switched Reluctance Motor: Noise and Vibration Aspects" IEEE transaction on Magnetics Volume.44 pp.4131-4134

9. Ayumu Nishimiya, Hiroki Goto, Hai-Jiao Guo and Osamu Ichinokura, "A Novel Torque Control for a SR motor EV," Elec. and Comm. Eng. Dept., Tohoku University, Elec. and Inform. Eng. Dept., Tohoku Gakuin University, Proceedings of the2008 International Conference on Electrical Machines, Paper ID 1176, 2008.

10. H. Goto, Y. Suzuki, K. Nakamura, T. Watanabe, H. J. Guo, and O.Ichinokura, "A multipolar SR motor and its application in EV," Journalof Magnetism and Magnetic Materials, Vol.290-291, pp.1338-1342, 2005. (Pubitemid 40370437)

11. R. Madhavan, "A Novel Axial Flux Segmented SRM for Electric Vehicle Application," IEEE XIX International Conferrence on Electrical Machines-ICEM 2010, Rome.

12. Hirom Arihara, Kan Akatsu, "Characteristics of Axial type Switched Reluctance Motor," Energy Conversion Congress and Exposition (ECCE), 2011 IEEE, 3582-3589.

13. Madhavan, R.; Fernandes, B.G. "Comparative analysis of axial flux SRM topologies for electric vehicle application", Power Electronics, Drives and Energy Systems (PEDES), 2012 IEEE International Conference on, On page(s): 1 - 6

14. Madhavan, R.; Fernandes, B.G. "Axial Flux Segmented SRM With a Higher Number of Rotor Segments for Electric Vehicles", *Energy Conversion, IEEE Transactions on,* On page(s): 203 - 213 Volume: 28, Issue: 1, March 2013

15. Eskandari, H.; Mirsalim, M. "An Improved 9/12 Two-Phase E-Core Switched Reluctance Machine", *Energy Conversion, IEEE Transactions on,* On page(s): 951 - 958 Volume: 28, Issue: 4, Dec. 2013

16. S. Rana and N.C. Kar, "Steady-State Analysis of Self-Excited Synchronous Reluctance Generators," Proc. of the 2008 IEEE Canadian Conference on Electrical and Computer Engineering, Niagara Falls, May.

17. S. Guha and N.C. Kar, "Saturation Modeling and Stability Analysis of Synchronous Reluctance Generator," IEEE Trans. on Energy Conversion, Vol.23, No.3, September, 2008.

18. http://www.dextermag.com/upload/Dexter_Hitachi_Finemet_Materials_hl-fm10-d.pdf

19. http://www.vacuumschmelze.com/en/research-innovation/materials-design/nanocrystalline-soft-magnetic-materials.html

Appendices

Appendix A: SRM One Coil Per Phase Layout Concepts

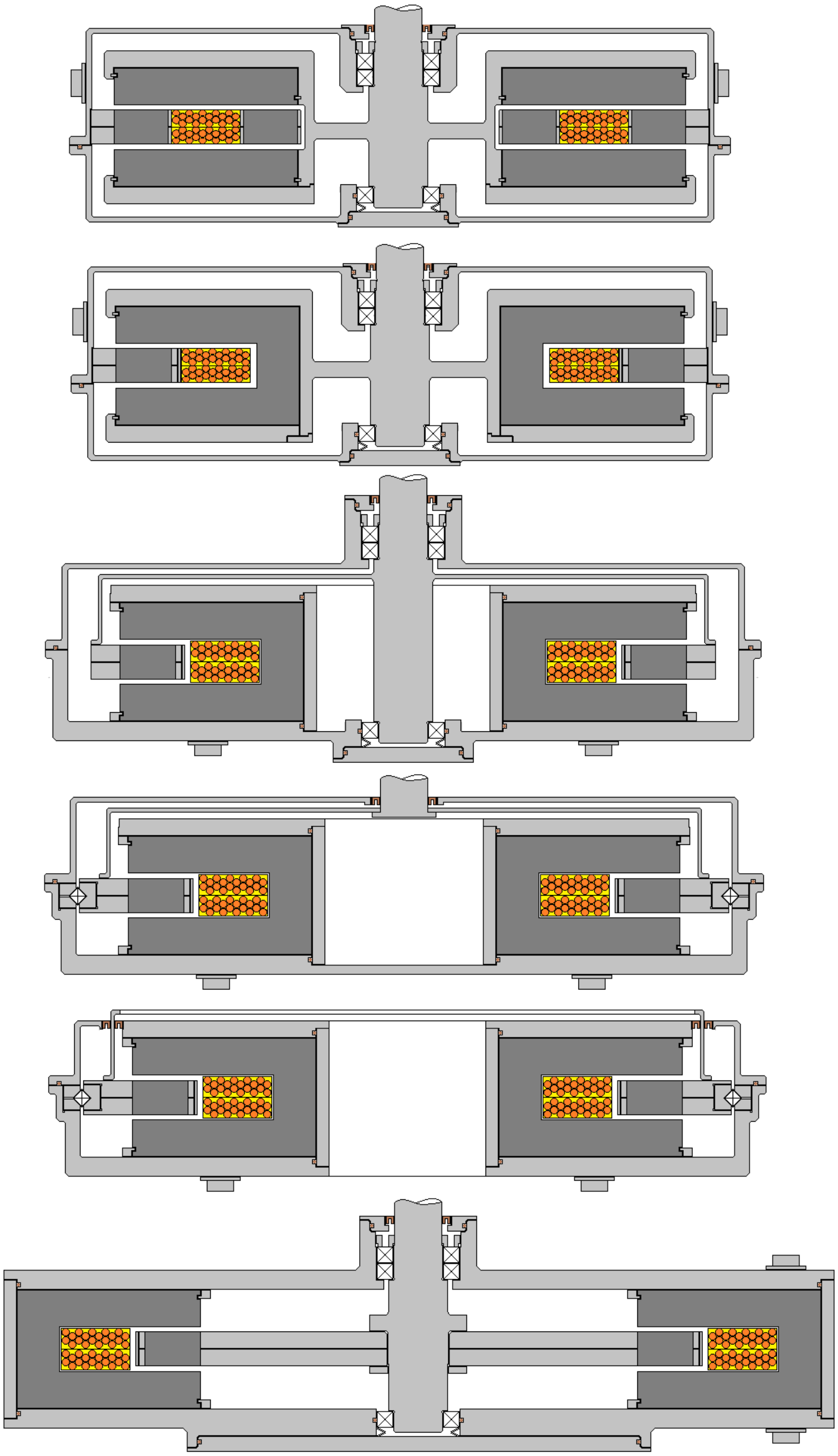

Figure 81. SRM One Coil Per Phase Layout Concepts

One Coil Per Phase – 3 Phase Concept Layout

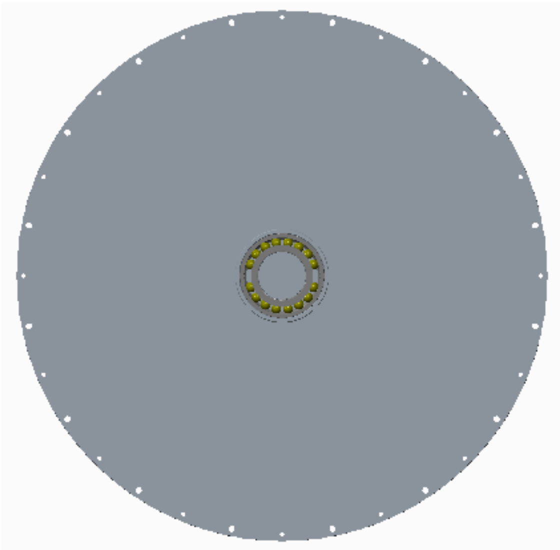

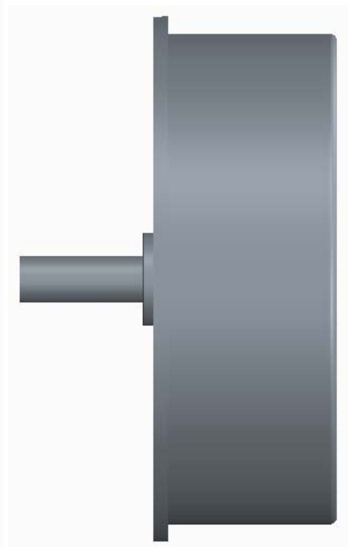

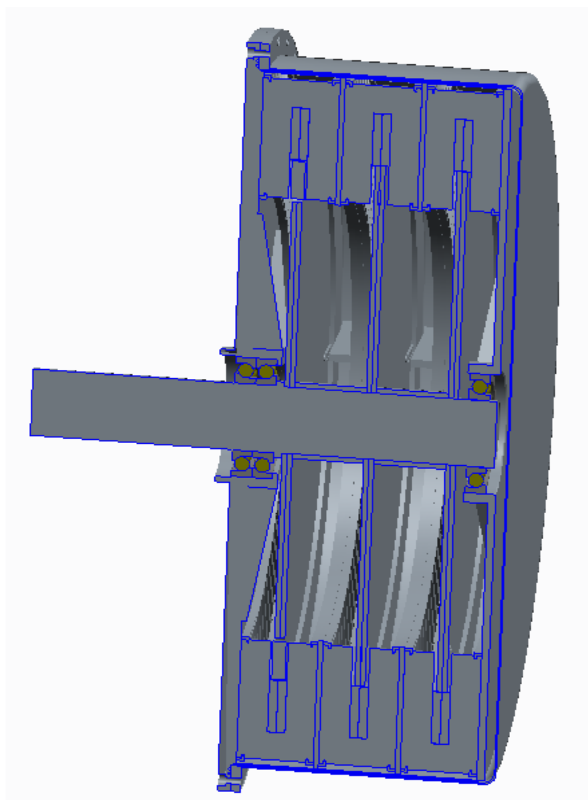

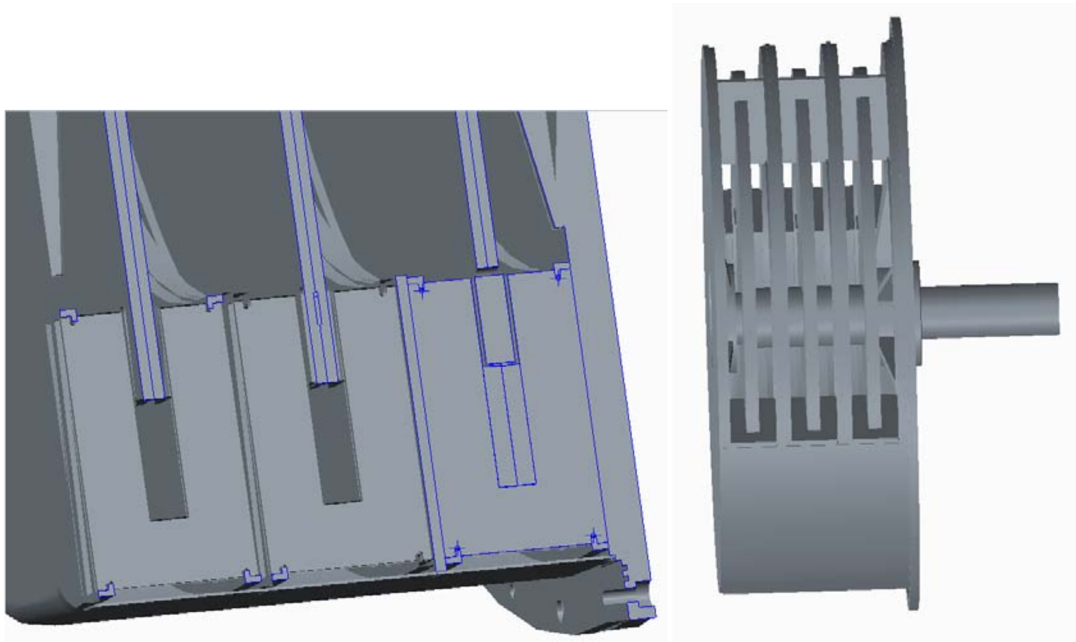

Figure 82. Three Phase Concept Layout

Appendix B: SRM Structural Considerations

Figure 81 shows the force between one side of the rotor and stator tooth. The force varies with rotational position, with the maximum force present when the rotor and stator teeth are aligned.

Typically magnetic design considerations (saturation) dictate material cross section areas that result in low mechanical stress. However, the stiffness of the stator structure is an important design factor and more of a design driver than mechanical stresses. Note that there is an upper limit to the forces because the iron will saturate. It is assumed there is a limit to the current in the machine so the structure is designed to handle the forces at the current limit and not the saturated iron level. A VR machine produces no force with an open or shorted winding, so failure modes are not considered.

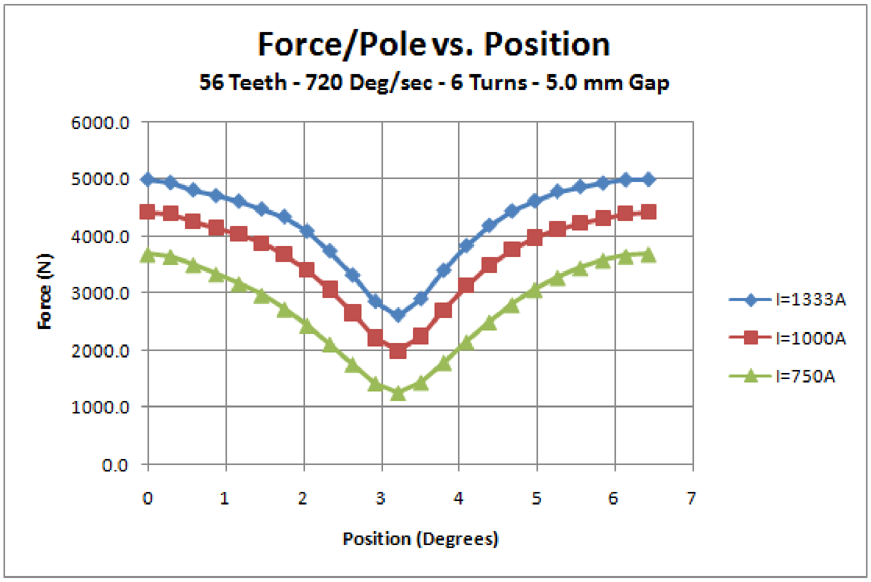

Figure 83 - Typical Stator Attraction Forces

While the rotor has no net axial force when centered, the stator plates are under a mutual attractive force (Figure 82). The stator C shaped structure must react to these magnetically generated axial forces that pull the plates together. The maximum force predicted by the 1 pole FEA model multiplied by the number of teeth times that for the entire disk (Figure 81).

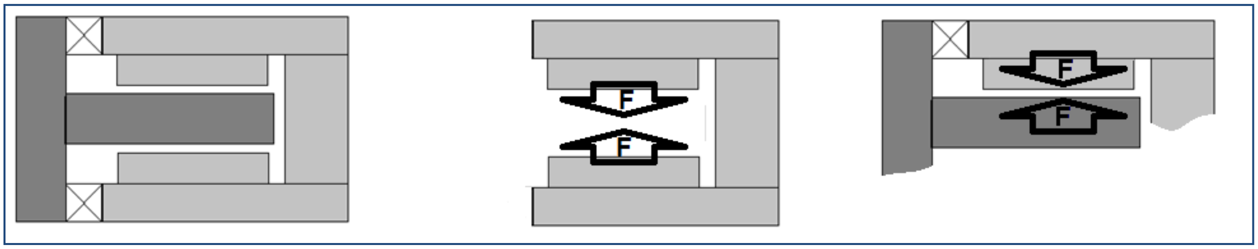

Figure 84 - Rotor & Stator Attraction Force

Stator Design

Two stator stiffness calculations must be evaluated for each of the assembly options. The first stiffness is a series combination of the two stator plate stiffnesses; the second is the series combination a rotor and stator plate stiffness. Equivalent series stiffness (Figure 84) is found with Equation 1:

$$K_{eq} = 1 / [(1/K_1) + (1/K_2)] \qquad \text{(Eq. 1)}$$

Additional structure is present between the plates in the first case and bearings between the stator and rotor in the second case must be considered, but are neglected in this preliminary sizing.

Roark's formulas for Stress & Strain are again used to evaluate the preliminary stator mechanical design. Figure 83 defines the geometry used for the stator structural analyses. By assuming homogenous disks, no strength from the teeth is included in these preliminary analyses. Although the teeth are not continuous circumferentially, they do act as radial stiffening ribs. Future structural FEA will verify closed form, structural estimates.

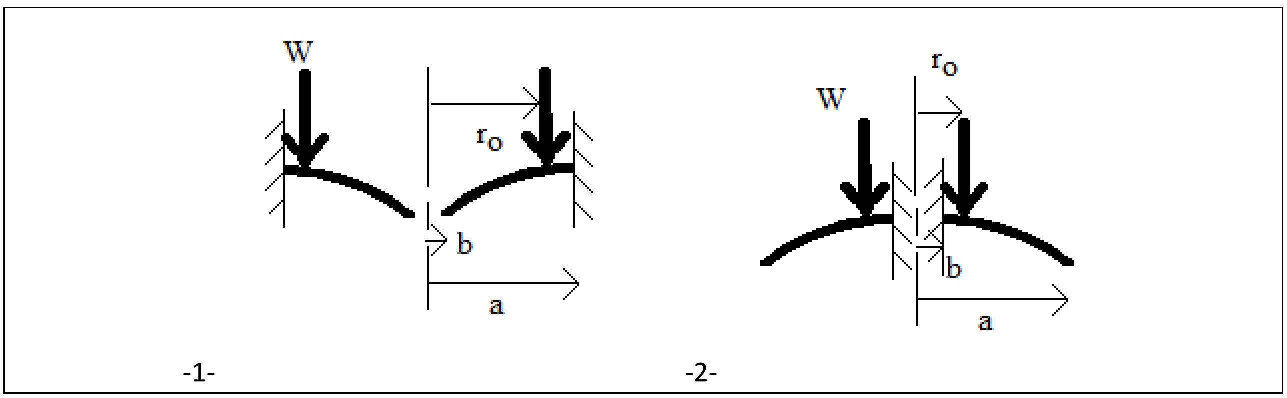

Figure 85 - Stator Plate Geometry and Load Definition

(Inside Rotor Left – Outside Rotor Right)

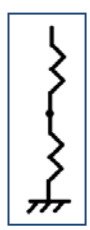

Figure 86 - Series Spring Combination

Table 12 - Stator Plate Axial Stiffness – Rotor Inside Case (Figure 3-1)

Parameter	Symbol	Value	Unit	Value	Unit	Comment
Load	W	1124	Lb	5000	N	
Unit Line Load	w	6.7	Lb/in	1178.9	N/m	
Outer Radius	a	33.268	in	0.845	m	
Inner Radius	b	19.685	in	0.5	m	
Load Radius	ro	26.575	in	0.675	m	
Thickness	t	1.342	in	0.03408067	m	
Young's Modulus	E	2.90E+07	psi	2.00E+11	N/m2	
Poisson's Ration	ν	0.3		0.3		
Plate Constant	D	6415028.6	in Lb	724764.8	Nm	$D=Et^3/12(1-\nu^2)$
Plate Function C1	C1	0.3940		0.3940		
Plate Function C4	C4	0.5917		0.5917		
Plate Function L3	L3	0.0012		0.0012		
Plate Function L6	L6	0.0174		0.0174		
Axial Stiffness 1k./w	Kb	16745	Lb/in2	115444927	N/m2	115444927
Axial Deflection 1k.	yb	0.000402	in	0.000010	m	0.0000102
Axial Stiffness 1k./W	Kb'	2.80E+06	Lb/in	4.90E+08	N/m	4.90E+08
Angular Deflect 1k.	θb	1.96E-03	deg	1.96E-03	radians	0.00003
Angular Deflect 1k.	θa	0.00000	deg	0.00000	radians	0.00000

Table 13 - Stator Plate Axial Stiffness – Rotor Outside Case (Figure 3-2)

Parameter	Symbol	Value	Unit	Value	Unit	Comment
Load	W	1124	Lb	5000	N	
Unit Line Load	w	6.7	Lb/in	1178.9	N/m	
Outer Radius	a	33.464567	in	0.85	m	
Inner Radius	b	13.188976	in	0.335	m	
Load Radius	ro	26.574803	in	0.675	m	
Thickness	t	1.3417587	in	0.034081	m	
Young's Modulus	E	2.90E+07	psi	2.00E+11	N/m2	
Poisson's Ration	ν	0.3		0.3		
Plate Constant	D	6415028.6	in Lb	724764.8	Nm	$D=Et^3/12(1-\nu^2)$
Plate Function C1	C1	0.6136		0.6136		
Plate Function C2	C2	0.6044		0.6044		
Plate Function C3	C3	0.0228		0.0228		
Plate Function C7	C7	0.975		0.975		
Plate Function C8	C8	0.750		0.750		
Plate Function C9	C9	0.297		0.297		
Plate Function L3	L3	0.0013		0.0013		
Plate Function L9	L9	0.1703		0.1703		
Axial Stiffness 1a./w	Ka	648	Lb/in2	4.46E+06	N/m2	4.46E+06
Axial Deflection 1a.	ya	0.0104	in	0.00026	m	0.00026
Axial Stiffness 1a./W	Ka'	1.08E+05	Lb/in	1.89E+07	N/m	1.89E+07
Angular Deflect 1a.	θa	-0.01176	deg	-0.00021	radians	-0.00021
Angular Deflect 1a.	θb	0.00000	deg	0.00000	radians	0.00000

Stator stiffness analyses shows the rotor inside case is a stiffer configuration that rotor outside case (Table 12 & Table 13).

Based on Table 12, the series equivalent stiffness for two identical stator plates is half of one stator plate or 2.45E8 N/m with a back iron thickness of 1 tooth height for the rotor inside configuration. This is adequate given the added stiffness from the rib like teeth.

Likewise, for the rotor outside configuration the effective stator thickness is 0.8E7 N/m. The thickness should be 2.36X one tooth height for this case.

Using the values from Table 4 and Table 6 yield an equivalent stiffness for a rotor & stator combination is tabulated as follows:

- Rotor inside equivalent series stiffness: 1.1 E8 N/m
- Rotor outside equivalent stiffness: 1.4E8 N/m

In conclusion the series rotor and stator plate stiffness is the limiting case for the rotor inside configuration and the series stator plate combination is the limiting case for the rotor outside configuration. The bearing stiffness must be included in the evaluation next.

Appendix C: Negative Stiffness

A very simple math model to describe ferromagnetic attraction per Figure 85 is written as follows:

$$F = C\,(I^2/g^2)$$

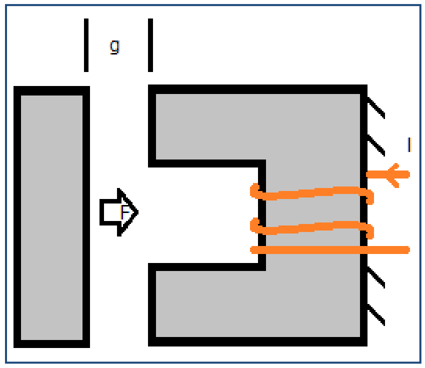

Figure 87 - Attractive Magnet

The force on the armature (Part on Left in Figure 85) is proportional to the square of the current and the inverse of the gap squared.

If the current is held constant and the armature is unrestrained, the armature will accelerate to the right. As it moves, the gap (g) gets smaller (g-Δg) and the force increases because of the inverse relationship $1/(g-\Delta g)^2$ (Figure 86).

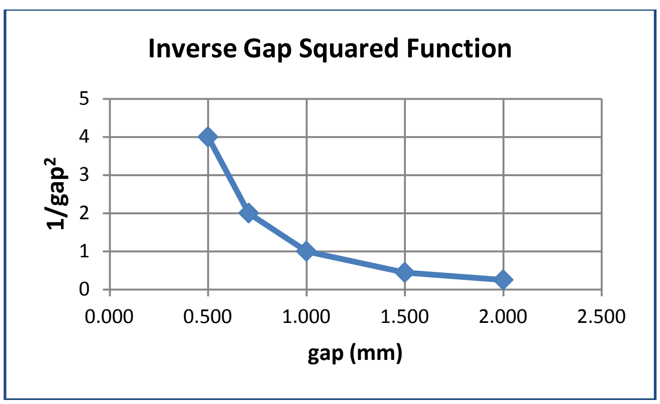

Figure 88 - Inverse Gap Square Function

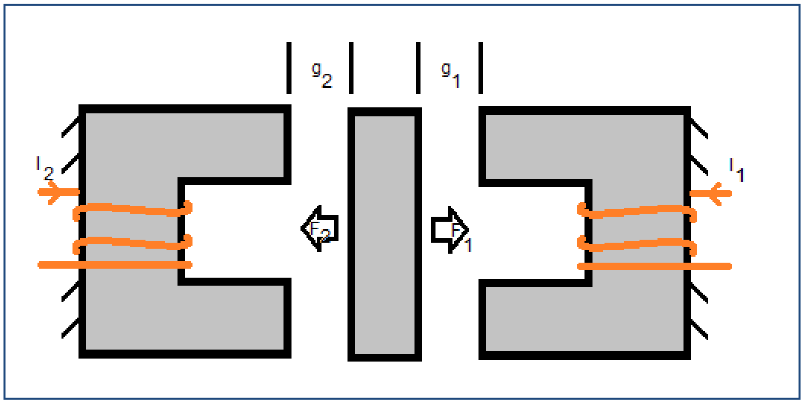

Figure 89 - Attractive Magnet Pair

Now consider the case with two magnets as shown in Figure 87; this structure is analogous to the axial gap SRM. If $I_1 = I_2 = I$ and $g_1 = g_2 = g$, it follows that $|F_1| = |F_2|$; so there is no net force on the armature (i.e., $\Sigma F = F1 + (-F2) = 0$).

However, this force balance is not stable. Similar to a ball on an inverted bowl (Figure 88) the slightest perturbation will cause the armature to move to one side or the other.

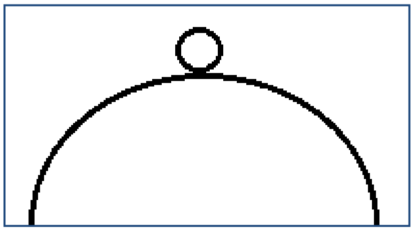

Figure 90 - Instability Analogy

Figure 89 illustrates the case where the gap is disturbed by Δg.

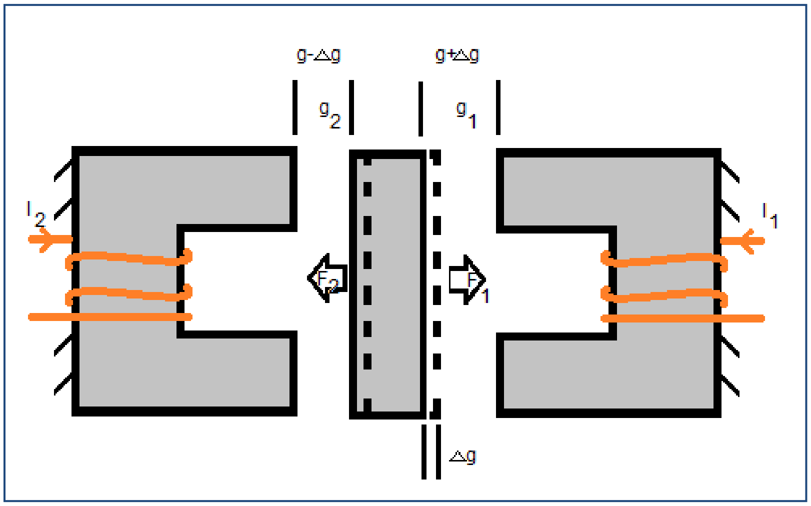

Figure 91 - Displaced Armature Case

Assuming $C_1 = C_2$, keeping $I_1 = I_2$ and doing a bit of algebra, the force acting on the armature is:

$$\Delta F = F_1 + (-F_2)$$

$$= ((C_1\, I_1^2)/(g + \Delta g)^2) - ((C_2\, I_2^2)/(g - \Delta g)^2) \quad ;\ \textit{Substitute for } F_1\ \&\ F_2$$

$$= (C\, I^2)[(1/(g + \Delta g)^2) - (1/(g - \Delta g)^2)] \quad ;\ \textit{Factor out C \& } I^2$$

$$= (C\, I^2)[((g - \Delta g)^2/(g + \Delta g)^2(g - \Delta g)^2) - ((g + \Delta g)^2/(g + \Delta g)^2(g - \Delta g)^2)] \ ;\ \textit{Cross Multiply Denominators}$$

$$= (C\, I^2)\ [\{((g - \Delta g)^2) - ((g + \Delta g)^2)\}/(g + \Delta g)^2(g - \Delta g)^2)] \quad ;\ \textit{Rearranging}$$

$$= (C\, I^2)\ [\{(g^2 - 2g\Delta g + \Delta g^2) - (g^2 + 2g\Delta g + \Delta g^2)\}/(g^4 - 2g^2\Delta g^2 + \Delta g^4)] \quad ;\ \textit{Binomial Expansion \& Canceling Terms}$$

$$= (C\, I^2)\ [(-4g\Delta g)/(g^4 - 2g^2\Delta g^2 + \Delta g^4)] \quad ;\ \textit{Canceling Numerator Terms}$$

$$\approx (C\, I^2)\ [(-4\Delta g)/g^3] \quad ;\ \textit{Approximate by Assuming } \Delta g^2\ \&\ \Delta g^4 \approx 0 \textit{ in Denominator and Canceling}$$

The first order expression for stiffness is found from:

$$K = \Delta F/\Delta g$$

$$K \approx (C\, I^2)\ [\{(-4\Delta g\}/g^3]\ /\Delta g$$

$$K \approx (C\, I^2)\ (-4/g^3)$$

So in the limit, as Δg goes to zero (i.e., the derivative), the stiffness is still finite. Note that it varies as the inverse cube of the nominal gap.

The axial force is large in the axial gap SRM design due to the small gap needed to obtain the necessary electrical behavior. As mentioned previously the forces cancel on the armature when the gaps are equal. However, the stator ends must react to the forces and the structural stiffness must be high to maintain the small gaps.

Figure 90 shows how the simple model discussed above must be adapted for the individual teeth in the SRM configurations. The teeth are mechanically linked but magnetically isolated in the armature. Figure 91 shows how a multi pole version is modeled by the FEA using a portion (blue box) of the multi-pole machine and appropriate boundary conditions. Using the FEA results for two different gaps, stiffness can be found from the change in force divided by the associated change in gap. Since the stiffness are in parallel (Figure 92), their individual stiffness must be added to obtain a full phase value.

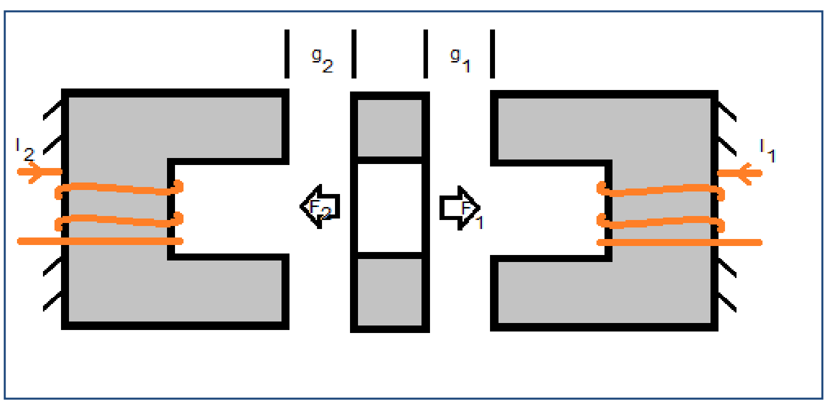

Figure 92 - Modified Armature Case – Magnetically Isolated & Mechanically Linked

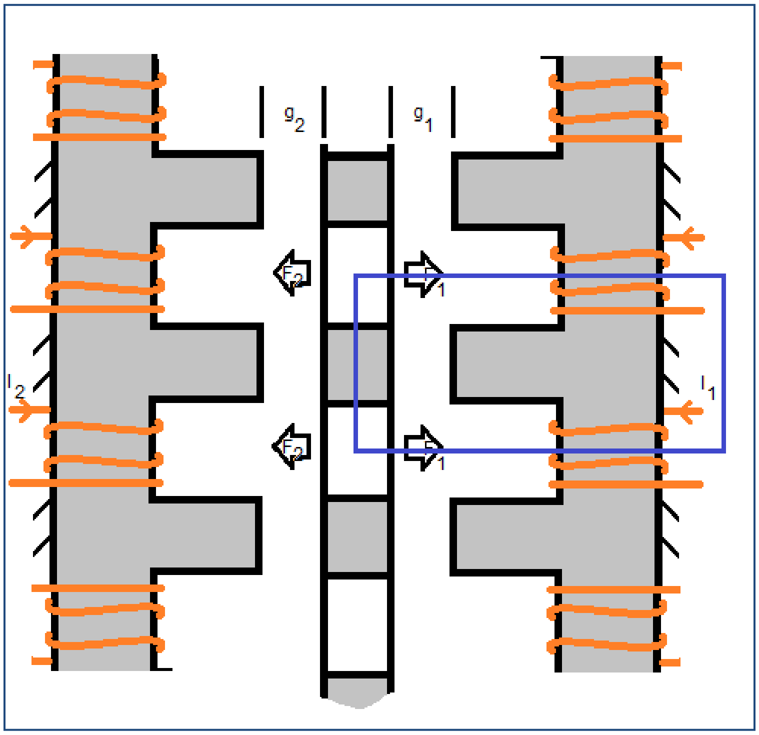

Figure 93 - Multi Tooth Structure

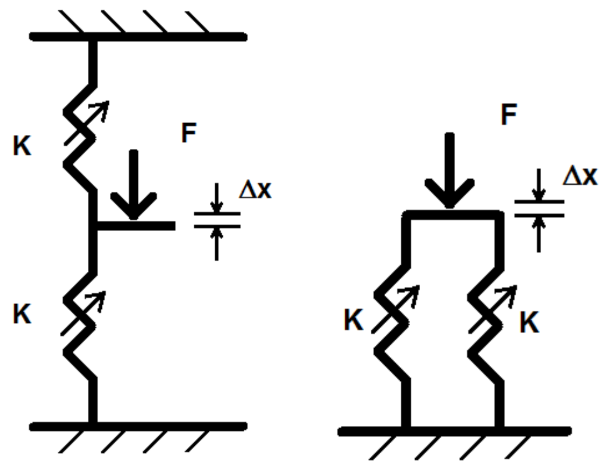

Figure 94 - Springs in Parallel